030601-3-T

Radiation and scattering from printed antennas on cylindrically conformal platforms

Leo C. Kempel, John L. Volakis
and Sunil Bindiganavale

National Aeronautics and
Space Administration
Langley Research Center
Hampton VA 23681-0001

January 1994

THE UNIVERSITY OF MICHIGAN
Radiation Laboratory
Department of Electrical Engineering
and Computer Science
Ann Arbor, Michigan 48109-2122
USA

FINAL REPORT

for NASA Grant NAG-1-1478

NASA Technical Monitor: Fred Beck
GCD, Mail Stop 490
NASA Langley Research Center
Hampton, VA 23681-0001
Telephone: (804) 864-1829

Grant Title: Analysis of Conformal Antennas in Composite Surfaces

Report Title: Radiation and Scattering from Printed Antennas on Cylindrically Conformal Platforms

Institution: Radiation Laboratory
Department of Electrical Engineering
and Computer Science
The University of Michigan
Ann Arbor MI 48109-2122

Date: January 1994

Report Authors: L. C. Kempel, J. L. Volakis and S. Bindiganavale

Principal Investigator: John L. Volakis
Telephone: (313) 764-0500
Volakis@um.cc.umich.edu

Table of Contents

PRIMARY -

Radiation and Scattering from Printed Antennas on Cylindrically Conformal Platforms

PROJECT SUMMARY

The goal of this project is to develop suitable methods and software for the analysis of antennas on cylindrical coated and uncoated platforms. Specifically, the finite element-boundary integral and finite element-ABC methods were employed very successfully for this purpose and associated software were developed for the analysis and design of wraparound and discrete cavity-backed arrays situated on cylindrical platforms. This is the first work which led to the successful implementation of analysis software for such antennas, and several significant developments played a major role in this respect. Among them, are the efficient implementation of the 3D Green's function for a metallic cylinder, the incorporation of the fast Fourier transform in computing the matrix-vector products executed in the solver of the finite element-boundary integral system and the development of a new absorbing boundary condition for terminating the finite element mesh on cylindrical surfaces. Of importance to this project was also the antenna measured data provided to us by Mr. Randy Sliva at the Naval Air Warfare Center, China Lake, CA. Since there is a dearth of reference data in the literature, the patterns provided by Mr. Sliva were essential in validating (to the extent possible) the antenna analysis part of the new formulation and associated software.

As can be realized, the emphasis of our work has so far been on the analysis of uncoated cylindrical platforms. Although of interest to this project was also the simulation of coated platforms, it was necessary to first complete the analysis of antenna on metallic platforms before proceeding with the characterization of patch antennas on the more complex coated configurations. Also, it was necessary to generate reference data for such configurations. Toward this purpose, a new finite element-boundary integral code is near completion for the analysis of flat patches on coated platforms. In this implementation, much effort was devoted to developing an efficient algorithm to evaluate the coated platform Green's function. The already completed and more versatile finite element-ABC code for cylindrically conformal platforms is already capable of simulating patch antennas on coated platforms. However, its validation will not be completed until the results of this code (and associated formulation) are compared with data based on the reference code and possibly measured data to be collected in the coming months. It should be mentioned that the implementation of the reference was delayed because of two dimensional reference code was first developed as described in the University of Michigan Radiation Laboratory report 030601-2-T.

This report contains three main section and two appendices

MAIN SECTIONS:

1. Scattering by Cavity-Backed Antennas on a Circular Cylinder

This section describes the finite element-boundary integral method and its implementation for antennas on cylindrical platforms. The Green's function expressions for large and small radii of curvature are also presented in this section. However, the specific details of the resulting system solution in conjunction with the FFT are given in the U-M Radiation Laboratory report 030601-1-T. Of most importance in this section is the presentation of scattering patterns for several patch antenna configurations illustrating the curvature effects. From these results we conclude that patch arrays on wraparound

substrates exhibit much higher RCS when compared to the same array of patches configured in individual cavities. Also, curves patches are typically of lower Q than flat patches of the same size.

2. Radiation by Cylindrical Conformal Antennas

This section addresses the performance of patch radiators on curved platforms. It includes comparisons of measured and calculated antenna patterns for patch arrays. These results demonstrate the effectiveness of the first ever robust formulation for the analysis of non-planar conformal patch antennas. From the results, it is shown that careful placement of the radiator patches is required to suppress back lobes in the radiation pattern. An important future task is, of course, the characterization of different antenna configurations. We can now begin to consider coupling issues and the effect of treatment and curvature on the input impedance and antenna RCS. We intend to submit an more detailed report on this subject in the very near future.

3. Finite Element-Boundary Integral Code Manual

This section serves as a users manual for the subject code. Also a short description of the code's operation is included. The effective use of this code should provide the user with a good tool for the analysis and design of patch antennas on cylindrical platforms.

APPENDICES

Appendix 1

This appendix gives preliminary results based on the finite element-absorbing boundary condition(FE-ABC) formulation code. This code is more versatile than the finite element-boundary integral code discussed above. It potentially allows the modeling of composite platforms and surface treatments. Also, this formulation, which is based on a new class of conformal ABCs, can be generalized to allow modeling of doubly conformal platforms. Additional validation and development of this code is necessary before it can be transferred to other users.

Appendix 2

This Appendix describes the finite element-boundary integral(FE-BI) formulation for antennas recessed in a coated ground plane. The emphasis on a new efficient evaluation of the Sommerfeld-type Green's function for the coated grounded plane and its incorporation into our existing FE-BI code. The intent is to use this code to generate reference data for validating the more versatile FE-ABC code and associated formulation.

Scattering by Cavity-backed Antennas on a Circular Cylinder

Leo C. Kempel and John L. Volakis
Radiation Laboratory
1301 Beal Ave.
Ann Arbor, MI 48109-2122

November 15, 1993

Abstract

Conformal arrays are popular antennas for aircraft, spacecraft and land vehicle platforms due to their inherent low weight and drag properties. However, to date there has been a dearth of rigorous analytical or numerical solutions to aid the designer. In fact, it has been common practice to use limited measurements and planar approximations in designing such non-planar antennas. In this paper, we extend the finite element-boundary integral method to scattering by cavity-backed structures in an infinite, metallic cylinder. In particular, we discuss the formulation specifics such as weight functions, dyadic Green's function, implementation details and particular difficulties inherent to cylindrical structures. Special care is taken to ensure that the resulting computer program has low memory demand and minimal computational requirements. Scattering results are presented and validated as much as possible.

1 Introduction

Conformal antenna arrays are attractive for aircraft, spacecraft, and land vehicle applications since these antenna systems have low weight, low drag, flexibility, and cost advantages over conventional protruding antennas. The majority of previous studies pertaining to non-planar conformal antennas has been conducted experimentally due to a dearth of rigorous analysis techniques. Traditional rigorous techniques involve an integral equation and are limited in terms of radius of curvature and structural complexity. Some approximate methods have been considered but these are restricted in accuracy and element shape.

Recently, the finite element–boundary integral (FEM-BI) method was successfully employed for the analysis of large cavity-backed planar arrays [1]. The resulting system is sparse due to the local nature of the finite element method, whereas the boundary integral sub-matrix is fully populated. However, by resorting to an iterative solver such as the Biconjugate Gradient (BiCG) method, the boundary integral sub-system may be cast in circulant form allowing use of the Fast Fourier Transform (FFT) in performing the matrix-vector products. This BiCG-FFT solution scheme ensures $\mathcal{O}(N)$ memory demand for the entire FEM-BI system and minimizes the computational requirements.

In this paper, the FEM-BI formulation is extended to scattering by aperture antennas conformal to a cylindrical metallic surface. In contrast to the planar aperture array, the implementation of the cylindrically conformal array requires shell-shaped elements rather than bricks, and the required external Green's function must satisfy the boundary conditions on the surface of the cylinder. In its exact form, this Green's function is an infinite series which imposes unacceptable computational burdens on the method. However, for large radius cylinders, a suitable asymptotic formula is available and herein used for an efficient evaluation of the Green's function. In addition, the resulting BI system is again cast in circulant form to ensure an $\mathcal{O}(N)$ memory demand and to take advantage of the FFT's efficiency when carrying out the matrix-vector product.

A primary difficulty in studying cavity-backed antennas mounted on curved surfaces is the lack of reference data. In this paper, scattering calculations based on the FEM-BI method are compared with data based on different techniques. Although such validation is necessarily limited, it provides con-

fidence in the formulation's accuracy so that this approach may be used in extending the available reference data.

2 FEM-BI for Circular Cylinders

In this section, the FEM-BI formulation is developed for cavities recessed in an infinite metallic cylinder, having walls which coincide with constant ρ-,ϕ- or z-surfaces (see figure 1). As usual, the finite element formulation permits substantial modeling flexibility, including cavity inhomogeneities, lumped loads, super/substrate antenna configurations, or microstrip line and so on.

The FEM-BI approach possesses both low memory and computational demand when implemented with a BiCG-FFT solver. Although the system of equations associated with the FEM formulation is sparse, the boundary integral sub-matrix is fully populated. However, if the aperture mesh is a uniform grid, the BiCG-FFT solver may be employed for that portion of the system thus retaining $\mathcal{O}$(N) memory demand for the entire system. In addition, the solver require low computational demand since both sparse matrix-vector products and discrete convolutions using FFTs require only $\mathcal{O}$(NlogN) operations per iteration.

The FEM-BI formulation begins with the weak form of the vector wave equation followed by specification of appropriate vector shape functions and dyadic Green's function. The resulting FEM-BI equations are then used to solve for the total electric fields within the cavity and on the aperture (see for example Volakis *et al.* [2]). For the specific configuration at hand, the weak form of the wave equation can be written as

$$\int_{V_i} \left\{ \frac{\nabla \times \vec{W}_j(\rho,\phi,z) \cdot \nabla \times \vec{W}_i(\rho,\phi,z)}{\mu_r(\rho,\phi,z)} \right.$$
$$\left. -k_o^2 \epsilon_r(\rho,\phi,z) \vec{W}_j(\rho,\phi,z) \cdot \vec{W}_i(\rho,\phi,z) \right\} \rho \, d\rho \, d\phi \, dz$$
$$+(k_o a)^2 \delta_a(j) \delta_a(i) \int_{S_i} \int_{S_j} \left[\vec{W}_i(a,\phi,z) \cdot \hat{\rho}(a,\phi,z) \times \right.$$
$$\left. \overline{\overline{G}}_2(a,\bar{\phi},\bar{z}) \times \hat{\rho}(a,\phi',z') \cdot \vec{W}_j(a,\phi',z') \right] d\phi' \, dz' d\phi \, dz = f_i^{int} + f_i^{ext} \quad (1)$$

In this, $\vec{W}_i$ are vector basis functions with support over the volume V_i which is

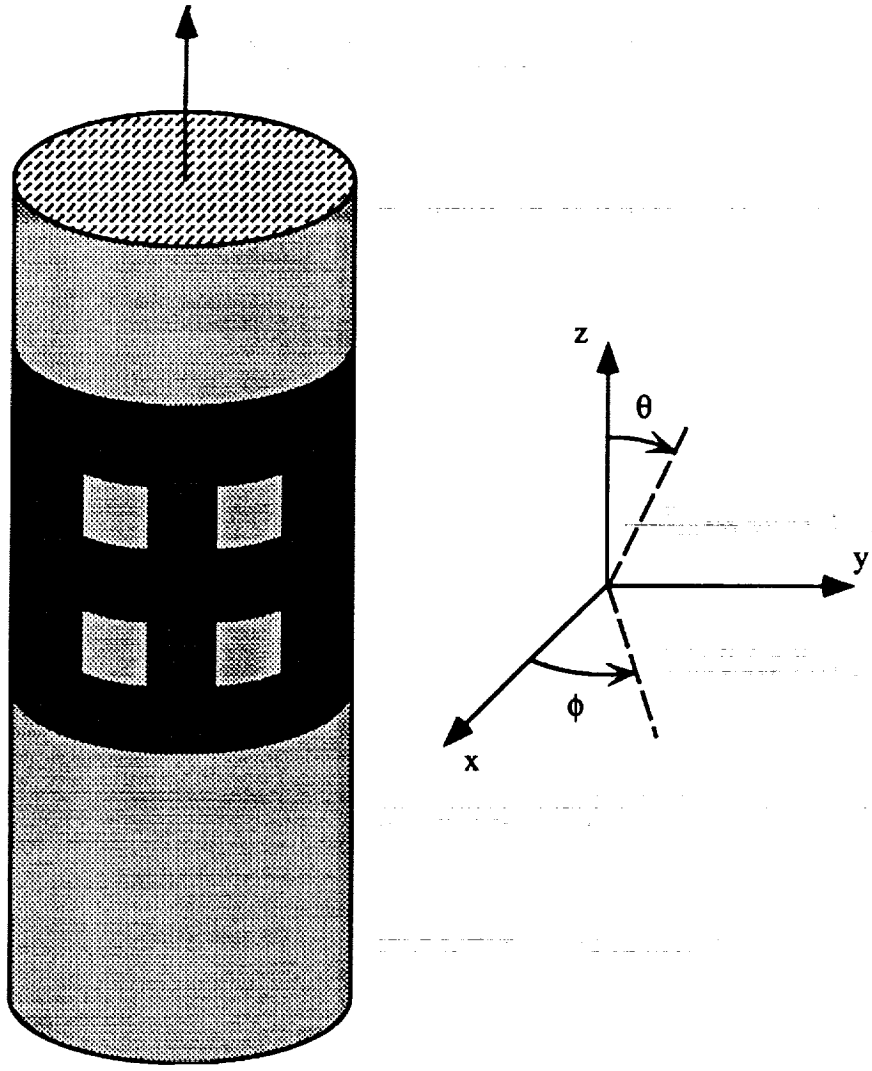

Figure 1: Illustration of a typical cavity-backed antenna situated on a metallic cylinder and the associated coordinate system.

associated with the i^{th} degree of freedom, and in a similar fashion, S_i and S_j represent aperture surfaces associated with the i^{th} and j^{th} degrees of freedom, respectively. The appropriate dyadic Green's function is denoted by $\overline{\overline{G}}_2$ and it has convolutional ($\bar{\phi} = \phi - \phi'$, $\bar{z} = z - z'$) form when evaluated on the surface of the cylinder, $\rho = a$. The unprimed coordinates represent the test point while the primed ones denote the source point. The free-space propagation constant is given by $k_0 = \frac{2\pi}{\lambda_0}$, where λ_0 is the free-space wavelength. The cavity is filled with an inhomogeneous material having relative constitutive properties ϵ_r and μ_r. The function $\delta_a(i)\delta_a(j)$ is the product of two Kronecker delta functions. Hence, it identifies which pairs of unknowns belong to the aperture and accordingly contribute to the boundary integral sub-matrix.

The FEM-BI equation (1) may be rewritten in matrix form as

$$\left[\mathcal{A}\right] \begin{Bmatrix} E_j^{ap} \\ E_j^{int} \end{Bmatrix} + \begin{bmatrix} [\mathcal{G}] & [0] \\ [0] & [0] \end{bmatrix} \begin{Bmatrix} E_j^{ap} \\ E_j^{int} \end{Bmatrix} = \begin{matrix} \{f_i^{ext}\} \\ \{0\} \end{matrix} \tag{2}$$

where the entries of $[\mathcal{A}]$ are due to the FEM portion of the formulation and $[\mathcal{G}]$ is the boundary integral sub-matrix. In (2), E_j^{ap} and E_j^{int} denote degrees of freedom associated with the aperture and interior fields, respectively. In this, f_i^{ext} are functions of the external excitation and will be discussed later in the paper.

An important factor in choosing the finite elements for gridding the cavity is the element's suitability for satisfying the mathematical requirements of the formulation as well as the physical features of the antenna system. Traditional node-based finite elements associate the degrees of freedom with the nodal fields and have proven unsatisfactory for three-dimensional electromagnetics applications since they do not correctly represent the null space of the curl operator and hence spurious modes are generated [3, 4]. In contrast, edge-based elements correctly model the curl operator and therefore the electromagnetic fields. In addition, edge-based elements avoid explicit specification of the fields at corners where edge conditions may require a singularity. Jin and Volakis [6] presented edge-based brick elements which are convenient for rectangular-type structures and cavities. For cavities residing in a circular cylinder, shell elements are the natural choice.

Cylindrical shell elements possess both geometrical fidelity and simplicity for cylindrical-rectangular cavities. Figure 2 illustrates a typical shell element which has eight nodes connected by twelve edges: four edges aligned along

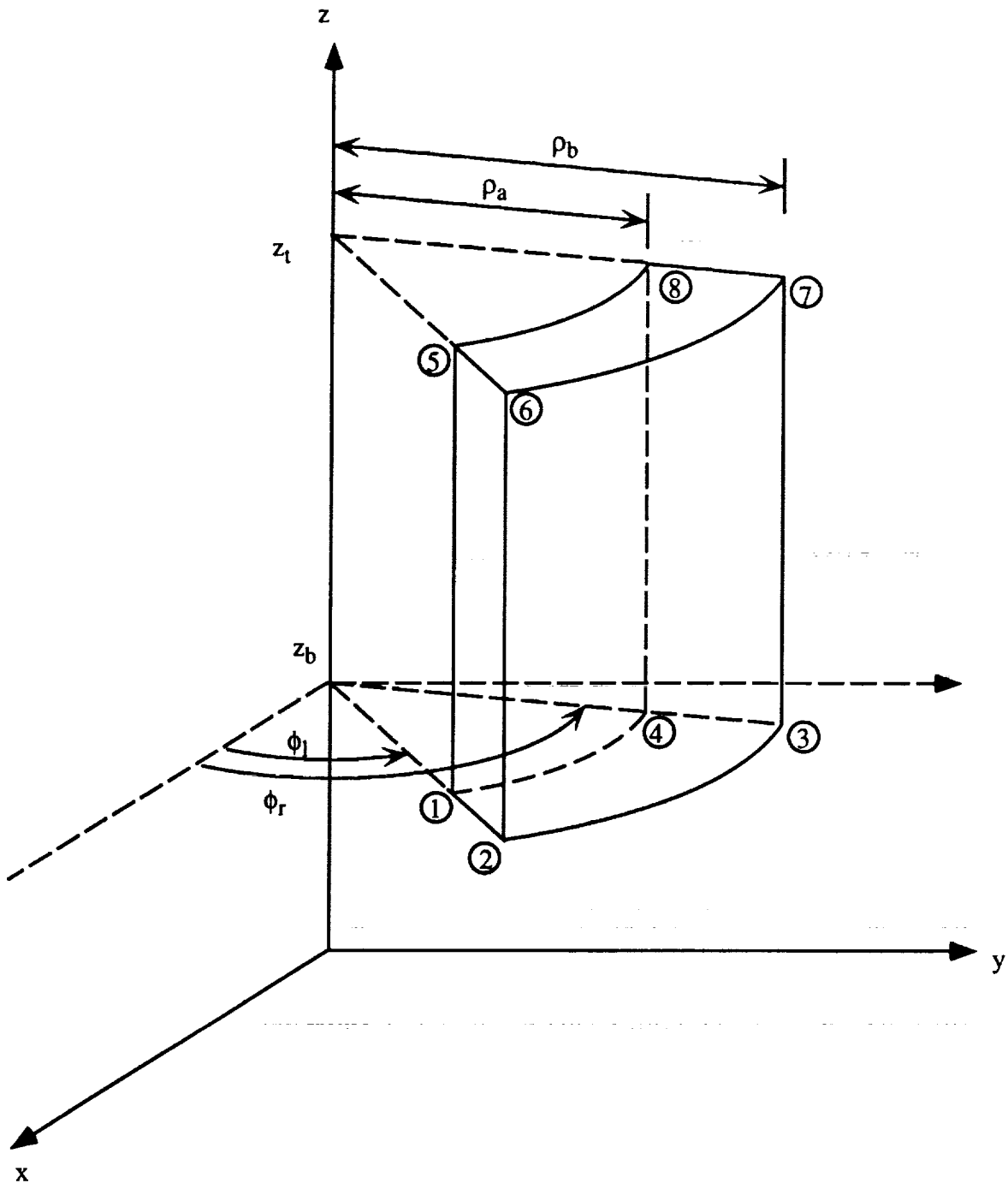

Figure 2: Cylindrical shell element.

each of the three orthogonal directions of the cylindrical coordinate system. Each element is associated with twelve vector shape functions given by

$$\vec{W}_{12}(\rho,\phi,z) = \vec{W}_{\rho}(\rho,\phi,z;\cdot,\phi_r,z_t,+), \quad \vec{W}_{43}(\rho,\phi,z) = \vec{W}_{\rho}(\rho,\phi,z;\cdot,\phi_l,z_t,-)$$
$$\vec{W}_{56}(\rho,\phi,z) = \vec{W}_{\rho}(\rho,\phi,z;\cdot,\phi_r,z_b,-), \quad \vec{W}_{87}(\rho,\phi,z) = \vec{W}_{\rho}(\rho,\phi,z;\cdot,\phi_l,z_b,+)$$

$$\vec{W}_{14}(\rho,\phi,z) = \vec{W}_{\phi}(\rho,\phi,z;\rho_b,\cdot,z_t,+), \quad \vec{W}_{23}(\rho,\phi,z) = \vec{W}_{\phi}(\rho,\phi,z;\rho_a,\cdot,z_t,-)$$
$$\vec{W}_{58}(\rho,\phi,z) = \vec{W}_{\phi}(\rho,\phi,z;\rho_b,\cdot,z_b,-), \quad \vec{W}_{67}(\rho,\phi,z) = \vec{W}_{\phi}(\rho,\phi,z;\rho_a,\cdot,z_b,+)$$

$$\vec{W}_{15}(\rho,\phi,z) = \vec{W}_{z}(\rho,\phi,z;\rho_b,\phi_r,\cdot,+), \quad \vec{W}_{26}(\rho,\phi,z) = \vec{W}_{z}(\rho,\phi,z;\rho_a,\phi_r,\cdot,-)$$
$$\vec{W}_{48}(\rho,\phi,z) = \vec{W}_{z}(\rho,\phi,z;\rho_b,\phi_l,\cdot,-), \quad \vec{W}_{37}(\rho,\phi,z) = \vec{W}_{z}(\rho,\phi,z;\rho_a,\phi_l,\cdot,+) \tag{3}$$

where $\vec{W}_{lk}$ is associated with the edge which is delimited by local nodes (l,k) as shown in figure 2. As seen from (3), three fundamental vector weight functions are required for the complete representation of the shell element. They are

$$\begin{aligned}
\vec{W}_{\rho}(\rho,\phi,z;\tilde{\rho},\tilde{\phi},\tilde{z},\tilde{s}) &= \frac{\tilde{s}\rho_b}{\alpha h}\frac{(\phi-\tilde{\phi})(z-\tilde{z})}{\rho}\hat{\rho} \\
\vec{W}_{\phi}(\rho,\phi,z;\tilde{\rho},\tilde{\phi},\tilde{z},\tilde{s}) &= \frac{\tilde{s}}{th}(\rho-\tilde{\rho})(z-\tilde{z})\hat{\phi} \\
\vec{W}_{z}(\rho,\phi,z;\tilde{\rho},\tilde{\phi},\tilde{z},\tilde{s}) &= \frac{\tilde{s}}{t\alpha}(\rho-\tilde{\rho})(\phi-\tilde{\phi})\hat{z}
\end{aligned} \tag{4}$$

where the element parameters $(\rho_a,\rho_b,\phi_l,\phi_r,z_b,z_t)$ are shown in figure 2, $t = \rho_b - \rho_a$, $\alpha = \phi_r - \phi_l$ and $h = z_t - z_b$. The $\frac{1}{\rho}$-term which appears in the definition of the $\hat{\rho}$-directed weight (4) is essential in satisfying the divergence free requirement, i.e. so that $\nabla\cdot\vec{W}_j = 0$[1]. Note that as the radius of the cylinder becomes large, the curvature of these elements decreases, resulting in weight functions which are functionally similar to the bricks presented

[1] $\vec{W}_j(\rho,\phi,z)$ will only satisfy this requirement within the volume of the element. These weighting functions introduce artificial charges on the faces of the element and are not divergenceless at element interfaces. This is allowable since these elements do not guarantee normal field continuity across the element faces.

by Jin and Volakis [6]. Having specified the vector basis functions, we may proceed to develop the matrix entries for the system (2).

The FEM-BI system is composed of two parts: a sparse FEM matrix and a fully populated BI sub-matrix as shown in (2). The FEM matrix entries are represented by

$$A_{ij} = \frac{1}{\mu_r} I_{st}^{(1)ij} - k_o^2 \epsilon_r I_{st}^{(2)ij} \tag{5}$$

where constant material properties have been assumed within each element. The subscripts (i,j) refer to the row and column of the matrix entry and correspond to the test and source edges, respectively. The auxiliary functions

$$\begin{aligned} I_{st}^{(1)ij} &= \int_{V_i} \nabla \times \vec{W}_s(\rho,\phi,z;\tilde{\rho}_j,\tilde{\phi}_j,\tilde{z}_j,\tilde{s}_j) \cdot \\ &\qquad \nabla \times \vec{W}_t(\rho,\phi,z;\tilde{\rho}_i,\tilde{\phi}_i,\tilde{z}_i,\tilde{s}_i)\rho\, d\rho\, d\phi\, dz \\ I_{st}^{(2)ij} &= \int_{V_i} \vec{W}_s(\rho,\phi,z;\tilde{\rho}_j,\tilde{\phi}_j,\tilde{z}_j,\tilde{s}_j) \cdot \vec{W}_t(\rho,\phi,z;\tilde{\rho}_i,\tilde{\phi}_i,\tilde{z}_i,\tilde{s}_i)\rho\, d\rho\, d\phi\, dz \end{aligned} \tag{6}$$

are identically zero unless both test and source edges share at least one element in common, resulting in a highly sparse system. Physically, such a system is a consequence of the locality property inherent in a partial differential equation formulation. In (6), the direction of the source and test edges are represented by $(s,t) \in \{\rho,\phi,z\}$, respectively. Since the edges of the mesh are aligned along three orthogonal directions, only six combinations of (s,t) are required for $I^{(1)}$ and only three such combinations for $I^{(2)}$ and all of these are evaluated in Appendix A. Since (6) is symmetric with respect to source and test edges, the FEM matrix will also be symmetric.

A lumped impedance post may be included in the formulation by adding a term to (1) and equivalently to (5); surface or sub-surface metallization layers may also be modeled. Radially oriented lumped loads are approximated in the FEM-BI formulation by a filamentary load located at (ϕ_L, z_L) [2]. Such posts have length l, cross-sectional area s and impedance Z_L. The contribution to $[\mathcal{A}]$ is given by

$$A_{ij} = jk_o Z_o \frac{l}{sZ_L} \int_V \frac{\delta(\phi-\phi_L)\delta(z-z_L)}{\rho} W_i(\rho,\phi,z) W_j(\rho,\phi,z) \rho d\rho d\phi dz \tag{7}$$

which may be readily evaluated in closed form. In addition, infinitesimally thin metallization layers may be represented by simply fixing *a priori* the

weight coefficients to zero for weights associated with edges which are tangential to the metal. This is a consequence of using a total electric field formulation. The symmetry and sparsity of the FEM system $[\mathcal{A}]$ is maintained after the addition of these loads while the BI system $[\mathcal{G}]$ remains fully populated and symmetric.

The boundary integral provides an exact boundary condition for mesh closure and its construction relies on a cylindrical dyadic Green's function. The entries of the boundary integral sub-matrix are

$$\begin{aligned} G_{ij} &= (k_o a)^2 \int_{S_i} \int_{S_j} W_t(a,\phi,z;\tilde{\rho}_i,\tilde{\phi}_i,\tilde{z}_i,\tilde{s}_i) \cdot \\ &\quad \left[\hat{\rho}(a,\phi,z) \times \overline{\overline{G}}_2(a,\bar{\phi},\bar{z}) \times \hat{\rho}(a,\phi',z')\right] \\ &\quad \cdot W_s(a,\phi',z';\tilde{\rho}_j,\tilde{\phi}_j,\tilde{z}_j,\tilde{s}_j) d\phi'\, dz' d\phi\, dz \end{aligned} \tag{8}$$

where the weight functions are given by (4) and evaluated at the surface $\rho = a$. In (8), the dyadic Green's function ($\overline{\overline{G}}_2$) satisfies both the radiation condition and the Neumann boundary condition at $\rho = a$. This dyadic Green's function may be expressed exactly [8]

$$\begin{aligned} G^{zz}(a,\bar{\phi},\bar{z}) &= -\frac{1}{(2\pi)^2} \sum_{n=-\infty}^{\infty} \int_{-\infty}^{\infty} \left(\frac{k_\rho}{k_o}\right)^2 \frac{1}{\gamma} \frac{H_n^{(2)}(\gamma)}{H_n'^{(2)}(\gamma)} e^{j(n\bar{\phi}-k_z\bar{z})} dk_z \\ G^{\phi z}(a,\bar{\phi},\bar{z}) &= -\frac{1}{(2\pi)^2} \sum_{n=-\infty}^{\infty} \int_{-\infty}^{\infty} \left(\frac{nk_z}{k_o^2 a\gamma}\right) \frac{H_n^{(2)}(\gamma)}{H_n'^{(2)}(\gamma)} e^{j(n\bar{\phi}-k_z\bar{z})} dk_z \\ G^{\phi\phi}(a,\bar{\phi},\bar{z}) &= \frac{1}{(2\pi)^2} \sum_{n=-\infty}^{\infty} \int_{-\infty}^{\infty} \frac{1}{\gamma} \left[\frac{H_n'^{(2)}(\gamma)}{H_n^{(2)}(\gamma)} - \left(\frac{nk_z}{k_o a k_\rho}\right)^2 \frac{H_n^{(2)}(\gamma)}{H_n'^{(2)}(\gamma)}\right] e^{j(n\bar{\phi}-k_z\bar{z})} dk_z \end{aligned} \tag{9}$$

where $\gamma = k_\rho a$ and $k_\rho = \sqrt{k_o^2 - k_z^2}$. However, for large radius cylinders, (9) is computationally prohibitive. In these cases, which are of main concern in this paper, it is advantageous to employ an asymptotic expression for $\overline{\overline{G}}_2$ [9, 10, 11, 12]. These employ a creeping wave series expansion of which only the two direct path contributions (see figure 3) are retained. The formula due to Pathak and Wang [9]

$$G^{zz}(a,\bar{\phi},\bar{z}) \sim -\frac{jk_o}{2\pi} q e^{-jk_o s} \left\{ \left(cos^2\theta + q(1-q)(2-3cos^2\theta)\right) v(\beta) \right\}$$

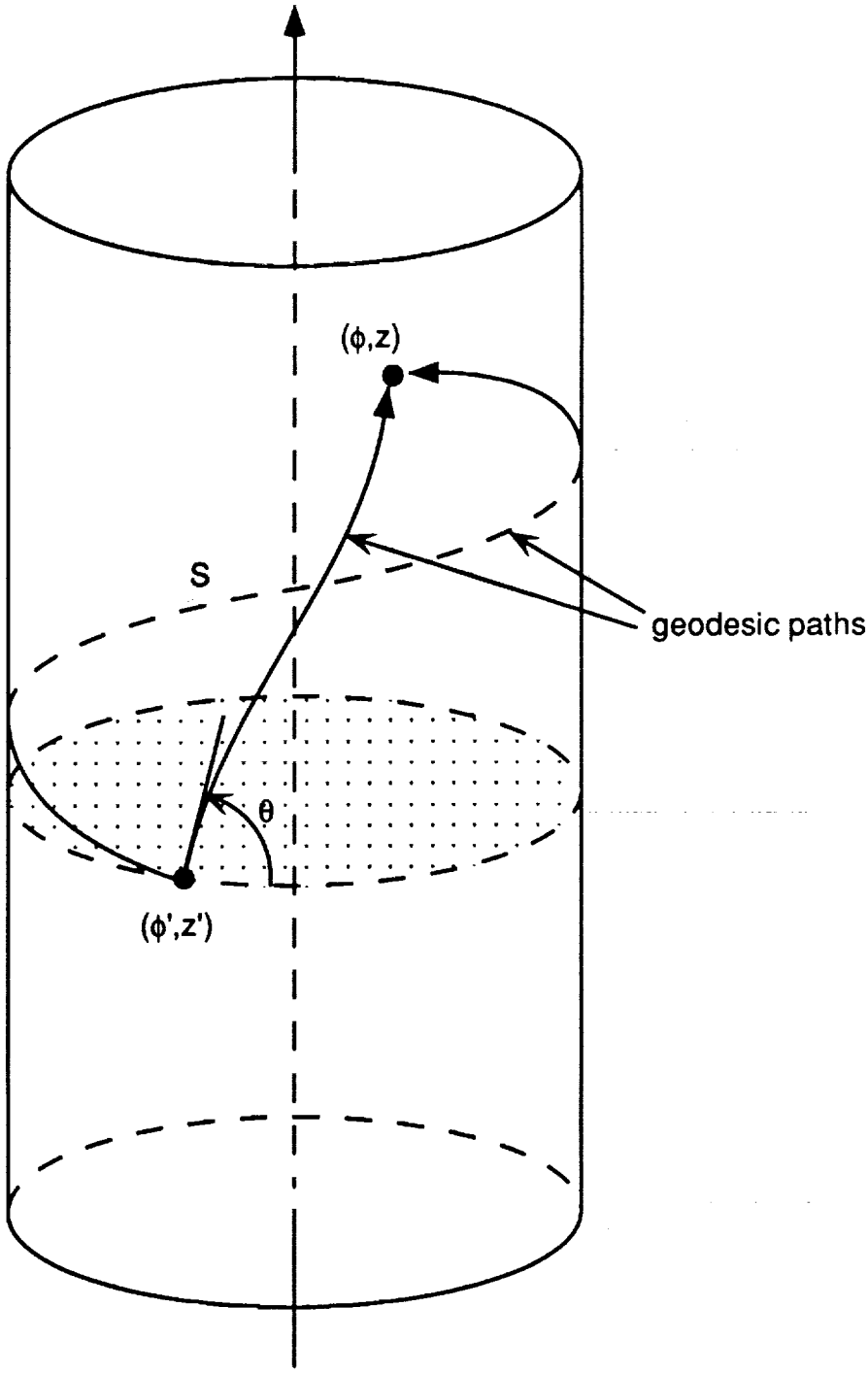

Figure 3: Geodesic paths on a circular cylinder.

$$
\begin{aligned}
G^{\phi z}(a,\bar{\phi},\bar{z}) &\sim \frac{jk_o}{2\pi}qe^{-jk_o s}\sin\theta\cos\theta\Big\{\,(1-3q(1-q))\,v(\beta)\Big\} \\
G^{\phi\phi}(a,\bar{\phi},\bar{z}) &\sim -\frac{jk_o}{2\pi}qe^{-jk_o s}\Big\{\,\Big(sin^2\theta+q(1-q)(2-3sin^2\theta)\Big)\,v(\beta) \\
&\quad +q\left[sec^2\theta\,(u(\beta)-v(\beta))\right]\Big\}
\end{aligned}
\tag{10}
$$

where $\beta = ks\left[\frac{cos^2\theta}{\sqrt{2k_o a}}\right]^{\frac{2}{3}}$ and $q = \frac{j}{k_o s}$ has proven quite accurate. In the definition of β, s is the usual geodesic path length ($s = \sqrt{(a\bar{\Phi})^2+z^2}$) and θ is the direction of the trajectory $\left(\theta = tan^{-1}\left[\frac{a\Phi}{z}\right]\right)$. Depending on which of the two direct paths (shown in figure 3) is used, $\bar{\Phi} = \bar{\phi}$ or $\bar{\Phi} = 2\pi - \bar{\phi}$. The soft and hard Fock functions, $u(\beta)$ and $v(\beta)$ respectively, are characteristic of on-surface creeping wave interactions and have been extensively investigated by Logan [13]. Although computation of the Green's function (10) is now tractable, evaluation of (8) must be done so that a discrete convolutional system is maintained and the singularity of (8) at $s = 0$ is properly treated.

Care must be taken in evaluating (8) so that the overall storage requirement remains $\mathcal{O}$(N) and the singular integrals of (8) are accurately computed. If uniform zoning is used, the resulting sub-matrix ($[\mathcal{G}]$) is block Toeplitz and hence amenable to solution using the BiCG-FFT method. For the non-selfcell contributions, mid-point integration may be used while a regularization procedure must be employed for the self-cell. Bird [12] noted that (10) recovers the metallic screen Green's function when $\beta = 0$ within the available approximation order. This suggests that (8) may be regularized by adding and subtracting from (10) the function

$$
2\overline{\overline{G}}_o(a,\bar{\phi},\bar{z}) = \left[\overline{\overline{I}}+\frac{\nabla\nabla}{k_o^2}\right]\frac{e^{-jk_oR}}{2\pi R} \quad ; \quad R = |\vec{r}-\vec{r}\,'| \tag{11}
$$

which is the free-space dyadic Green's function multiplied by two. The resulting regularized Green's function (curvature contribution) is given by

$$
\tilde{G}^{zz}(a,\bar{\phi},\bar{z}) \sim -\frac{jk_o}{2\pi}qe^{-jk_o s}\Big\{\,\Big(cos^2\theta+q(1-q)(2-3cos^2\theta)\Big)\,[v(\beta)-1]\Big\}
$$

$$\begin{aligned}
\tilde{G}^{\phi z}(a,\bar{\phi},\bar{z}) &\sim \frac{jk_o}{2\pi} q e^{-jk_o s} \sin\theta\cos\theta \Big\{ (1-3q(1-q))\,[v(\beta)-1] \Big\} \\
\tilde{G}^{\phi\phi}(a,\bar{\phi},\bar{z}) &\sim -\frac{jk_o}{2\pi} q e^{-jk_o s} \Big\{ \Big(sin^2\theta + q(1-q)(2-3sin^2\theta)\Big)\,[v(\beta)-1] \\
&\quad + q\left[sec^2\theta\,(u(\beta)-v(\beta))\right] \Big\}
\end{aligned} \tag{12}$$

and since it is no longer singular it may be evaluated numerically. The planar contribution may be calculated in the manner described previously by Jin and Volakis [5]. The FEM-BI matrix has now been fully developed and it remains to specify the excitation function for external sources.

3 Plane Wave Excitation

Plane wave excitation of the geometry is considered in this section for scattering analysis. The use of the exact boundary condition in (1) allows coupling of an exterior excitation field into the cavity. We will describe the form of the source functional, f_i^{ext}, and discuss its numerical implementation.

The forcing functional, due to exterior sources (f_i^{ext}) is given by

$$f_i^{ext} = jZ_o k_o a \int_{S_i} \vec{W}_i(a,\phi',z') \cdot \hat{\rho}(a,\phi',z') \times \vec{H}^{cyl}(a,\phi',z') d\phi'\, dz' \tag{13}$$

where $\vec{W}_i(\rho,\phi,z)$ is the testing weight for the i^{th} row of the matrix and $\vec{H}^{cyl}$ represents the magnetic field on the cylinder's surface in the absence of the cavity. A plane wave

$$\begin{aligned}
\vec{E}^i &= \hat{e}^i e^{-jk_o(\hat{k}^i\cdot\vec{r})} \\
\vec{H}^i &= Y_o(\hat{k}^i \times \hat{e}^i) e^{-jk_o(\hat{k}^i\cdot\vec{r})} \\
&= Y_o\left[\hat{\rho}^i \sin\gamma\cos\theta_i - \hat{\phi}^i\cos\gamma - \hat{z}\sin\gamma\sin\theta_i\right] e^{jk_o[\rho\sin\theta_i\cos(\phi-\phi_i)+z\cos\theta_i]}
\end{aligned} \tag{14}$$

is assumed to be incident on the cylinder from the direction (θ_i,ϕ_i) where γ is the polarization angle and $\hat{e}^i = \hat{\theta}^i\cos\gamma + \hat{\phi}^i\sin\gamma$ is the electric field polarization. The total surface field is given by the sum of the incident

and corresponding scattered field from the infinite metallic cylinder [14]. Specifically,

$$\begin{aligned}\vec{H}^{cyl}(a,\phi,z) &= \vec{H}^{i}(a,\phi,z)+\vec{H}^{s}_{cyl}(a,\phi,z)\\ &= \hat{\phi}H^{cyl}_{\phi}+\hat{z}H^{cyl}_{z}\end{aligned} \tag{15}$$

where

$$\begin{aligned}H^{cyl}_{\phi}(a,\phi,z) &= -2Y_o\frac{e^{jk_o\cos\theta_i z}}{\pi k_o a\sin\theta_i}\sum_{n=-\infty}^{\infty}\left[\frac{\cos\gamma}{H^{(2)}_n(k_oa\sin\theta_i)}+\right.\\ &\qquad \left. j\frac{n}{k_oa\sin\theta_i}\frac{\sin\gamma\cos\theta_i}{H^{\prime(2)}_n(k_oa\sin\theta_i)}\right]e^{jn(\frac{\pi}{2}+\phi-\phi_i)}\\ H^{cyl}_{z}(a,\phi,z) &= j2Y_o\frac{\sin\gamma}{\pi k_o a}e^{jk_o\cos\theta_i z}\sum_{n=-\infty}^{\infty}\left[\frac{e^{jn(\frac{\pi}{2}+\phi-\phi_i)}}{H^{\prime(2)}_n(k_oa\sin\theta_i)}\right]\end{aligned} \tag{16}$$

is obtained from traditional modal analysis. These expressions may be approximated by retaining only a few terms of the series if $k_oa\sin\theta_i$ is small. However, as this parameter becomes large (e.g. for large a and $\theta_i \rightarrow 90^o$), (16) may be replaced with equivalent asymptotic representations similar to those considered earlier. Utilizing Watson's transformation and Fock theory [14] in connection with (16), we find that

$$\begin{aligned}H^{cyl}_{z} &\sim -Y_o\sin\gamma\sin\theta_i e^{jk_o\cos\theta_i z}\sum_{p=1}^{2}e^{-jk_oa\sin\theta_i\Phi_p}\left[g^{(0)}(m\Phi_p)\right]^*\\ H^{cyl}_{\phi} &\sim j2Y_o\cos\gamma\frac{m^2}{k_oa\sin\theta_i}e^{jk_o\cos\theta_i z}\sum_{p=1}^{2}e^{-jk_oa\sin\theta_i\Phi_p}\left[f^{(0)}(m\Phi_p)\right]^*\\ &\quad -Y_o\sin\gamma\cos\theta_i e^{jk_o\cos\theta_i z}\sum_{p=1}^{2}(-1)^p e^{-jk_oa\sin\theta_i\Phi_p}\left[g^{(0)}(m\Phi_p)\right.\\ &\qquad \left.-j\frac{m}{k_oa\sin\theta_i}g^{(1)}(m\Phi_p)\right]^*\end{aligned} \tag{17}$$

in which $\Phi_1 = \frac{3\pi}{2}-(\phi-\phi_i)$, $\Phi_2 = (\phi-\phi_i)-\frac{\pi}{2}$, $m = \left[\frac{k_oa\sin\theta_i}{2}\right]^{\frac{1}{3}}$, and complex conjugation is denoted by an asterisk. The appropriate far-zone Fock functions ($g^{(0)}$, $g^{(1)}$ and $f^{(0)}$) are given by Logan [13].

The asymptotic formulas (17) are quite accurate except in the geometrical optics region ($\phi \approx \phi_i$). In this case, Goriainov's [15] expressions

$$
\begin{aligned}
H_z^{cyl} \sim\ & -Y_o \sin\alpha \sin\theta_i e^{jk_o \cos\theta_i z} \Big\{ e^{-jk_o a \sin\theta_i \Phi_1} \left[g^{(0)}(m\Phi_1) \right]^* \\
& + e^{jk_o a \sin\theta_i \cos(\phi-\phi_i)} \left[G(-m\cos(\phi-\phi_i)) \right]^* \Big\} \\
H_\phi^{cyl} \sim\ & j2Y_o \cos\alpha \frac{m^2}{k_o a \sin\theta_i} e^{jk_o \cos\theta_i z} \Big\{ e^{-jk_o a \sin\theta_i \Phi_1} \left[f^{(0)}(m\Phi_1) \right]^* \\
& + e^{jk_o a \sin\theta_i \cos(\phi-\phi_i)} \left[F(-m\cos(\phi-\phi_i)) \right]^* \Big\} \\
& + Y_o \sin\alpha \cos\theta_i e^{jk_o \cos\theta_i z} \Big\{ e^{-jk_o a \sin\theta_i \Phi_1} \Big[g^{(0)}(m\Phi_1) \\
& - j \frac{m}{k_o a \sin\theta_i} g^{(1)}(m\Phi_1) \Big]^* \\
& - e^{jk_o a \sin\theta_i \cos(\phi-\phi_i)} \Big[G(-m\cos(\phi-\phi_i)) \\
& - j \frac{m}{k_o a \sin\theta_i} G^{(1)}(-m\cos(\phi-\phi_i)) \Big]^* \Big\}
\end{aligned}
\tag{18}
$$

have been found to be more accurate and can be used instead of (17). The Fock functions (G, $G^{(1)}$ and F) are again defined in Logan [13]. These surface field expressions may be used to calculate the entries of the column vector $\{f_i^{ext}\}$ efficiently via a numerical evaluation of (13). In particular, the modal series (16) is used when $k_o a \sin\theta_i \leq 10$ and either (17) or (18) for $k_o a \sin\theta_i > 10$ as appropriate. With the excitation functional and the FEM-BI matrix now specified, the BiCG-FFT method [16, 17] may be used to determine the unknown electric fields within the cavity.

4 Scattering

Once the cavity aperture and volume electric fields have been determined by solving (2) for an external excitation, the radar cross section (RCS) may be calculated. The far-zone fields may be computed by integrating the aperture fields with a suitable Green's function. In this section we present the relevant

formula for calculating the far-zone fields and hence the RCS due to excitation by a plane wave (14).

To determine the far-zone fields, we begin with the integral representation for the scattered magnetic field in terms of the aperture fields. We have

$$\begin{aligned}\vec{H}^s(r,\theta,\phi) &= jY_o k_o a \int_S \overline{\overline{G}}_2(r,\theta,\phi;a,\phi',z') \cdot \\ &\quad \left[\hat{\rho}(a,\phi',z') \times \vec{E}(a,\phi',z')\right] d\phi'\, dz' \end{aligned} \tag{19}$$

with (r,θ,ϕ) indicating the observation point in spherical coordinates. When the observation point is very far from the cylinder, the dyadic Green's function in (19) can be replaced by its far-zone representation

$$\overline{\overline{G}}_2(r,\theta,\phi;a,\phi',z') \sim \frac{e^{-jk_o r}}{k_o r}\left[G^{\theta\phi}\hat{\theta}\hat{\phi}' + G^{\theta z}\hat{\theta}\hat{z} + G^{\phi\phi}\hat{\phi}\hat{\phi}'\right] \tag{20}$$

where the unprimed unit vectors are functions of the observation position and the primed ones are functions of the integration point in (19). The components of this far-zone Green's function

$$\begin{aligned} G^{\theta\phi} &\sim \frac{j}{(2\pi)^2}\frac{2k_o\cos\theta}{(k_o a\sin\theta)^2}e^{jk_o\cos\theta z'}\sum_{n=-\infty}^{\infty}\frac{n}{H_n'^{(2)}(k_o a\sin\theta)}e^{jn(\frac{\pi}{2}+(\phi-\phi'))} \\ G^{\theta z} &\sim \frac{j}{(2\pi)^2}\frac{2}{a}e^{jk_o\cos\theta z'}\sum_{n=-\infty}^{\infty}\frac{1}{H_n'^{(2)}(k_o a\sin\theta)}e^{jn(\frac{\pi}{2}+(\phi-\phi'))} \\ G^{\phi\phi} &\sim \frac{j}{(2\pi)^2}\frac{2}{a\sin\theta}e^{jk_o\cos\theta z'}\sum_{n=-\infty}^{\infty}\frac{1}{H_n^{(2)}(k_o a\sin\theta)}e^{jn(\frac{\pi}{2}+(\phi-\phi'))} \end{aligned} \tag{21}$$

are determined by a mode matching procedure. As one might expect, these series converge rather slowly for large $k_o a\sin\theta$. They must therefore be recast in another form by employing Watson's transformation and Fock theory as was done previously (17). In doing so, we obtain

$$\begin{aligned} G^{\theta\phi} &\sim \frac{k_o\cos\theta}{4\pi}e^{jk_o\cos\theta z'}\sum_{p=1}^{2}(-1)^p e^{-jk_o a\sin\theta\Phi_p}\left[g^{(0)}(m\Phi_p) - j\frac{m}{k_o a\sin\theta}g^{(1)}(m\Phi_p)\right]^* \\ G^{\theta z} &\sim -\frac{k_o\sin\theta}{4\pi}e^{jk_o\cos\theta z'}\sum_{p=1}^{2}e^{-jk_o a\sin\theta\Phi_p}\left[g^{(0)}(m\Phi_p)\right]^* \\ G^{\phi\phi} &\sim \frac{m^2}{2a\pi\sin\theta}e^{jk_o\cos\theta z'}\sum_{p=1}^{2}e^{-jk_o a\sin\theta\Phi_p}\left[f^{(0)}(m\Phi_p)\right]^* \end{aligned} \tag{22}$$

where the Fock functions are the same as those used with (17) due to reciprocity. As was the case for the plane wave source, Goriainov's [15] approximations are more accurate in the geometrical optics region ($\phi' \approx \phi$) and similar expressions may be obtained for (22) as was found for (17). The far-zone scattered field can be computed numerically by using (19) and either the series or asymptotic formula as appropriate. Having done so, the RCS is calculated from

$$\sigma(\theta,\phi) = \lim_{r\to\infty} 4\pi r^2 \frac{|\vec{H}^s(r,\theta,\phi)|}{|\vec{H}^i(r,\theta,\phi)|} \tag{23}$$

Above we presented a FEM-BI formulation suitable for modeling cavity-backed structures embedded in a circular cylinder. Next, we consider a few numerical calculations aimed at validating this formulation and in giving us an appreciation on how the cylinder's curvature influences the scattering parameters.

5 Results

Having solved for the electric fields induced by an incident plane wave, the resulting RCS data must be validated with known results. As previously mentioned, available measured or computed data is rather scarce and as a consequence, we are forced to rely on limiting cases in order to validate this work. As the radius of curvature decreases, a cylindrical-rectangular cavity will approximate a planar-rectangular cavity. Another limiting case involves comparison of an elongated 3-D cavity with a corresponding 2-D cavity for normal incidence ($\theta_i = 90°$). Finally, we may compare our infinite cylinder results with a finite Body of Revolution (BOR) model for certain polarizations and angles of incidence. We begin with the quasi-planar case.

The first validation effort for scattering by cavity-backed patch antennas relies on the fact that a small patch on a very large radius cylinder is quasi-planar and approximates rather well an equal sized planar patch. For our test we chose as a reference a planar $1.448'' \times 1.083''$ patch residing on a $2.89'' \times 2.10'' \times 0.057''$ cavity filled with a dielectric having $\epsilon_r = 4$. The equivalent patch on a 10λ cylinder is $6.46° \times 1.083''$ residing on a $12.90° \times 2.10'' \times 0.057''$ cavity. Figure 4 shows the results for the patch on a large radius cylinder with corresponding data for the planar cavity-backed patch. Clearly, the two

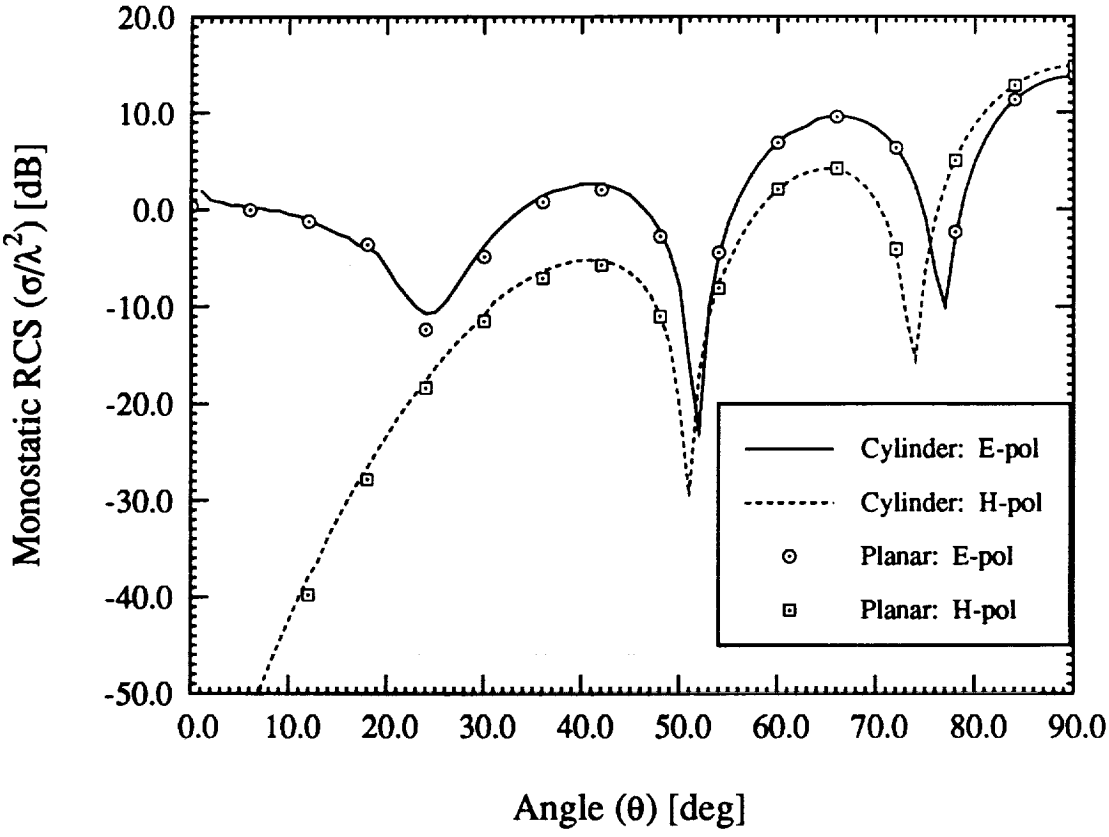

Figure 4: Comparison of RCS for a planar patch ($1.488'' \times 1.083''$) residing on a $2.89'' \times 2.10'' \times 0.059''$ cavity filled with $\epsilon_r = 4$ dielectric and a corresponding quasi-planar patch on a large radius ($10\lambda_0$) cylinder.

RCS patterns are in excellent agreement, and although figure 4 illustrates only monostatic scattering in the $\phi = 0^o$ plane, additional runs for normally incident monostatic scattering and various bistatic situations yield similar agreement.

Comparisons may also be made for elongated cavities and 2-D MoM results. Long narrow cavities have very little axial interaction for principal plane ($\theta = 90^o$) excitation and therefore results based on this formulation should compare well with corresponding 2-D data. It is well known that the RCS of the 3-D scattering body of length $L \gg \lambda_0$ is related to the corresponding 2-D scattering of the same cross section via the relation

$$\sigma_{3D} = 2\left(\frac{L}{\lambda_0}\right)^2 \sigma_{2D} \tag{24}$$

Such a comparison is shown in figure 5 for monostatic scattering by a $45^o \times 5\lambda \times 0.1\lambda$ cavity for both principal polarizations. Once again the agreement between the two results is excellent, thus providing a partial validation of the formulation for highly curved geometries. We remark that similar agreement has been observed for bistatic scattering in the $\theta = 90^o$ plane.

The planar approximation eliminates the effects of curvature, which is a primary interest in this work, and the 2-D comparisons done above are only valid for normal incidence. To consider oblique incidence on a highly curved structure, we resort to comparisons with a Body of Revolution (BOR) code for wraparound cavities. Since the BOR code can only model finite structures, we simulate an infinite cylinder by coherently subtracting the far-zone fields of the finite structure without a cavity from similar data which includes the cavity. Such an procedure mimics common measurement practices and was found suitable for near normal incidence and quite acceptable near grazing incidence in the case of H-polarization ($\alpha = 90^o$). An example calculation for the latter case is given in figure 6 where a bistatic scattering pattern is presented in the $\phi = 0^o$ plane due to a plane wave incident at ($\theta_i = 90^o$,$\phi_i = 0^o$). Clearly, there is good agreement between the FEM-BI results and data based on the BOR formulation.

The previous comparisons serve to validate the formulation. Having done so, it is instructive to examine the effect that curvature has on the scattering properties of cavity-backed patch antennas. Consider a 2 cm $\times$ 3 cm patch residing on a 5.0 cm $\times$ 6.0 cm $\times$ 0.07874 cm cavity which is filled with a dielectric having $\epsilon_r = 2.17$. Figures 7 and 8 illustrate the behavior of

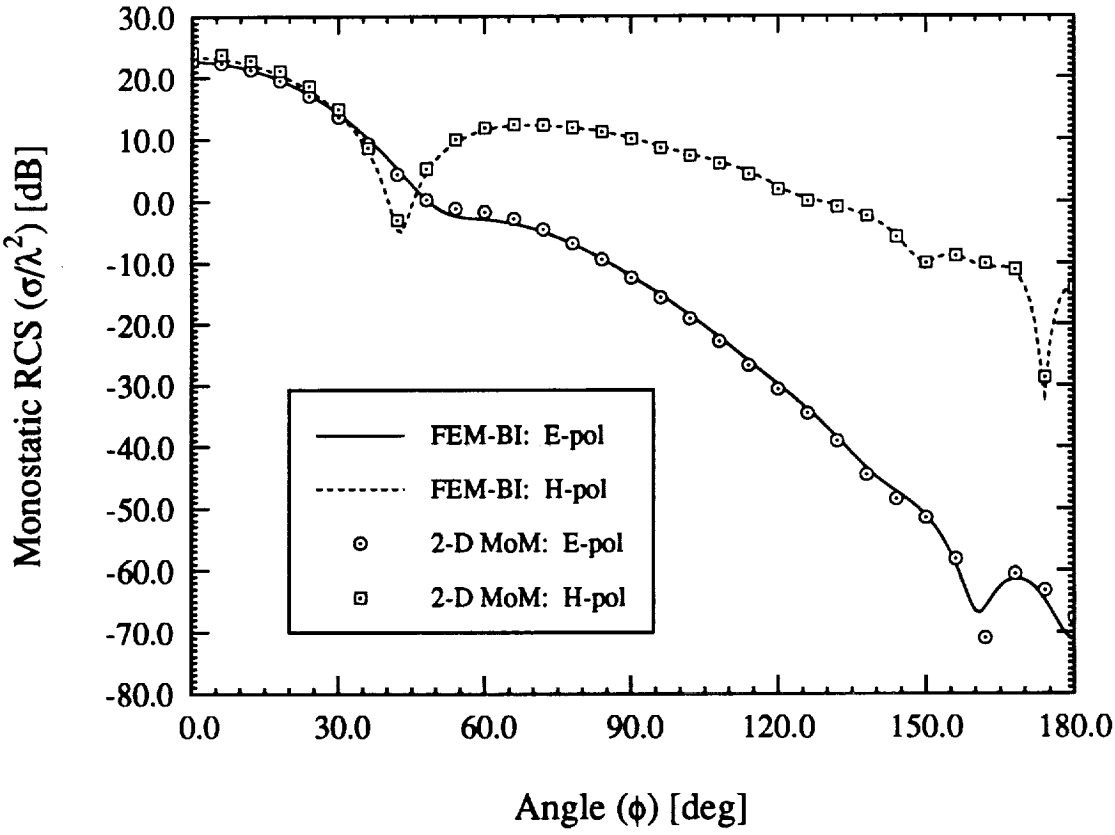

Figure 5: Comparison of 2-D MoM results and FEM-BI RCS results for a $45^o \times 5\lambda_0 \times 0.1\lambda_0$ air-filled cavity.

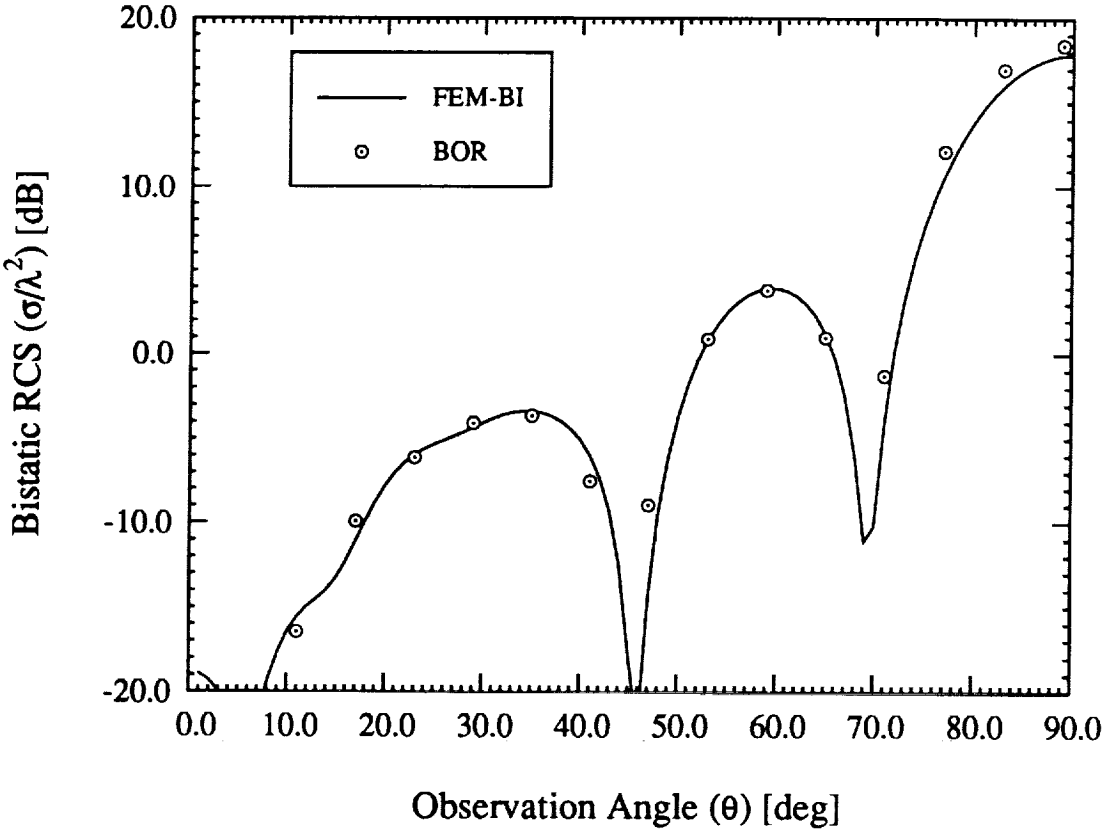

Figure 6: Comparison of the RCS computed via the FEM-BI method and a BOR code for a $3\lambda_0 \times 0.1\lambda_0$ air-filled wraparound cavity excited by a normally incident H-polarized ($\alpha = 90°$) plane wave.

this geometry as a function of frequency and curvature. Evidently, the resonance behavior of this patch is sensitive to curvature for both principal polarizations. The frequency response for E-polarization is more sensitive to curvature since the radiating surface field component is parallel to the long side of the patch and cavity. If the patch and cavity were oriented so that the long side is in the $\hat{\phi}$-direction, the response to H-polarization would exhibit greater sensitivity. Such an effect is important to low observable antenna designers since they want to operate the antenna in the region of lowest RCS. This low return region is a consequence of delicate cancellations due to the physical layout of the aperture. Such cancellations are not as complete for highly curved structures as they are for planar cavities.

Conformal antenna designers often use wraparound antennas to achieve omnidirectional coverage. Two different configurations are typically used: a wraparound cavity where the cavity is filled with a single continuous collar of dielectric and discrete cavities symmetrically placed around the circumference of the cylinder. These two configurations are shown in figure (9). Since near resonance, the radiation properties of these two types of antennas is identical, any RCS advantage which one might possess could govern the appropriate choice of arrays. Figure 10 compares the E-polarized monostatic scattering at 3 GHz in the $\theta = 90°$ plane for a wraparound cavity and four discrete cavities; where the patches and cavities are identical to those used in the previous example. Not surprisingly, the wraparound structure has a higher return due to coupling within the substrate. However, since in this case the scattered field is due to the z component of the surface field (ϕ-directed magnetic currents), both cavities yield large scattered fields in the four directional lobes. Figure 11 is the corresponding comparison for H-polarization. In this case, the scattered field is attributed to the ϕ component of the surface fields (z-directed magnetic currents). Therefore, substrate modes diffract near the patch resulting in discrete lobes for the discrete array while creeping waves shed isotropically for the continuous wraparound cavity. Low observable designs will favor discrete cavity arrays over wraparound cavities since the scattering may be channeled in preferred directions and the overall scattering level is consistently lower. A final example is shown in figure 12 where we observe that other than the expected higher scattering from the wraparound cavity, the scattering behavior of the two arrays is very similar.

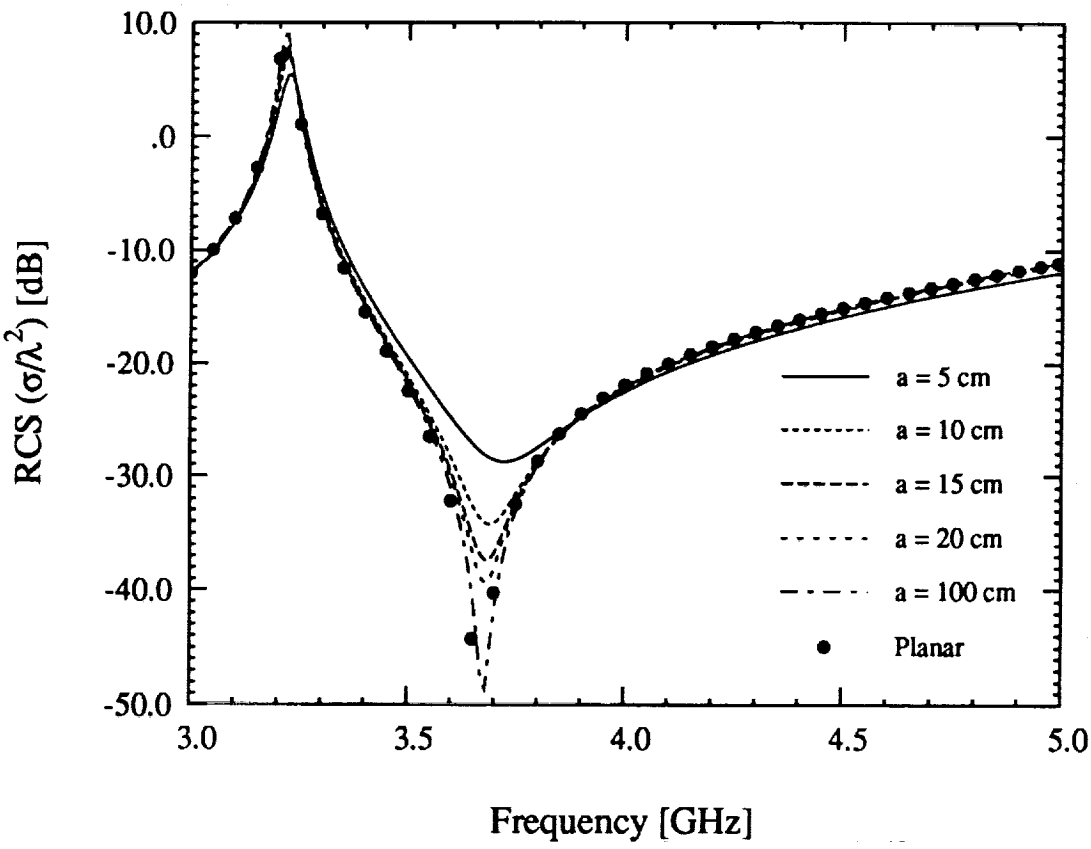

Figure 7: RCS frequency response for a 2 cm $\times$ 3 cm $\times$ patch residing in a 5 cm $\times$ 6 cm $\times$ 0.07874 cm cavity with $\epsilon_r = 2.17$ as a function of curvature for E-polarization ($\alpha = 0^o$).

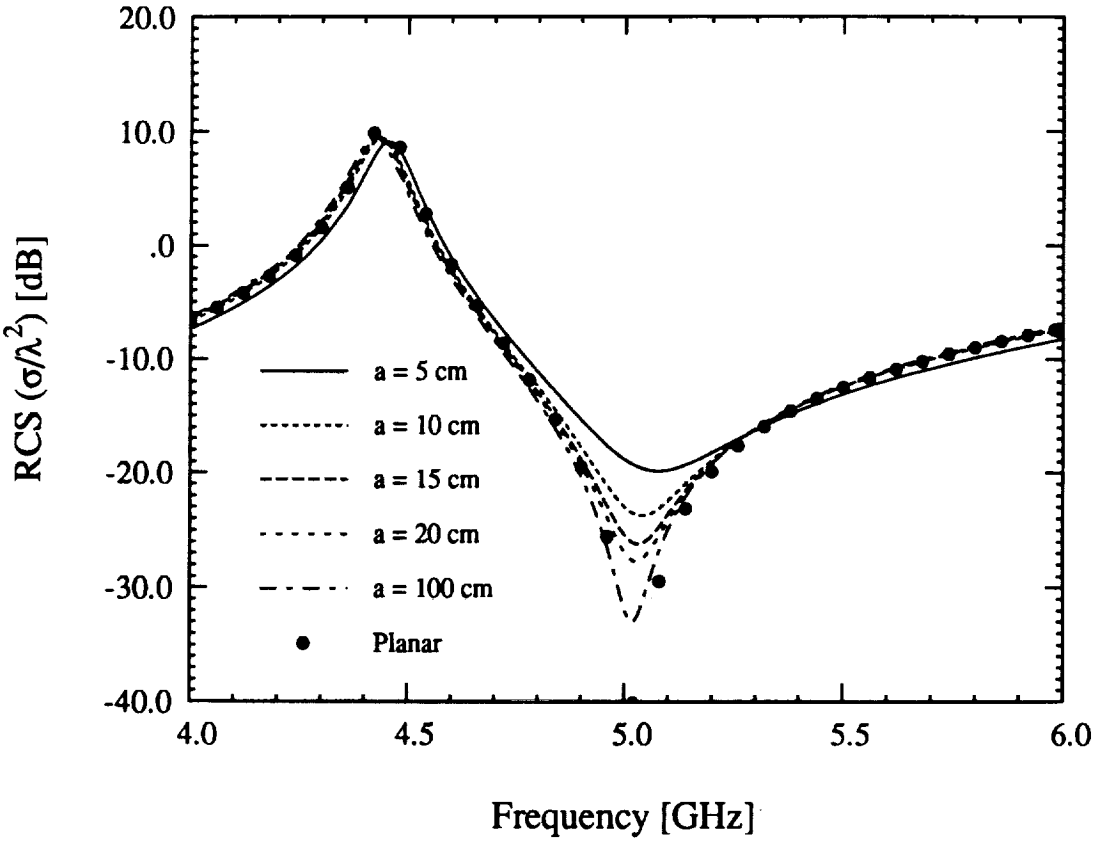

Figure 8: RCS frequency response for a 2 cm × 3 cm × patch residing in a 5 cm × 6 cm × 0.07874 cm cavity with $\epsilon_r = 2.17$ as a function of curvature for H-polarization ($\alpha = 90°$).

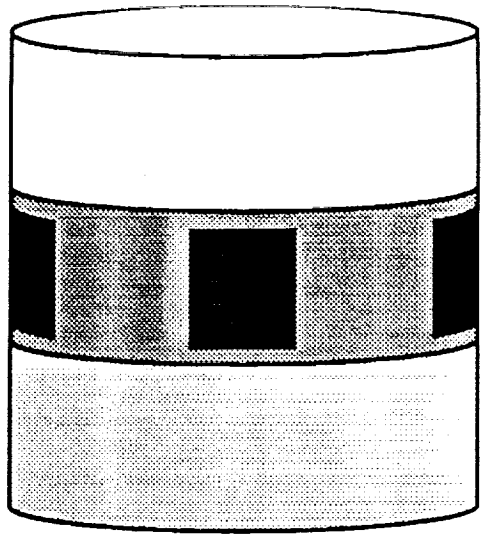

(a)

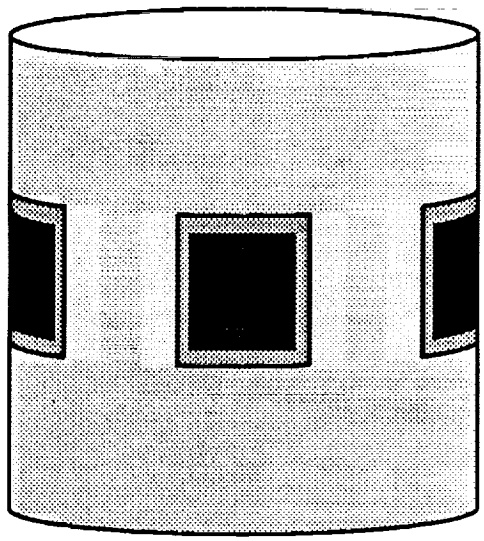

(b)

Figure 9: Illustration of two types of arrays: (a) wraparound array; (b) discrete cavity array

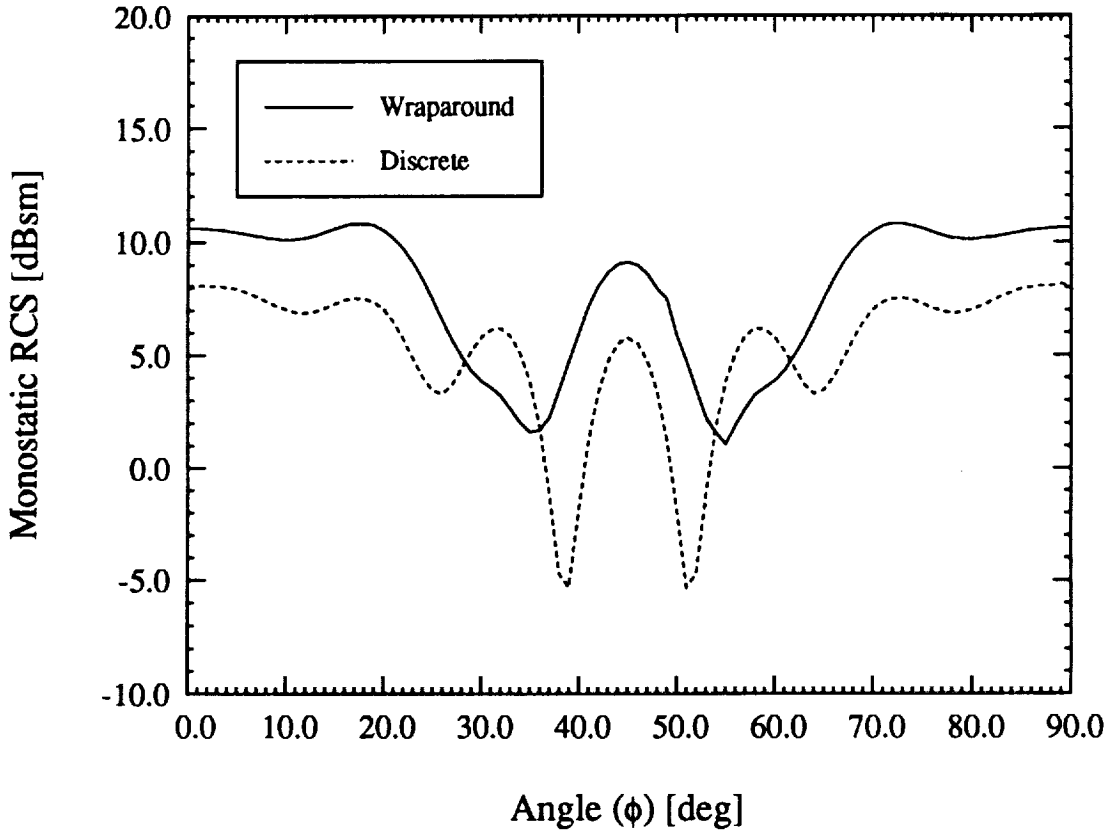

Figure 10: Comparison of E-polarized monostatic RCS at 3 GHz for a four patch array placed on a wraparound collar or in four discrete cavities. The patches and cavities are identical to the one used in figure 7. The observation plane is $\theta = 90^{o}$.

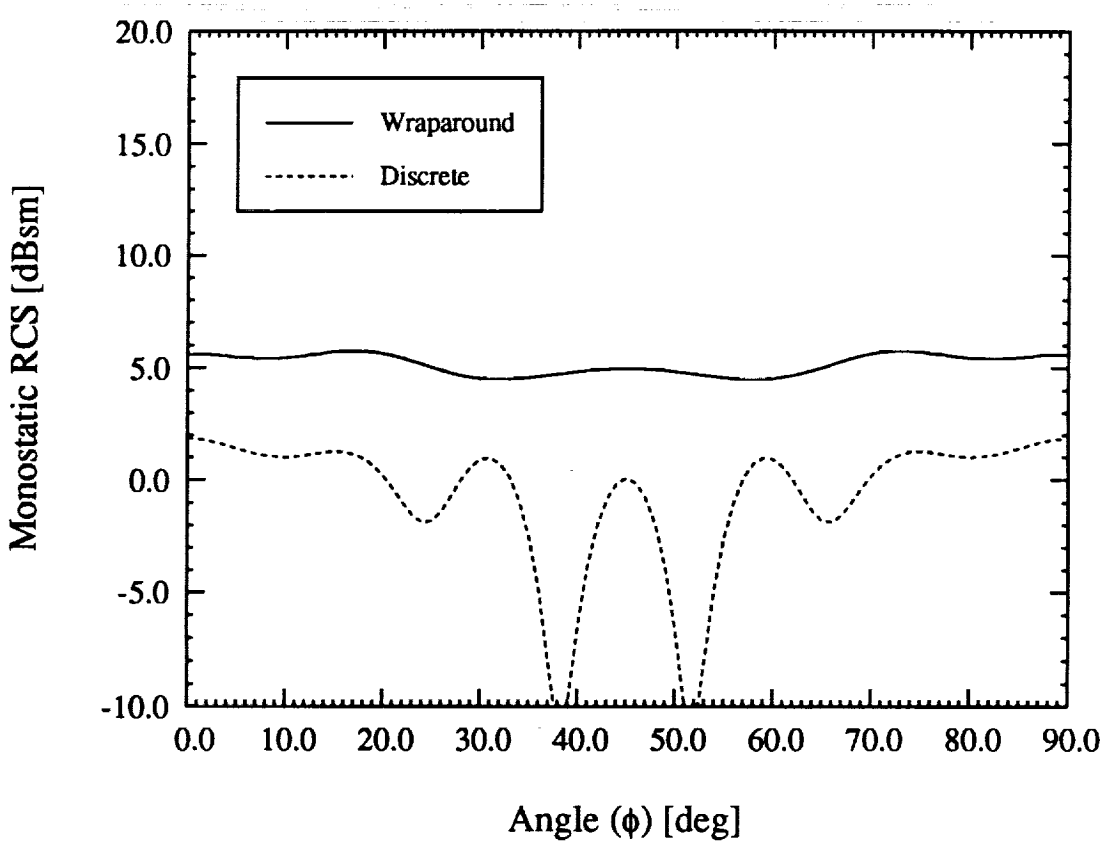

Figure 11: Comparison of H-polarized monostatic RCS at 3 GHz for a four patch array placed on a wraparound collar or in four discrete cavities. The patches and cavities are identical to the one used in figure 8. The observation plane is $\theta = 90^{o}$.

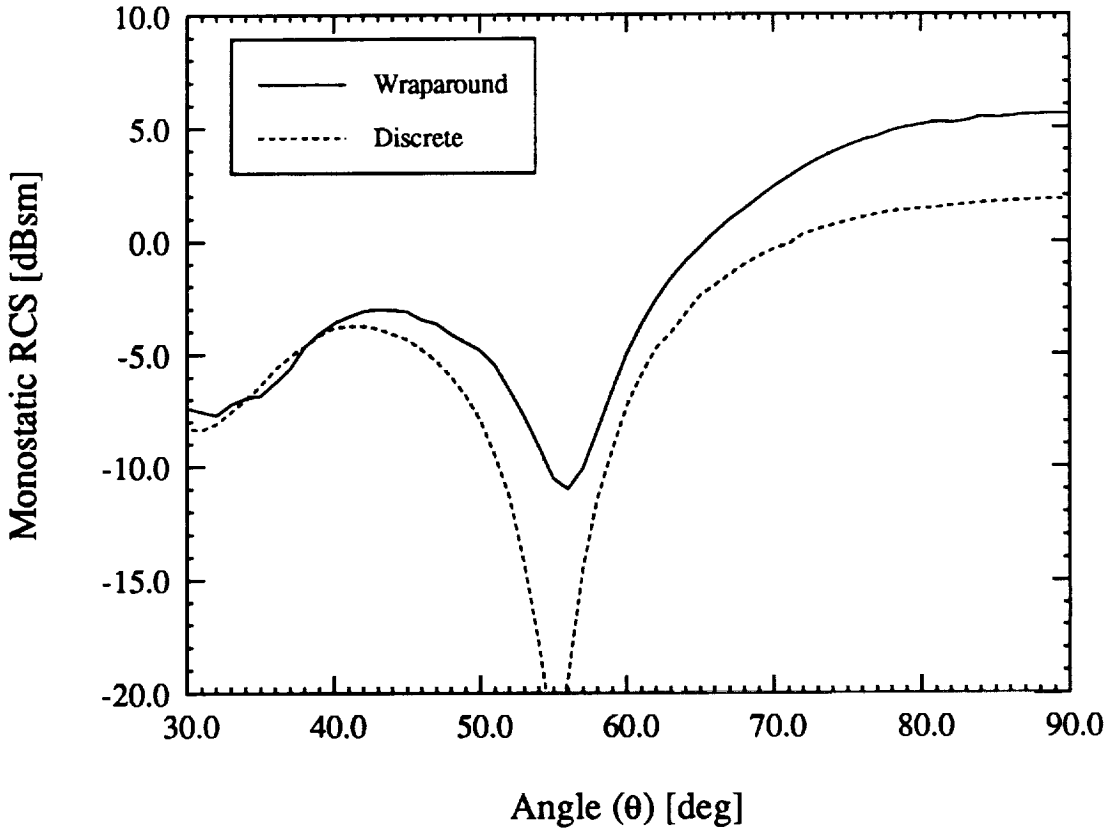

Figure 12: Comparison of H-polarized monostatic scattering at 3 GHz by a four patch array placed on a wraparound collar or in four discrete cavities. The patches and cavities are identical to the one used in figure 8. The observation plane is $\phi = 0°$.

6 Conclusions

In this paper, we have presented a Finite Element Method - Boundary Integral technique suitable for electromagnetic scattering calculations for cavities embedded within a circular, metallic cylinder. This formulation is analogous to the FEM-BI approach used by Jin and Volakis [1, 5, 6] and may accordingly be used for the analysis of scattering by a large array of cavity-backed patch antennas. These cavities need not be identical, periodically spaced or homogeneously filled and may in fact may possess lumped impedance loads or surface metallization layers. The FEM approach employs vector finite elements which properly represent the electromagnetic fields and possess high geometrical fidelity for cylindrical-rectangular cavities. Such elements were presented and are analogous to the bricks used for modeling rectangular cavities. In addition, we presented an efficient method for evaluating the on-surface and far-zone dyadic Green's functions. The presented formulation is amenable to solution using the BiCG-FFT method provided uniform zoning is used across the aperture and as a consequence, this implementation has low computational and memory demand. We have presented some validation of this work with appropriate limiting cases which provides further archival reference data. In addition, we showed how this formulation may be used to influence conformal antenna designs.

References

[1] J-M Jin and J.L. Volakis, "A hybrid finite element method for scattering and radiation by microstrip patch antennas and arrays residing in a cavity," *IEEE Trans. Antennas and Propagat.*, Vol. 39, No. 11, pp. 1598-1604, Nov. 1991.

[2] J.L. Volakis, A. Chatterjee and J. Gong, "A class of hybrid finite element methods for electromagnetics: A review," to appear in *J. Electromagnetic Waves Appl.*, 1994.

[3] Z.J. Cendes, "Vector finite elements for electromagnetic field computation," *IEEE Trans. Magnetics*, Vol. 27, No. 5, pp. 3958-3966, Sept. 1991.

[4] A. Bossavit, "A rationale for edge-elements in 3D fields computations," *IEEE Trans. Magnetics* Vol. 24, No. 1, pp. 74-79, Jan 1988.

[5] J-M Jin and J.L. Volakis, "A finite element-boundary integral formulation for scattering by three-dimensional cavity-backed apertures," *IEEE Trans. Antennas and Propagat.*, Vol. 39, No. 1, pp. 97-104, Jan. 1991.

[6] J-M Jin and J.L. Volakis, "Electromagnetic scattering by and transmission through a three-dimensional slot in a thick conducting plane," *IEEE Trans. Antennas and Propagat.*, Vol. 39, No. 4, pp. 543-550, Apr. 1991.

[7] A. Chatterjee, J-M. Jin, and J.L. Volakis, "Computation of cavity resonances using edge-based finite elements," *IEEE Trans. Microwave Theory Tech.*, Vol. 40, No. 11, pp. 2106-2108, Nov. 1992.

[8] C-T Tai, *Dyadic Green's Functions in Electromagnetic Theory* . International Textbook Co., Scranton, 1971.

[9] P.H. Pathak and N.N. Wang, "An analysis of the mutual coupling between antennas on a smooth convex surface," *Ohio State Univ. Electro-Science Lab.*, Report 784583-7, Oct. 1978.

[10] J. Boersma and S.W. Lee, "Surface field due to a magnetic dipole on a cylinder: Asymptotic expansions of exact solution," *Univ. Illinois Electromagnetics Lab.*, Report 78-17, 1978.

[11] T.S. Bird, "Comparison of asymptotic solutions for the surface field excited by a magnetic dipole on a cylinder," *IEEE Trans. Antennas and Propagat.*, Vol. 32, No. 11, pp. 1237-1244, Nov. 1984.

[12] T.S. Bird, "Accurate asymptotic solution for the surface field due to apertures in a conducting cylinder," *IEEE Trans. Antennas and Propagat.*, Vol. 33, No. 10, pp. 1108-1117, Oct. 1985.

[13] N. A. Logan, "General research in diffraction theory," *Lockheed Aircraft Corp., Missiles and Space Div.*, vol. 1 and 2, Report LMSD-288088, Dec. 1959.

[14] O. Einarsson, R.E. Kleinman, P. Laurin, and P.L.E. Uslenghi, "Studies in radar cross sections L - Diffraction and scattering by regular bodies IV: The circular cylinder," *University of Michigan Technical Report* No. 7133-3-T, 1966.

[15] A.S. Goriainov, "An asymptotic solution of the problem of diffraction of a plane electromagnetic wave by a conducting cylinder," *Radio Engr. and Electr. Phys.*, Vol. 3, pp. 23-39 , 1958. (English translation of *Radiotekhnica i Elektronica*, Vol. 3)

[16] T.K. Sarkar, "On the application of the generalized biconjugate gradient method," *J. Electromagnetic Waves Appl.*, Vol. 1, No. 3, pp. 223-242, 1987.

[17] C.F. Smith, A.F. Peterson and R. Mittra, "The biconjugate gradient method for electromagnetic scattering," *IEEE Trans. Antennas and Propagat.*, Vol. 38, No. 6, pp. 938-940, June 1990.

Appendices

A FEM Matrix Entries

The matrix entries for the FEM portion of the system (5) are given in this appendix assuming that the cylindrical shell elements (4) are used in (6). These integrals are given by

$$
\begin{aligned}
I_{\rho\rho}^{(1)} &= \frac{\tilde{s}_s\tilde{s}_t}{(\alpha h)^2}\left[\rho_b^2 h \ln\left(\frac{\rho_b}{\rho_a}\right)\int_{\phi_l}^{\phi_r}(\phi-\tilde{\phi}_s)(\phi-\tilde{\phi}_t)d\phi + \right. \\
&\qquad \left. \frac{\alpha}{2}\left(\frac{\rho_b^2}{\rho_a^2}-1\right)\int_{z_b}^{z_t}(z-\tilde{z}_s)(z-\tilde{z}_t)dz\right] \\
I_{\rho\phi}^{(1)} &= -\frac{\tilde{s}_s\tilde{s}_t}{th^2}\left[2\rho_b\ln\left(\frac{\rho_b}{\rho_a}\right)+\tilde{\rho}_t\left(1-\frac{\rho_b}{\rho_a}\right)\right]\int_{z_b}^{z_t}(z-\tilde{z}_s)(z-\tilde{z}_t)dz \\
I_{\rho z}^{(1)} &= -\frac{\tilde{s}_s\tilde{s}_t\rho_b}{\alpha^2}\int_{\phi_l}^{\phi_r}(\phi-\tilde{\phi}_s)(\phi-\tilde{\phi}_t)d\phi \\
I_{\phi\phi}^{(1)} &= \frac{\tilde{s}_s\tilde{s}_t\alpha}{(th)^2}\left[h\left(\frac{1}{4}\left(\rho_b^4-\rho_a^4\right)+\frac{1}{3}\left(\tilde{\rho}_s+\tilde{\rho}_t\right)\left(\rho_a^3-\rho_b^3\right)+\frac{1}{2}\tilde{\rho}_s\tilde{\rho}_t\left(\rho_b^2-\rho_a^2\right)\right)+\right. \\
&\qquad \left.\left(2\left(\rho_b^2-\rho_a^2\right)-2t\left(\tilde{\rho}_s+\tilde{\rho}_t\right)+\tilde{\rho}_s\tilde{\rho}_t\ln\left(\frac{\rho_b}{\rho_a}\right)\right)\int_{z_b}^{z_t}(z-\tilde{z}_s)(z-\tilde{z}_t)dz\right] \\
I_{\phi z}^{(1)} &= -\frac{\tilde{s}_s\tilde{s}_t}{t^2}\int_{\rho_a}^{\rho_b}(\rho-\tilde{\rho}_s)(\rho-\tilde{\rho}_t)d\rho \\
I_{zz}^{(1)} &= \frac{\tilde{s}_s\tilde{s}_t h}{(t\alpha)^2}\left[\alpha\left(\frac{1}{2}\left(\rho_b^2-\rho_a^2\right)-t\left(\tilde{\rho}_s+\tilde{\rho}_t\right)+\tilde{\rho}_s\tilde{\rho}_t\ln\left(\frac{\rho_b}{\rho_a}\right)\right)+\right. \\
&\qquad \left.\frac{1}{2}\left(\rho_b^2-\rho_a^2\right)\int_{\phi_l}^{\phi_r}(\phi-\tilde{\phi}_s)(\phi-\tilde{\phi}_t)d\phi\right] \\
I_{\rho\rho}^{(2)} &= \frac{\tilde{s}_s\tilde{s}_t\rho_b^2}{(\alpha h)^2}\ln\left(\frac{\rho_b}{\rho_a}\right)\int_{\phi_l}^{\phi_r}(\phi-\tilde{\phi}_s)(\phi-\tilde{\phi}_t)d\phi\int_{z_b}^{z_t}(z-\tilde{z}_s)(z-\tilde{z}_t)dz \\
I_{\phi\phi}^{(2)} &= \frac{\tilde{s}_s\tilde{s}_t\alpha}{(th)^2}\left[\frac{1}{4}\left(\rho_b^4-\rho_a^4\right)+\frac{1}{3}\left(\tilde{\rho}_s+\tilde{\rho}_t\right)\left(\rho_a^3-\rho_b^3\right)+\frac{1}{2}\tilde{\rho}_s\tilde{\rho}_t\left(\rho_b^2-\rho_a^2\right)\right]\times \\
&\qquad \int_{z_b}^{z_t}(z-\tilde{z}_s)(z-\tilde{z}_t)dz \\
I_{zz}^{(2)} &= \frac{\tilde{s}_s\tilde{s}_t h}{(t\alpha)^2}\left[\frac{1}{4}\left(\rho_b^4-\rho_a^4\right)+\frac{1}{3}\left(\tilde{\rho}_s+\tilde{\rho}_t\right)\left(\rho_a^3-\rho_b^3\right)+\frac{1}{2}\tilde{\rho}_s\tilde{\rho}_t\left(\rho_b^2-\rho_a^2\right)\right]\times
\end{aligned}
$$

$$\int_{\phi_l}^{\phi_r} (\phi - \tilde{\phi}_s)(\phi - \tilde{\phi}_t) d\phi \qquad \text{(A-1)}$$

Each of the above unevaluated integrals is of the form

$$\int_L^U \left(\xi - \tilde{\xi}_s\right)\left(\xi - \tilde{\xi}_t\right) d\xi = \frac{1}{2}\left(L^2 - U^2\right)\left(\tilde{\xi}_s + \tilde{\xi}_t\right) + \frac{1}{3}\left(U^3 - L^3\right) + \tilde{\xi}_s\tilde{\xi}_t\,(U - L) \qquad \text{(A-2)}$$

The integrals $I_{st}^{(1),(2)}$ are used in the assembly of the FEM portion ($[\mathcal{A}]$) of the system.

B Fock Functions

The asymptotic form of the dyadic Green's function with observation both on the surface of the cylinder and in the far field involves Fock functions. These have been extensively studied and tabulated by Logan [13]. The numerical evaluation of these functions are performed either for small arguments or large arguments.

The on-surface Fock functions used in this paper are

$$\begin{aligned} v(\xi) &= \frac{1}{2} e^{j\pi/4} \sqrt{\frac{\xi}{\pi}} \int_{\infty e^{-j2\pi/3}}^{\infty} \frac{w_2(\tau)}{w_2'(\tau)} e^{-j\xi\tau} d\tau \\ u(\xi) &= e^{j3\pi/4} \frac{\xi^{\frac{3}{2}}}{\sqrt{\pi}} \int_{\infty e^{-j2\pi/3}}^{\infty} \frac{w_2'(\tau)}{w_2(\tau)} e^{-j\xi\tau} d\tau \end{aligned} \qquad \text{(B-1)}$$

where $w_2(\tau)$ and its derivative $w_2'(\tau)$ denote Airy functions of the Second Kind. For small arguments ($\xi < 0.6$), the asymptotic expansion of (B-1) is given by

$$\begin{aligned} v(\xi) &\sim 1.0 - \frac{\sqrt{\pi}}{4}\xi^{\frac{3}{2}} + j\frac{7}{60}\xi^3 + \frac{7}{512}\sqrt{\pi} e^{-j\frac{\pi}{4}} \xi^{\frac{9}{2}} + \ldots \\ u(\xi) &\sim 1.0 - \frac{\sqrt{\pi}}{2} e^{-j\frac{\pi}{4}} \xi^{\frac{3}{2}} + j\frac{5}{12}\xi^3 + \frac{5}{64}\sqrt{\pi} e^{-j\frac{\pi}{4}} \xi^{\frac{9}{2}} + \ldots \end{aligned} \qquad \text{(B-2)}$$

while a rapidly converging residue series is used for $\xi > 0.6$

$$v(\xi) \sim = e^{-j\frac{\pi}{4}} \sqrt{\pi\xi} \sum_{n=1}^{10} \left(\tau_n'\right)^{-1} e^{-j\xi\tau_n'}$$

$$u(\xi) \sim = 2e^{j\frac{\pi}{4}}\sqrt{\pi}\xi^{\frac{3}{2}}\sum_{n=1}^{10}(\tau_n)^{-1}\,e^{-j\xi\tau_n} \qquad \text{(B-3)}$$

where τ_n and $\tau_n^{'}$ are zeros of $w_2(\tau)$ and $w_2^{'}(\tau)$, respectively. Those zeros are given in the following table

Table B-1
Zeros of the $w_2(\tau)$ and $w_2^{'}(\tau)$
$\tau_n = |\tau_n|e^{-j\frac{\pi}{3}}$ and $\tau_n^{'} = |\tau_n^{'}|e^{-j\frac{\pi}{3}}$

n	$\lvert\tau_n\rvert$	$\lvert\tau_n^{'}\rvert$
1	2.33811	1.011879
2	4.08795	3.24819
3	5.52056	4.82010
4	6.78661	6.16331
5	7.94413	7.37218
6	9.02265	8.48849
7	10.0402	9.53545
8	11.0085	10.5277
9	11.9300	11.4751
10	12.8288	12.3848

The far-zone Fock functions are given by

$$\begin{aligned} g^{(l)}(\xi) &= \frac{j^l}{\sqrt{\pi}}\int_\Gamma \frac{e^{j\xi\tau}}{w_1^{'}(\tau)}d\tau \\ f^{(l)}(\xi) &= \frac{j^l}{\sqrt{\pi}}\int_\Gamma \frac{e^{j\xi\tau}}{w_1(\tau)}d\tau \\ G^{(l)}(\xi) &= g^{(l)}(\xi)e^{j\frac{\xi^3}{3}} \\ F^{(l)}(\xi) &= f^{(l)}(\xi)e^{j\frac{\xi^3}{3}} \end{aligned} \qquad \text{(B-4)}$$

where $w_1(\tau)$ and its derivative $w_1^{'}(\tau)$ denote Airy functions of the First Kind and the integration contour is given by Logan [13]. These functions, $g^{(0)}(\xi)$, $g^{(1)}(\xi)$ and $f^{(0)}(\xi)$, may be calculated using

$$
\begin{aligned}
g^{(0)}(\xi) &= 2.0e^{-j\frac{\xi^3}{3}} \quad \xi < -1.3 \\
&= 1.39937 + \sum_{m=1}^{6} \frac{c(m)}{m!} (\kappa\xi)^m \quad -1.3 \leq \xi \leq 0.5 \\
&= \sum_{m=1}^{10} \frac{e^{\left[\kappa\alpha'(m)\xi\right]}}{\alpha'(m)Ai(m)} \quad 0.5 < \xi \leq 4.0 \\
&= 1.8325e^{\left[-(0.8823-j0.5094)\xi - j\frac{\xi^3}{3}\right]} \quad \xi \geq 4.0
\end{aligned} \tag{B-5}
$$

$$
\begin{aligned}
g^{(1)}(\xi) &= -j2.0\left(\xi^2 + j\frac{0.25}{\xi} - \frac{0.25}{\xi^4}\right) e^{-j\frac{\xi^3}{3}} \quad \xi < -2.8 \\
&= \sum_{m=1}^{6} \frac{c(m)\kappa^m}{m!} (\xi)^{m-1} \quad -2.8 \leq \xi \leq 0.5 \\
&= \kappa \sum_{m=1}^{10} \frac{e^{[\kappa\alpha(m)\xi]}}{Ai(m)} \quad 0.5 < \xi \leq 4.0 \\
&= -1.8325\left(0.8823 - j0.5094 + j\xi^2\right) e^{\left[-(0.8823-j0.5094)\xi - j\frac{\xi^3}{3}\right]} \quad \xi > 4.0
\end{aligned} \tag{B-6}
$$

$$
\begin{aligned}
f^{(0)}(\xi) &= j2\xi\left(1 - \frac{0.25}{\xi^3} + \frac{0.5}{\xi^6}\right) e^{-j\frac{\xi^3}{3}} \quad \xi < -1.1 \\
&= 0.77582 + e^{-j\pi/3} \sum_{m=1}^{6} \frac{c(m)}{m!} (\kappa\xi)^m \quad -1.1 \leq \xi \leq 0.5 \\
&= e^{-j\pi/3} \sum_{m=1}^{10} \frac{e^{[\kappa\alpha(m)\xi]}}{Ai'(m)} \quad 0.5 < \xi \leq 4.0 \\
&= 0.0 \quad \xi > 4.0
\end{aligned} \tag{B-7}
$$

with constant $\kappa = e^{-j5\pi/6}$ and the coefficients for (B–5) and (B–6) given in the following table

Table B-2 Constants for (B–5) and (B–6)			
m	c(m)	$\alpha'(m)$	Ai(m)
1	0.7473831	1.01879297	0.5356566
2	-0.6862081	3.2481975	-0.41901548
3	-2.9495325	4.82009921	0.38040647
4	-3.4827075	6.16330736	-0.35790794
5	8.9378967	7.37217726	0.34230124
6	56.1946214	8.48848673	-0.33047623
7		9.53544905	0.32102229
8		10.52766040	-0.31318539
9		11.47505663	0.30651729
10		12.38478837	-0.30073083

The corresponding constants for (B–7) are given as

Table B-3 Constants for (B–7)			
m	c(m)	$\alpha(m)$	Ai'(m)
1	1.146730417	2.33810741	0.70121082
2	0.86284558	4.08794944	-0.80311137
3	-2.0192636	5.52055983	0.86520403
4	-9.977776	6.78670809	-0.91085074
5	-14.59904	7.94413359	0.94733571
6	49.0751	9.02265085	-0.97792281
7		10.04017434	1.00437012
8		11.00852430	-1.02773869
9		11.93601556	1.04872065
10		12.82877675	-1.06779386

Radiation by Cavity-backed Antennas on a Circular Cylinder

Leo C. Kempel, John L. Volakis and Randy Sliva
Radiation Laboratory
University of Michigan
1301 Beal Ave.
Ann Arbor, MI 48109-2122

December 10, 1993

Abstract

Conformal antenna arrays are popular antennas for aircraft, spacecraft and land vehicle platforms due to their inherent low weight, cost and drag properties. However, to date there has been a dearth of rigorous analytical or numerical solutions to aid the designer. In fact, it has been common practice to use limited measurements and planar approximations in designing such non-planar antennas. In this paper, we extend the finite element-boundary integral method to radiation by cavity-backed structures in an infinite, metallic cylinder. The formulation is used to investigate the effect of cavity size on the radiation pattern for typical circumferentially and axially polarized patch antennas. Curvature effect on the gain, pattern shape and input impedance is also studied. Finally, the accuracy of the FE-BI approach for a microstrip patch array is demonstrated.

1 Introduction

Modern aircraft and missile deigns seek to utilize conformal antenna arrays rather than conventional protruding antennas due to their low weight, low drag, low cost and flexibility. Although most useful aircraft surfaces possess some curvature, the vast majority of available design information is restricted to planar elements. Indeed, the literature is rich with approximate [1], numerical [2] and experimental [3] design and characterization data for planar structures. The most common antenna element is a microstrip patch printed on a dielectric coated groundplane. Dielectric coated cylinders have also been investigated using approximate [4] and numerical [5] approaches.

Often, it is desirable to enclose each radiating element within a metallic cavity to suppress parasitic substrate coupling [6]. Approximate models, such as the cavity model, are typically not modified to account for the metallic sidewalls of the surrounding cavity since the approximations involved in this approach limits its operation to resonant patches. Experience has shown that a surrounding cavity does not effect the radiation pattern of a resonant patch antenna. However, since integral equation formulations are meant to operate at any frequency, these formulations need be modified to account for the metallic sidewalls. This is done by partitioning the problem into an interior cavity region and an open exterior region and enforcing field continuity across the aperture. Such an approach requires a complicated dyadic Green's function for the interior region and as is the case with all integral equation formulations, the resulting linear system is associated with a fully populated matrix and hence imposes a large $\mathcal{O}(N^2)$ memory and computation demand. Additionally, most integral equation formulations utilize equivalent surface currents and are therefore inappropriate for modeling inhomogeneous substrates.

An alternative formulation, utilizing the Finite Element-Boundary Integral (FE-BI) method, was proposed by Jin and Volakis [7] which was suitable for cavity-backed antennas recessed in a metallic groundplane. As with all partial differential equation formulations, this approach is associated with a highly sparse system which requires only $\mathcal{O}(N)$ storage. Additionally, when coupled with a Biconjugate Gradient-Fast Fourier Transform (BiCG-FFT) solver, the computational burden is only $\mathcal{O}(N\log(N))$. Since this approach is a volume formulation, inhomogeneous substrates may be readily modeled. This FE-BI method has been successfully used for scattering and antenna

performance analysis in planar platforms.

Recently, the FE-BI method was extended to cylindrical-rectangular and wraparound cavities for scattering calculations [8]. New divergence free, high fidelity edge-based elements were presented along with an efficient solution strategy which exploited an asymptotic evaluation of the appropriate dyadic Green's function as well as the BiCG-FFT solver. The resulting computer code was shown to accurately compute the scattering by planar and highly curved elements. This paper investigates the accuracy of this FE-BI method formulation for antenna performance analysis. Both radiation pattern and input impedance calculations will be compared with known results. The effect of curvature on the pattern shape, the resonance behavior and the input impedance will be explored.

2 Formulation

In this section, the FE-BI formulation appropriate for radiation analysis is developed for cavity-backed antennas recessed in an infinite metallic cylinder (see figure 1). As usual, the finite element formulation permits substantial modeling flexibility, including cavity inhomogeneities, lumped loads and microstrip feeding lines.

The FE-BI formulation begins with the weak form of the vector wave equation followed by specification of appropriate vector shape functions and dyadic Green's function. The resulting FE-BI equations are then used to solve for the total electric fields within the cavity and on the aperture (see for example Volakis *et al.* [9]). For the specific configuration at hand, the weak form of the wave equation can be written as

$$\int_{V_i} \left\{ \frac{\nabla \times \vec{W}_j(\rho,\phi,z) \cdot \nabla \times \vec{W}_i(\rho,\phi,z)}{\mu_r(\rho,\phi,z)} \right.$$
$$\left. -k_o^2 \epsilon_r(\rho,\phi,z) \vec{W}_j(\rho,\phi,z) \cdot \vec{W}_i(\rho,\phi,z) \right\} \rho \, d\rho \, d\phi \, dz$$
$$+(k_o a)^2 \delta_a(j) \delta_a(i) \int_{S_i} \int_{S_j} \left[\vec{W}_i(a,\phi,z) \cdot \hat{\rho}(a,\phi,z) \times \right.$$
$$\left. \overline{\overline{G}}_2(a,\bar{\phi},\bar{z}) \times \hat{\rho}(a,\phi',z') \cdot \vec{W}_j(a,\phi',z') \right] d\phi' \, dz' \, d\phi \, dz = f_i^{int} + f_i^{ext} \quad (1)$$

In this, $\vec{W}_i$ are vector basis functions with support over the volume V_i which is

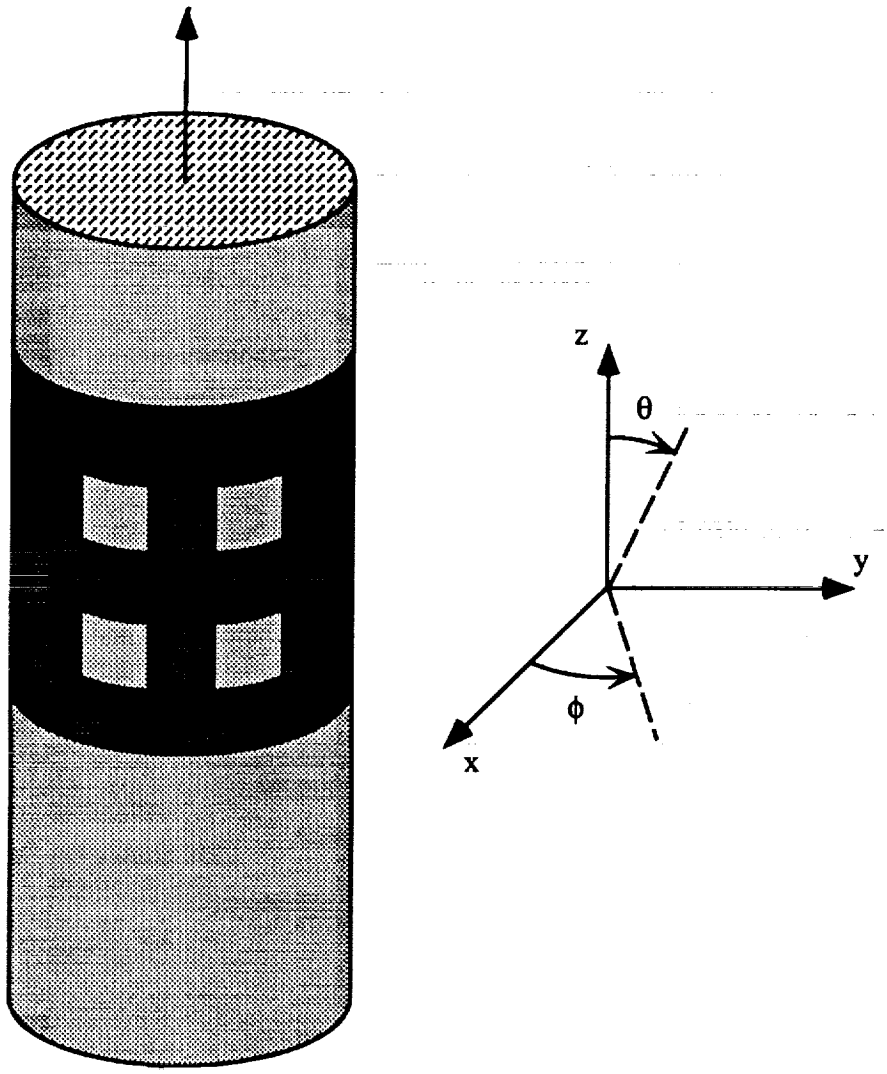

Figure 1: Illustration of a typical cavity-backed antenna situated on a metallic cylinder and the associated coordinate system.

associated with the i^{th} degree of freedom, and in a similar fashion, S_i and S_j represent aperture surfaces associated with the i^{th} and j^{th} degrees of freedom, respectively. The appropriate dyadic Green's function is denoted by $\overline{\overline{G}}_2$ and it has convolutional ($\bar{\phi} = \phi - \phi'$, $\bar{z} = z - z'$) form when evaluated on the surface of the cylinder, $\rho = a$. The unprimed coordinates represent the test point while the primed ones denote the source point. The free-space propagation constant is given by $k_0 = \frac{2\pi}{\lambda_0}$, where λ_0 is the free-space wavelength. The cavity is filled with an inhomogeneous material having relative constitutive properties ϵ_r and μ_r. The function $\delta_a(i)\delta_a(j)$ is the product of two Kronecker delta functions. Hence, it identifies which pairs of unknowns belong to the aperture and accordingly contribute to the boundary integral sub-matrix.

The FEM-BI equation (1) may be rewritten in matrix form as

$$\left[\mathcal{A}\right] \begin{Bmatrix} E_j^{ap} \\ E_j^{int} \end{Bmatrix} + \begin{bmatrix} [\mathcal{G}] & [0] \\ [0] & [0] \end{bmatrix} \begin{Bmatrix} E_j^{ap} \\ E_j^{int} \end{Bmatrix} = \begin{matrix} \{0\} \\ \{f_i^{int}\} \end{matrix} \tag{2}$$

where the entries of $[\mathcal{A}]$ are due to the FEM portion of the formulation and $[\mathcal{G}]$ is the boundary integral sub-matrix. In (2), E_j^{ap} and E_j^{int} denote degrees of freedom associated with the aperture and interior fields, respectively. In this, f_i^{int} are functions of the internal excitation and for this paper a radially oriented probe feed is considered.

The matrix entries, $[\mathcal{A}]$ and $[\mathcal{G}]$, are given in a previous paper [8]. In addition, the vector elements, dyadic Green's function evaluation and far-zone field formulae are given and are therefore not repeated here. Hence, we need only specify the interior source functional in order to model a radiating element. That functional is given for general impressed sources as

$$f_i^{int} = -\int_{V_i} \left\{ \nabla \times \left[\frac{\vec{M}^{int}(\rho,\phi,z)}{\mu_r(\rho,\phi,z)} \right] + jk_o Z_o \vec{J}^{int}(\rho,\phi,z) \right\} \cdot \vec{W}_i(\rho,\phi,z)\rho\, d\rho\, d\phi\, dz \tag{3}$$

where $\vec{J}^{int}$ and $\vec{M}^{int}$ are the impressed electric or magnetic current densities representing the sources. For a radially ($\hat{\rho}$) directed probe feed, the impressed monopole current located at (ϕ_s, z_s) is given by

$$\vec{J}^{int} = \hat{\rho} I_0 \frac{\delta(\phi - \phi_s)(z - z_s)}{\rho} \tag{4}$$

which results in an excitation function (3)

$$f_i^{int} = -jk_oZ_oI_o\frac{\tilde{s}_i\rho_b}{\alpha_i h_i}\ln\left(\frac{\rho_b}{\rho_a}\right)\left[\left(\phi_s-\tilde{\phi}_i\right)\left(z_s-\tilde{z}_i\right)\right] \quad (5)$$

if the edge-based elements of [8] are used.

Having specified the finite element and boundary integral matrices as well as the internal excitation for those systems, we use the BiCG method to solve for the unknown electric fields throughout the computation domain. The FE matrix is highly sparse and hence may be efficiently solved using a sparse matrix-vector product. It is also important to note that the matrix-vector product associated with the boundary integral can be performed using FFTs. Hence, the resulting BiCG-FFT solver is highly efficient without consuming excessive memory resources. The electric field may now be used to compute antenna parameters such as the gain and the input impedance.

The radiation pattern is computed by integrating the aperture fields with the far-zone dyadic Green's function given in [8]

$$\begin{aligned}\vec{H}^r(r,\theta,\phi) &= jY_ok_oa\int_S \overline{\overline{G}}_2(r,\theta,\phi;a,\phi',z')\cdot \\ &\quad \left[\hat{\rho}(a,\phi',z')\times\vec{E}(a,\phi',z')\right]d\phi'\,dz'\end{aligned} \quad (6)$$

with (r,θ,ϕ) indicating the observation point in spherical coordinates. In the far-zone, the electric and magnetic fields are related by

$$\begin{aligned}E_\phi^r &= -Z_oH_\theta^r \\ E_\theta^r &= Z_oH_\phi^r\end{aligned} \quad (7)$$

which is used to compute the antenna gain

$$G_{dB}(\theta,\phi) = 10\log_{10}\left[4\pi\left(\frac{r}{\lambda_{cm}}\right)^2|E^r(\theta,\phi)|^2\right]+10\log_{10}\left[\frac{\lambda_{cm}^2}{Z_oR_{in}}\right] \quad (8)$$

where λ_{cm} is the wavelength in centimeters, R_{in} is the input resistance which is given below and E^r is the radiated electric field as $r\rightarrow\infty$.

In addition to the antenna gain, designers are concerned with the input impedance of an antenna for feedline matching purposes. The FEM approach allows the calculation of the input impedance of the radiating structure in a

rather elegant manner. The input impedance is comprised of two contributions [10]

$$Z_{in} = Z_P + Z_D \tag{9}$$

where the first term is the probe's self-impedance (e.g. the probe's impedance in the absence of the patch) and the second term is the contribution of the patch current to the total input impedance. The probe self-impedance accounts for the finite radius of the probe and hence is omitted when a zero-thickness probe is assumed. Ignoring the probe-feed's self impedance, we have [10]

$$Z_{in}^{i} = -\frac{1}{I_o^2}\int_{V_i} \vec{E}(\rho,\phi,z)\cdot\vec{J}_i^{int}(\rho,\phi,z)\rho d\rho d\phi dz \tag{10}$$

where the impressed current is given by (4), V_i refers to the volume elements containing the probe-feed, the electric field is the interior field at (ρ,ϕ,z) and I_o is the constant current impressed on the probe. Utilizing (4) and assuming the edge-based elements presented in [8], the input impedance (10) is evaluated as

$$Z_{in}^{i} = -\frac{E(i)}{I_o}\frac{\tilde{s}_i\rho_b^i}{\alpha_i h_i}\ln\left(\frac{\rho_b}{\rho_a}\right)\left[\left(\phi_s-\tilde{\phi}_i\right)\left(z_s-\tilde{z}_i\right)\right] \tag{11}$$

which must be summed over the four radial edges of the element which contains the feed. Having specified the FE-BI system, interior excitation functional and appropriate antenna parameters such as gain and input impedance, the formulation may be used to analyze the radiation characteristics of several interesting configurations.

3 Results

The FE-BI formulation presented in [8] may be used for antenna performance studies by making the modifications outlined in this paper. This method can be used to determine the role of curvature in the radiation pattern and the input impedance of a cavity-backed patch antenna. Additionally, designers are concerned with the effect of the cavity size might have on antenna performance. In particular, since the cavity is used to suppress parasitic substrate

modes, varying the cavity size can be used to determine the effect of such modes on the radiation pattern.

Two types of antenna elements are investigated and they are shown in figure 2 where each patch is $a\alpha^o \times b$ in size with a denoting the radius of the cylinder. A patch whose radiating side walls are axially oriented is termed an axially polarized patch and is fed at $\phi_s = \frac{\alpha}{2}$. Circumferentially (or azimuthally) polarized patches have radiating walls forming constant z-surfaces and are typically fed at $z_s = \frac{b}{2}$. Observation in the $\theta = 90^o$ plane is the E-plane for circumferentially polarized patched and the H-plane for axially polarized elements. The terminology originates with the cavity model for patch antennas. We will now characterize a typical cavity-backed patch antenna.

Several computed and measured antenna patterns have been published for patches printed on a coated cylinder. One such patch, which is 3.5 cm × 3.5 cm, was used by Sohtell [11] to compare the accuracy of the cavity model [4] to a surface current integral equation [5]. The measured data was taken at 2.615 GHz for a metallic cylinder which was 63.5 cm long and had a radius of a = 14.95 cm. The cylinder was coated with a 0.3175 cm uniform dielectric having relative permittivity of $\epsilon_r = 2.32$. Data was taken for $-180^o \leq \phi \leq 180^o$ in the $\theta = 90^o$ plane corresponding to the E-plane for circumferentially polarized elements and the H-plane for axially polarized ones. Figure 3 compares these measured patterns with data generated using the FE-BI formulation for an identical patch placed within a $360^o \times 7$ cm cavity. This wraparound cavity best simulated the measured coated cavity. Note that the H-plane patterns are symmetric due to the symmetric placement of the feed, whereas the E-plane patterns are not symmetric. The placement of the feed was not specified in [11]; however, the agreement for the E-plane pattern shown in figure 3 indicates that the position used in the FE-BI model ($a\phi_s$ = -1 cm) is reasonable. The feed was placed at z_s = -1 cm for the axially polarized (H-plane) case.

In a previous paper [8], discrete cavity arrays were found to have a significantly lower radar cross section (RCS) compared to a wraparound array. Thus, the size of the cavity had a significant effect on the scattering properties of the array. The two antennas presented by Sohtell [11] were placed within cavities which were 7 cm high and approximately 30, 50, 90, 180, 270 or 360 degrees in angular extent. Figure 4 illustrates that azimuthal cavity size has little effect on the radiation pattern for a circumferentially polarized element. A similar comparison for the axially polarized patch is shown in

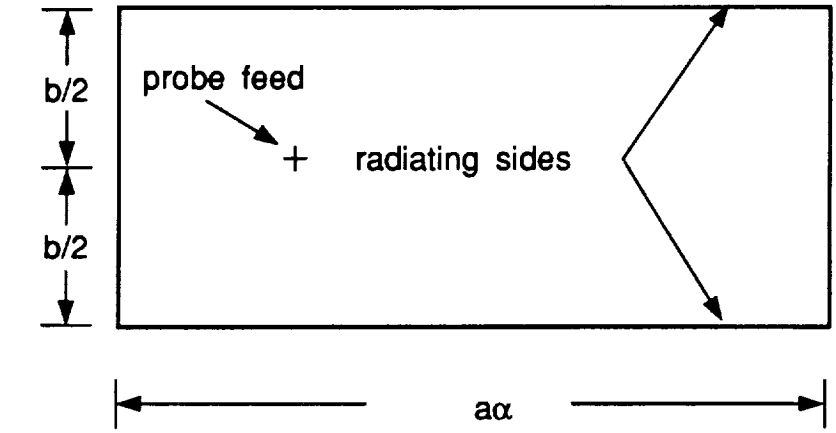

(a)

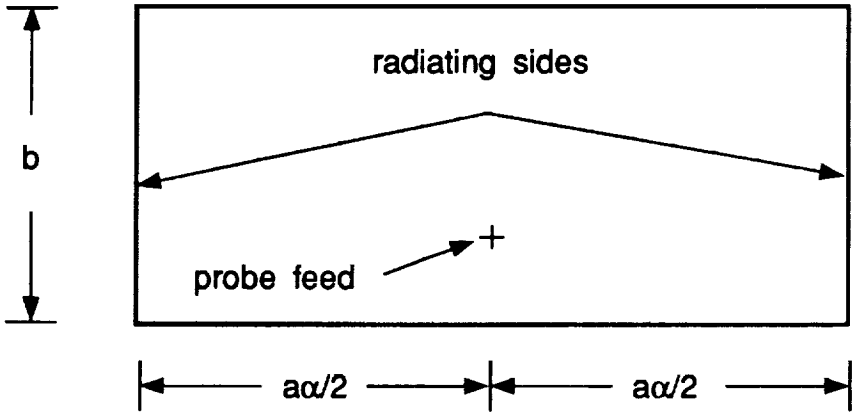

(b)

Figure 2: Illustration of (a) a circumferentially polarized patch element; and (b) an axially polarized patch element. The radius of the cylinder is denoted by a.

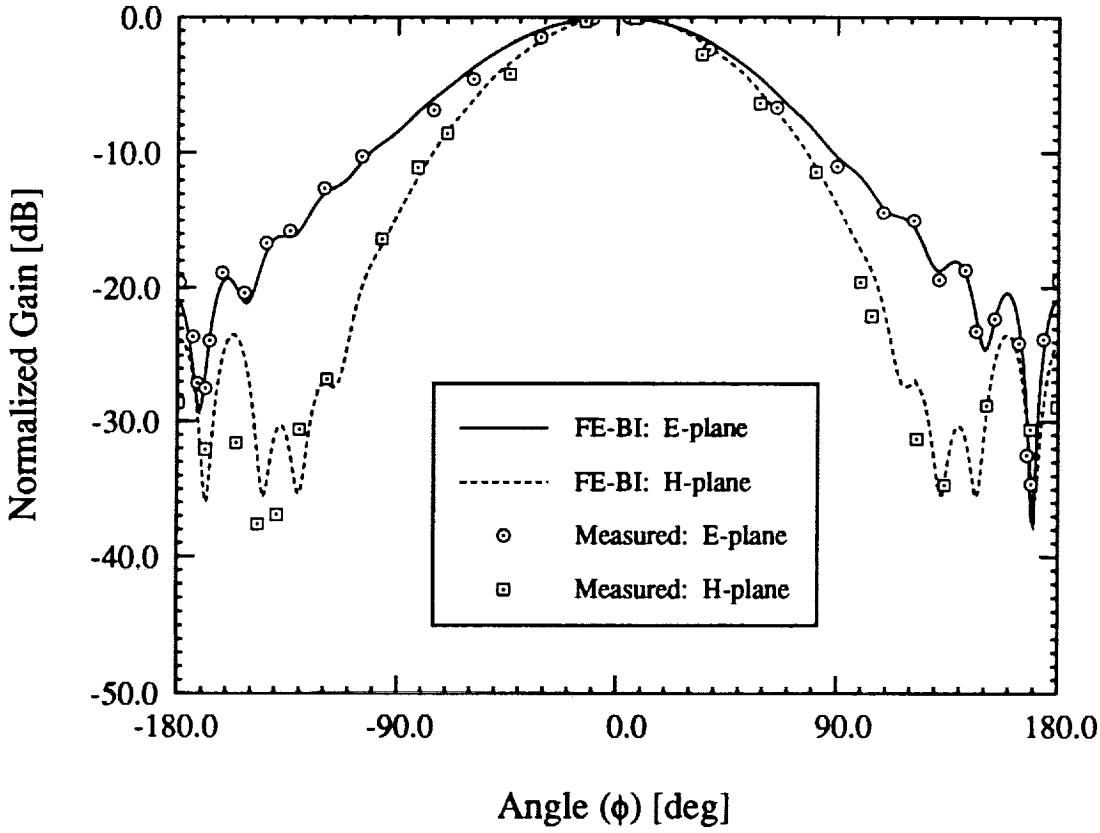

Figure 3: Comparison of measured [11] and computed data for a circumferentially polarized element (E-plane) and an axially polarized element (H-plane). The antenna (3.5 cm $\times$ 3.5 cm) was printed on a 14.95 cm cylinder with a 0.3175 cm coating (ϵ_r = 2.32). The probe feed was place at ($a\phi_s, z_s$) = (-1.0,0.0) for the circumferentially polarized patch and at ($a\phi_s, z_s$) = (0.0,-1.0) for the axially polarized antenna.

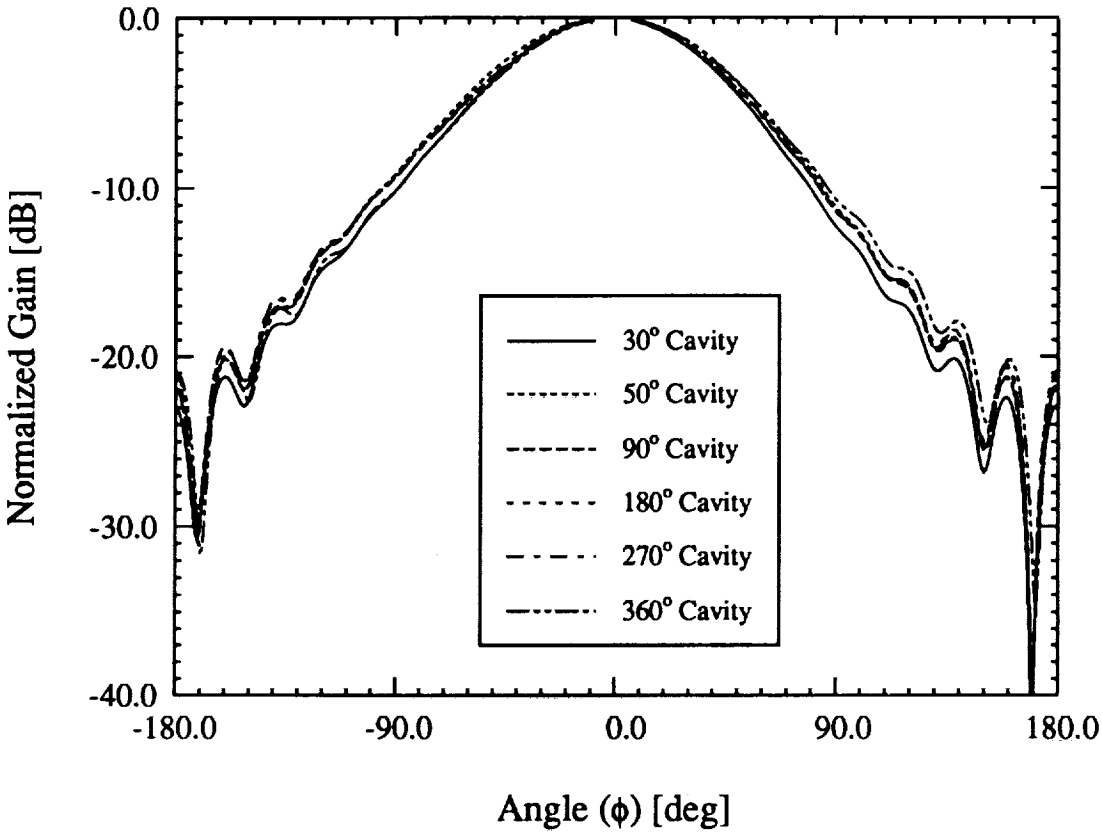

Figure 4: Effect of cavity size on the E-plane radiation pattern of a circumferentially polarized patch antenna.

figure 5. The back lobe of the antenna (near $\phi = 180^0$) is very small for cavities less than 180^o in extent but increases for larger cavities. For cavities which lie on the forward face of the cylinder, the substrate modes diffract off the cavity walls; an effect which has little influence on the main lobe of the pattern. However, for wraparound cavities and cavities which extend into the back side of the cylinder, the substrate modes shed like creeping waves giving rise to the back lobe.

Having established the effect of cavity size on the antenna patterns, it is instructive to gauge the effect that curvature has on the resonance behavior (or gain) of patch antennas. The two antennas were placed in 14 cm $\times$ 14 cm cavities which were place on cylinders with increasing radius. The frequency was allowed to vary from 2.4 GHz to 2.7 GHz and the peak radiated power was recorded at each frequency. For this paper, the radiated power is recognized as the first term of (8). Figure 6 illustrates that the resonance frequency increases with increasing curvature for a circumferentially polarized antenna, but the maximum gain is similar regardless of element curvature. Note in the cavity model, the radiating edges for a circumferentially polarized patch are the azimuthal walls of the cavity (see figure 2) which have a constant separation regardless of the cylinder radius. However, the axially polarized patch has decreasing resonant gain with increasing curvature as shown in figure 7. For this patch, radiation is attributed to the axial magnetic walls of the cavity model which have increasing angular separation with decreasing curvature. These walls radiate strongly away from the pattern peak ($\phi = 0^o$). Accordingly, the gain of an axially polarized antenna decreases with increasing curvature. The radiation pattern of a circumferentially polarized antenna is largely unaffected by curvature as shown in figure 8 when excited at a resonant frequency. However, the radiation pattern of the axially polarized antenna broadens as the curvature increases and this is illustrated in figure 9. Once again, both relationships are readily explained by considering the effect that curvature has on the orientation of the cavity model radiating walls.

In addition to the gain and pattern of an antenna, designers require the input impedance for matching purposes. For the antenna examined above (in a 14 cm $\times$ 14 cm cavity), the input impedance was calculated from 2.4 GHz to 2.7 GHz for various cylinder radii. Figure 10 illustrates that the input impedance of a circumferentially polarized patch antenna is not affected by curvature while figure 11 shows that increased curvature reduces the input

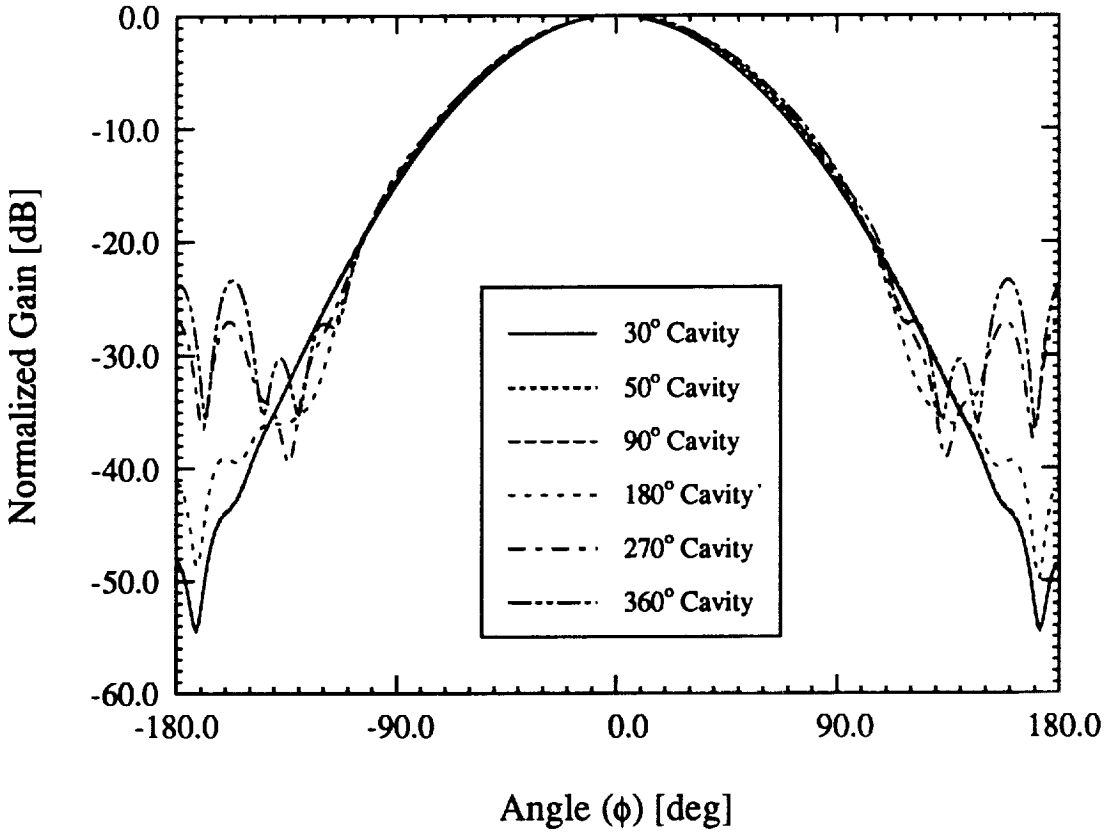

Figure 5: Effect of cavity size on the H-plane radiation pattern of an axially polarized patch antenna.

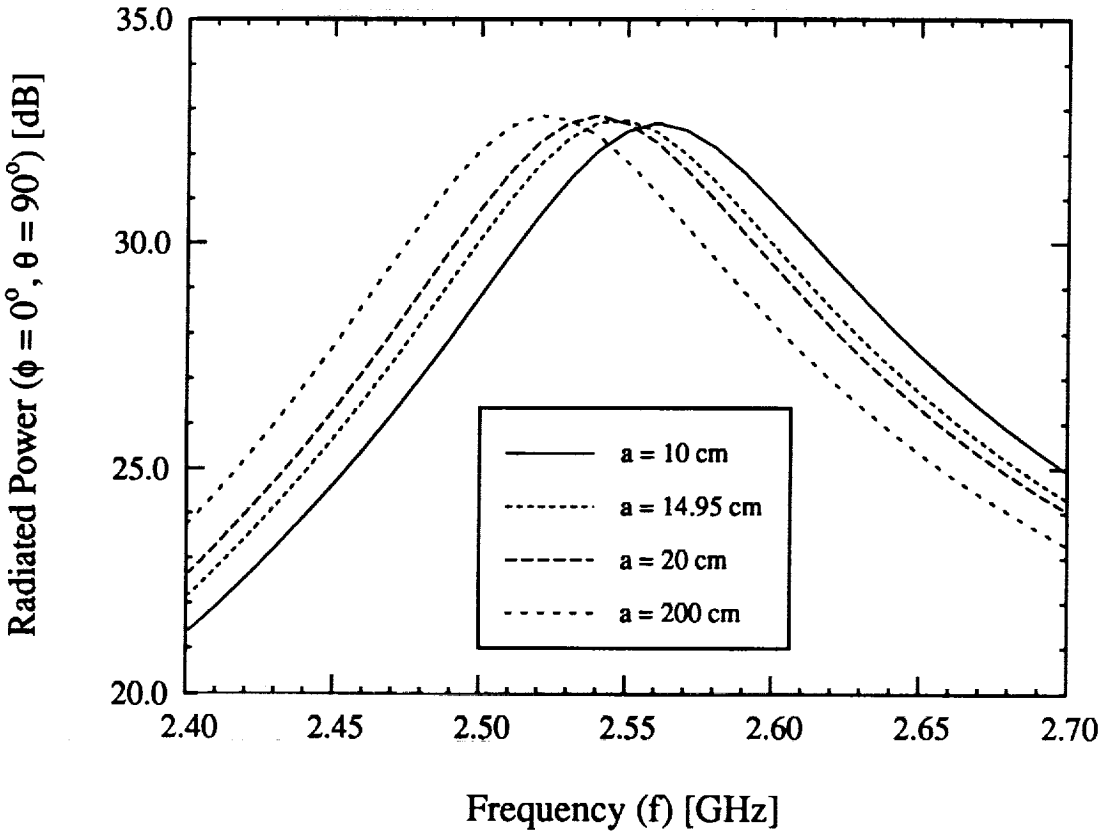

Figure 6: Resonance behavior of a circumferentially polarized patch antenna for various cylinder radii.

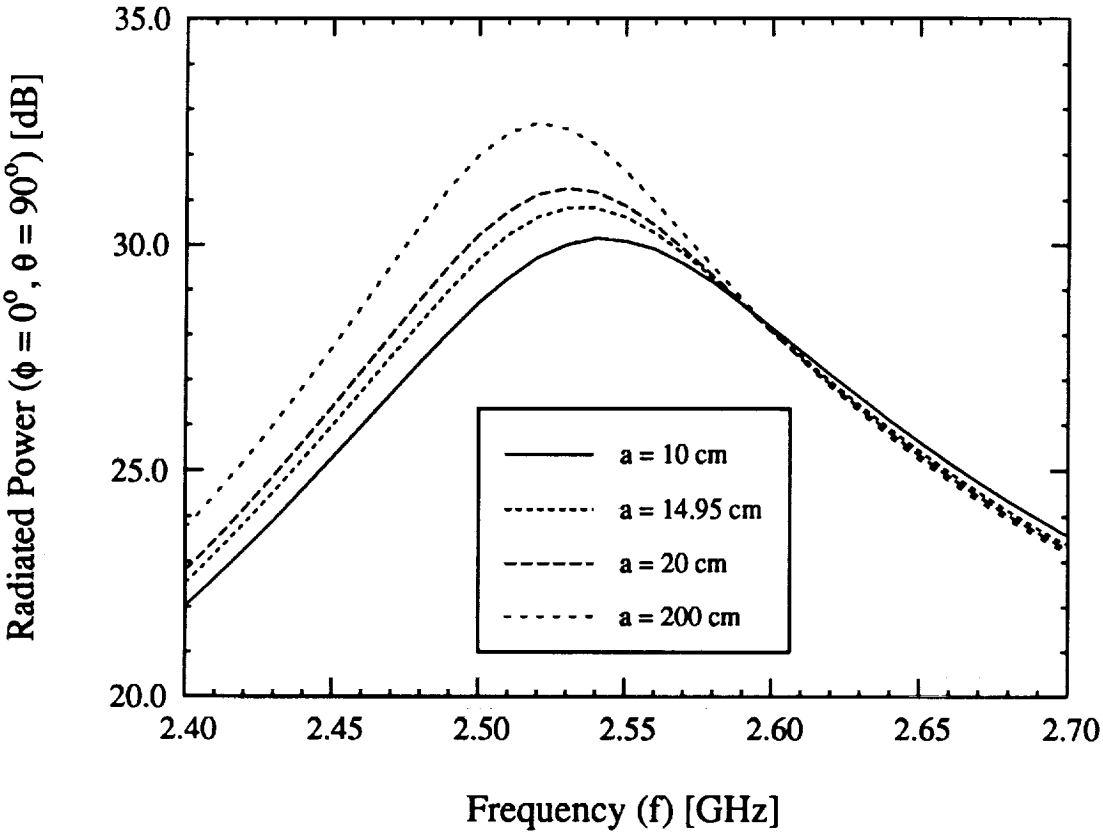

Figure 7: Resonance behavior of an axially polarized patch antenna for various cylinder radii.

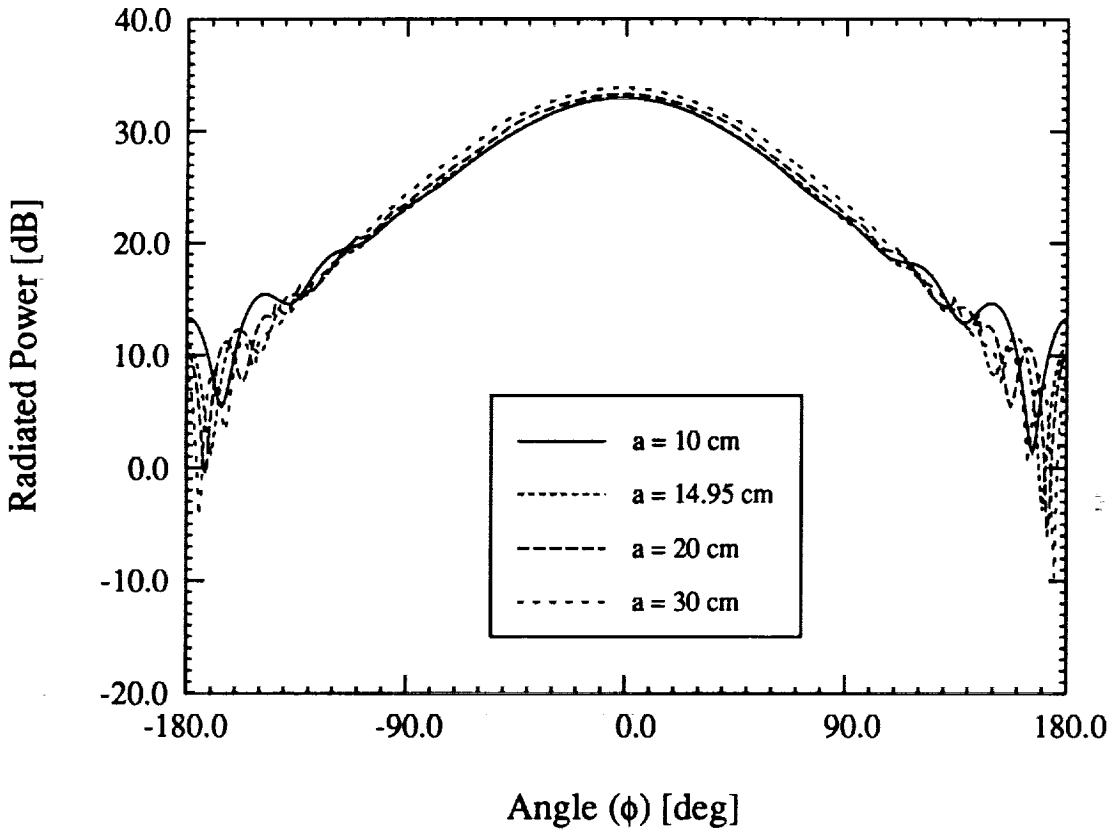

Figure 8: Variation of the radiation pattern shape with respect to curvature for a circumferentially polarized antenna.

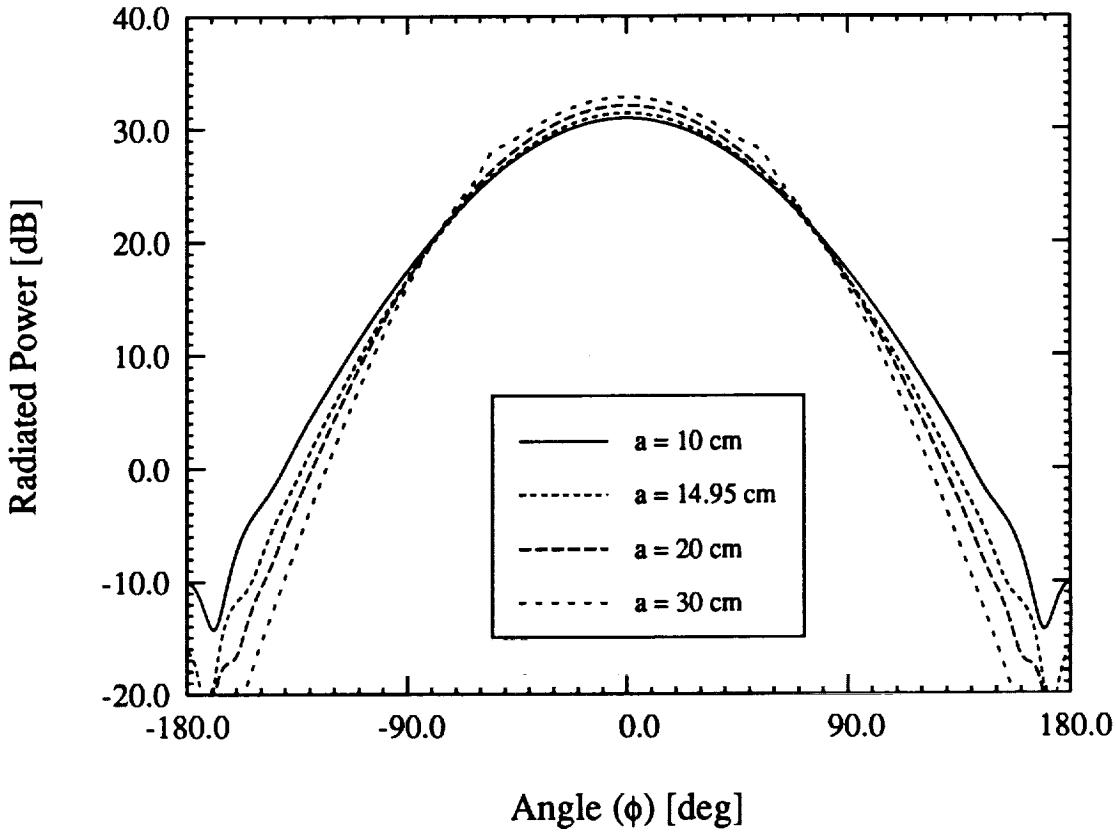

Figure 9: Variation of the radiation pattern shape with respect to curvature for an axially polarized antenna.

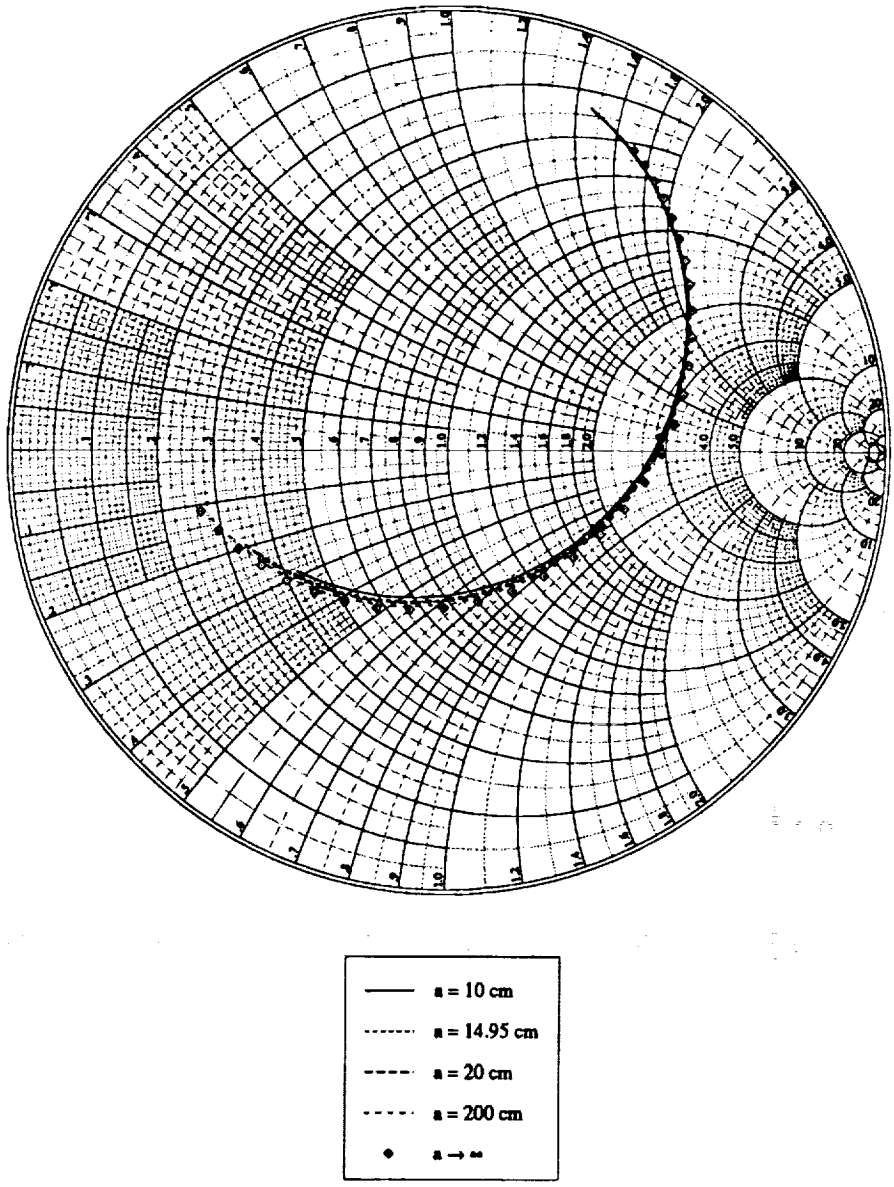

Figure 10: Input impedance of a circumferentially polarized patch antenna for various cylinder radii. The frequency range was 2.4 GHz to 2.7 GHz and the cavity size was 14 cm × 14 cm.

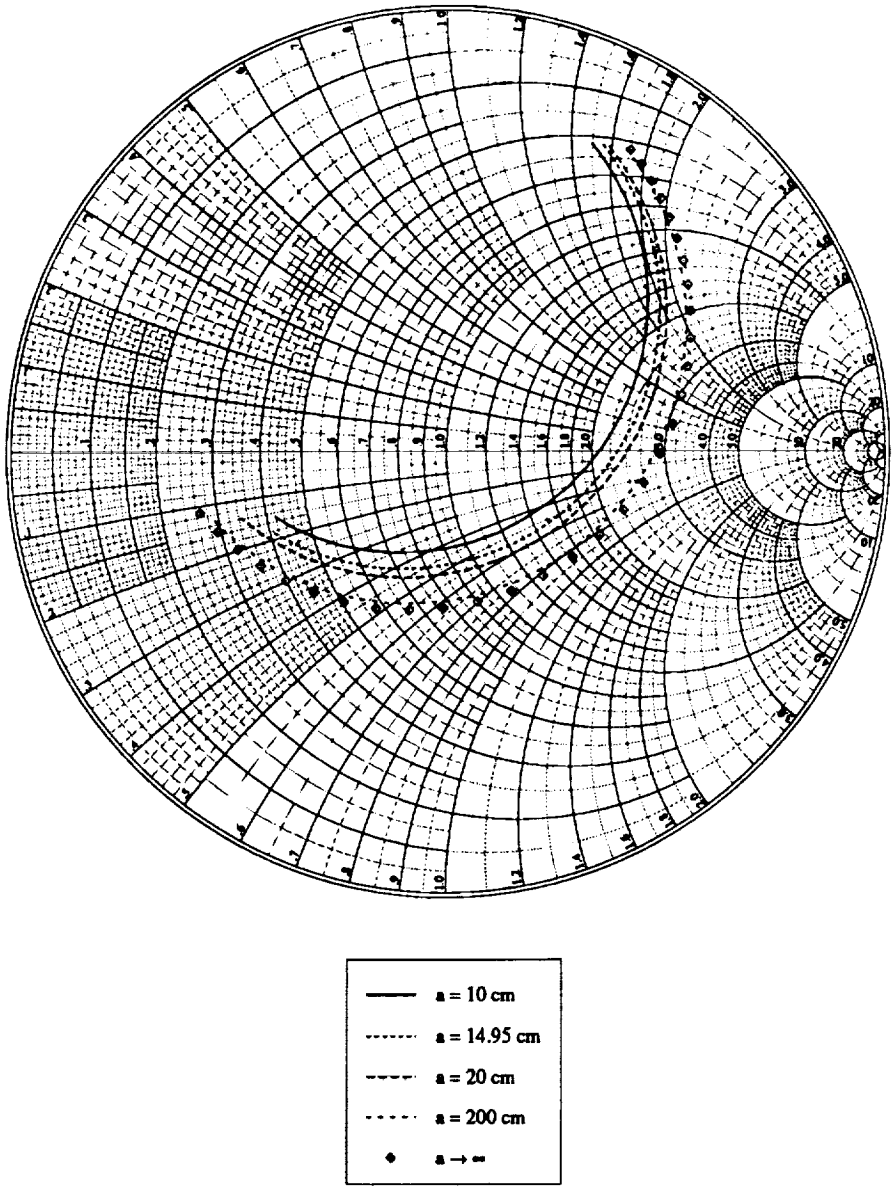

Figure 11: Input impedance of an axially polarized patch antenna for various cylinder radii. The frequency range was 2.4 GHz to 2.7 GHz and the cavity size was 14 cm $\times$ 14 cm.

impedance of an axially polarized patch. This observation agrees the the results reported by Luk *et. al.* [12].

In addition to single patches, the FE-BI formulation may be used to design microstrip arrays. Such an approach includes mutual coupling between elements which is ignored by the cavity model. Furthermore, the FE-BI formulation consumes less computational resources than a comparable integral equation formulation due to the sparsity of the FE matrix. The H-plane pattern of a four element array was measured to gauge the accuracy of the FE-BI approach. Each element is 2 cm $\times$ 3 cm and placed within a 5 cm $\times$ 6 cm $\times$ 0.07874 cm cavity which is filled with a dielectric having $\epsilon_r = 2.17$. The cylinder is 91.44 cm long and has a radius of 15.24 cm. The cavities are placed symmetrically around the cylinder (e.g. a patch is centered at 0°, 90°, 180° and 270°). Only the patch centered at 0° was excited while the remaining patches were terminated with a 50Ω load. The driving patch is axially polarized and the feed is located at $z_s = -0.375$ cm. Figure 12 illustrates the excellent agreement between the FE-BI formulation and the measured data.

4 Conclusions

In this paper, the FE-BI formulation for cavity-backed antennas was presented. The data generated by this code for a common cylindrical-rectangular patch antenna compared favorably with measured data. Having validated the implementation, the FE-BI method was used to study the radiation properties of a circumferentially and axially polarized patch antenna. The azimuthal cavity size was found to have little effect on the circumferentially polarized E-plane pattern. However, for the H-plane pattern of an axially polarized element, the back lobe is significantly larger for cavities which extend from the front side to the back side of the cylinder. A wraparound antenna exhibited the largest back lobe implying that this lobe is a result of creeping wave shedding. Diffraction due to the creeping wave is suppressed for cavities not extending to the back side of the cylinder. The presence of a back lobe must be considered when designing low observable, jam-resistant antennas or antennas on complex platforms (e.g. an antenna near the rear stabilizer). Thus, as was the case for scattering reduction, it is advisable to use the smallest cavity possible.

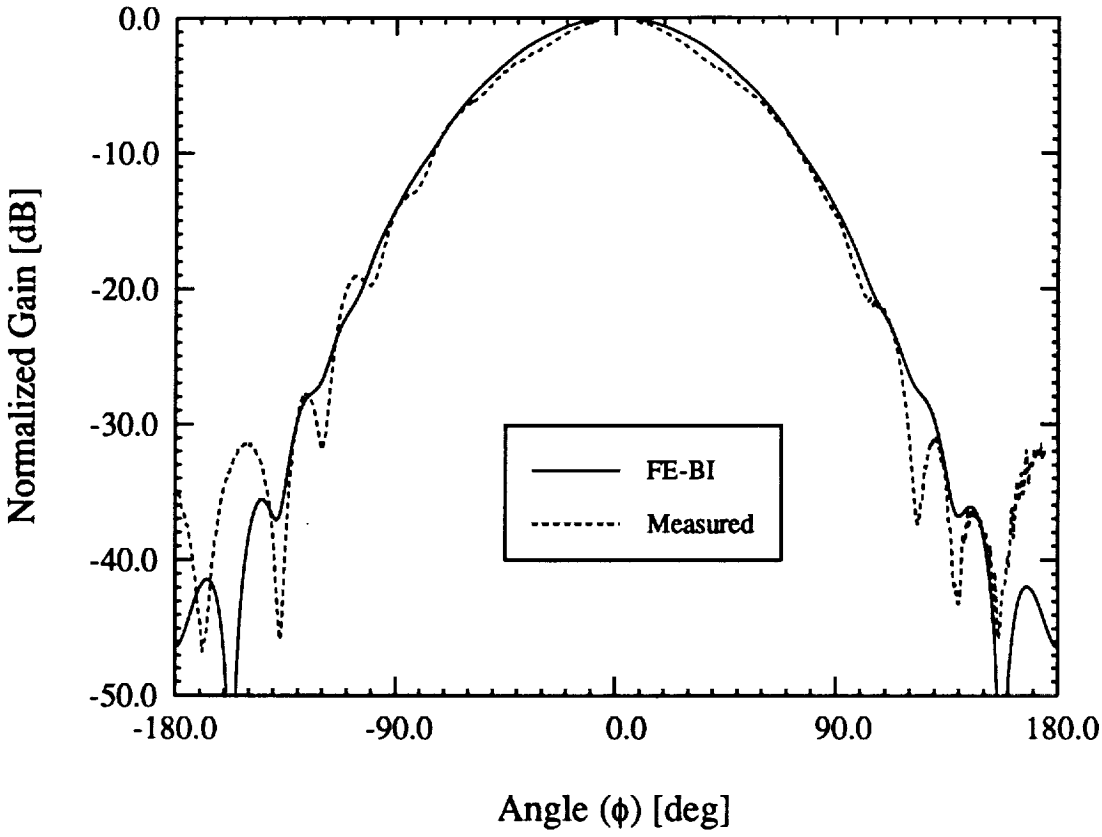

Figure 12: H-plane pattern for a four element patch array. Each patch is 2 cm $\times$ 3 cm and are placed symmetrically around the cylinder. Only the patch centered at 0^o is fed while the other patches are terminated with 50Ω loads.

The effect of curvature on the resonance, radiation pattern shape and input impedance was studied. Both circumferentially and axially polarized antennas were considered and was found that the resonant frequency increased with increasing curvature for both antennas. However, while the gain of the circumferentially polarized patch remained constant, the gain of the axially polarized patch decreased with increasing curvature. Such an effect is readily explained by considering which walls of the cavity model radiate for each polarization (see figure 2). The radiation pattern for axially polarized antennas broadens with increasing curvature while the corresponding patterns for circumferentially polarized antennas is unaffected by curvature. The input impedance of the circumferentially polarized antenna was not affected by curvature while the input impedance of the axially polarized antenna decreased with increasing curvature. We therefore conclude that axially polarized antennas are strongly affected by curvature while circumferentially polarized antennas are not affected by curvature.

Since the cavity model does not include mutual coupling and the usual integral equation formulations are associated with high storage and computational demand, the FE-BI formulation is attractive for array analysis. The H-plane pattern of a discrete four element wraparound array compared favorably with measured data.

References

[1] Y.T. Lo, D. Solomon and W.F. Richards, "Theory and experiments on microstrip antennas," *IEEE Trans. Antennas and Propagat.*, Vol. 27, pp. 137-145, 1979.

[2] D.M. Pozar and S.M. Voda, "A rigorous analysis of a microstripline fed patch antenna," *IEEE Antennas Propagat.*, Vol. 35, pp. 1343-1350, Dec. 1987.

[3] J.R. James and G.J. Wilson, "Microstrip antennas and arrays, Pt. 1 – Fundamental action and limitations," *IEE J. Microwaves, Optics, and Acoustics*, Vol. 1, pp. 165-174, 1977.

[4] J.S. Dahele, R.J. Mitchell, K.M. Luk and K.F. Lee, "Effect of curvature on characteristics of rectangular patch antenna," *Electronics Letters*, Vol 23, pp. 748-749, 2 July 1987.

[5] J. Ashkenazy, S. Shtrikman and D. Treves, "Electric surface current model for the analysis of microstrip antennas on cylindrical bodies," *IEEE Antennas Propagat.*, Vol. 33, pp. 295-300, Mar. 1985.

[6] J. Aberle, "On the use of metallized cavities backing microstrip antennas", *1991 IEEE Antennas and Propagat. Soc. Int. Symp.*, Vol. 1, pp.60-63, June 1991.

[7] J-M Jin and J.L. Volakis, "A hybrid finite element method for scattering and radiation by microstrip patch antennas and arrays residing in a cavity," *IEEE Trans. Antennas and Propagat.*, Vol. 39, No. 11, pp. 1598-1604, Nov. 1991.

[8] L.C. Kempel and J.L. Volakis, "Scattering by cavity-backed antennas on a circular cylinder," submitted to *IEEE Trans. Antennas and Propagat.*.

[9] J.L. Volakis, A. Chatterjee and J. Gong, "A class of hybrid finite element methods for electromagnetics: A review," to appear in *J. Electromagnetic Waves Appl.*, 1994.

[10] T.M. Hashaby, S.M. Ali and J.A. Kong, "Input impedance and radiation pattern of cylindrical-rectangular and wraparound microstrip antennas,"

IEEE Trans. Antennas and Propagat., Vol. 38, No. 5, pp. 722-731, May 1990.

[11] E.V. Sohtell, "Microstrip antennas on a cylindrical surface," in *Handbook of microstrip antennas*, Ed. J.R. James and P.S. Hall, Peregrinus: London, pp. 1227-1255, 1989.

[12] K-M Luk, K-F Lee and J.S. Dahele, "Analysis of the cylindrical-rectangular patch antenna," *IEEE Trans. Antennas and Propagat.*, Vol. 37, No. 2, pp. 143-147, Feb. 1989.

User Manual for EXCALIBUR: A FE-BI Numerical Laboratory for Cavity-Backed Antennas in a Circular Cylinder Version 1.2

Leo C. Kempel
Radiation Laboratory
University of Michigan
1301 Beal Ave.
Ann Arbor, MI 48109-2122

December 16, 1993

1 Introduction

The Finite Element-Boundary Integral (FE-BI) technique has been used to analyze the scattering and radiation properties of cavity-backed patch antennas recessed in a metallic groundplane. A program, CAVITY3D, was written and found to yield accurate results for large arrays without the usual high memory and computational demand associated with competing formulations. Recently, the FE-BI approach was extended to cavity-backed antennas recessed in an infinite, metallic circular cylinder. EXCALIBUR is a computer program written in the Radiation Laboratory of the University of Michigan which implements this formulation.

This user manual will give a brief introduction to EXCALIBUR and some hints as to its proper use. As with all computational electromagnetics programs (especially finite element programs), skilled use and best performance is only obtained through experience. However, we will comment on several important aspects of the program such as portability, geometry generation, interpretation of results and custom modification.

2 Formulation

EXCALIBUR implements the FE-BI formulation for cavity-backed antennas recessed in metallic circular cylinders. The formulation imposes some restrictions on the geometries which will be discussed. Principally, use of the BiConjugate Gradient-Fast Fourier Transform (BiCG-FFT) iterative solver requires uniform zoning on the aperture of the cavity. Thus, each surface patch has cylindrical-rectangular shape. The basis functions, dyadic Green's function and associated field formulas are given in a paper concerning scattering by these structures [1]. Modifications of this formulation for antenna analysis was given in another paper [2].

The uniform zoning requirement causes some difficulty in modeling; however, with some practice, these difficulties may be overcome. For example, the specification of the patch and cavity size must both be expressed by an integer number of edges (hence nodes). Thus, if the cavity is twice the size of the patch, one has no problem specifying the patch and the cavity with the same uniform grid. However, if the ratio of the patch and cavity sizes are not integers, discretization may not be possible. This is often the case with

a continuous wraparound cavity. Such a cavity is shown in figure 1 along with an example of a discrete wraparound array. If the cavity size and patch size are not convenient, you must either change the cavity size as possible or change the radius of the cylinder. If the radius is changed slightly, it will not effect the electromagnetic properties of the structure, but it may allow uniform discretization. Although the restrictions imposed by the uniform zoning requirement seems rather stringent, with practice, an antenna designer will find that EXCALIBUR is quite flexible.

3 Compilation

The first task in utilizing EXCALIBUR is to compile and link the various files of the program. The following files are required to run EXCALIBUR and are given on the distribution diskette: *excalibur.f*,*dyadic.f*, *matrixGenerate.f*, *preProcessor.f*, *rcs.f*, *fft.f*, *gauss.inc*, *fft.inc* and *excalibur.inc*. These files perform the following functions:

- *excalibur.f*: Main program, BiCG solver, matrix building subroutines, FE-BI subroutine, impedance insert and various auxiliary subroutines.
- *dyadic.f*: Compute dyadic Green's function terms for admittance matrix, on-surface and far-field Fock functions and gamma function.
- *matrixGenerate.f*: Boundary integral and FE matrix terms.
- *preProcessor.f*: Geometry/mesh generator.
- *rcs.f*: Radar Cross Section, far-zone dyadic Green's function and plane wave excitation functions.
- *fft.f*: Forward and inverse Fast Fourier Transform subroutines.
- *gauss.inc*: Numerical integration parameters for gaussian quadrature.
- *fft.inc*: Include file for 2-D FFT subroutines.
- *excalibur.inc*: Main memory allocation file also contains variable dictionary.

The distribution disk also contains the following Fast Fourier Transform options:

- *fftCooley.f*: Classic Cooley-Tukey Radix-2 algorithm.
- *fftSplitRadix.f*: Split-Radix algorithm by Sorenson [3].

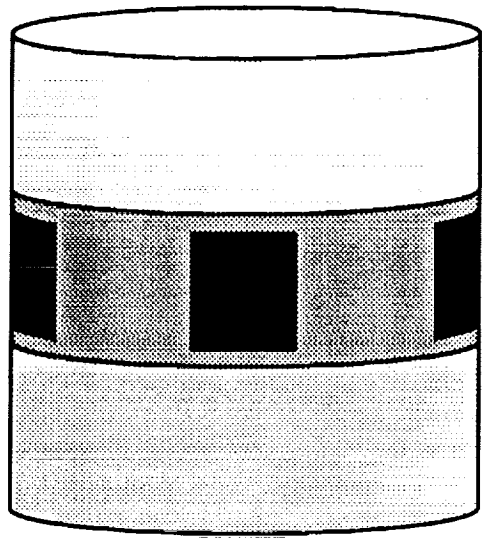

(a)

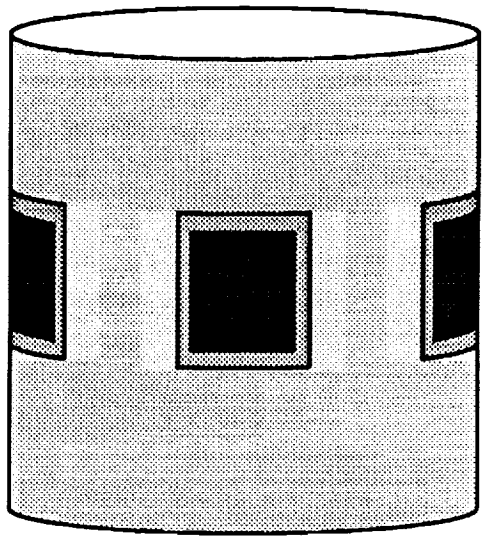

(b)

Figure 1: Illustration of two types of arrays: (a) wraparound array; (b) discrete cavity array

- fftCRAY.f: Calls the CRAY library vectorized, multitasked 2-D FFT routine.
- fftCONVEX.f: Calls the *veclib* vectorized 2-D FFT routine.

Prior to compilation, the user should copy one of these files into *fft.f*. The optimized routines for the CRAY and CONVEX architectures should be used when possible while in general the Split-Radix algorithm should give better performance than the Cooley-Tukey version. To enhance their efficiency, the Split-Radix and Cooley-Tukey files utilize a decimation-in-frequency forward transform and a decimation-in-time inverse transform in order to avoid the need to perform bit reversal.

Another file which is included on the distribution diskette is *convertToASCII.f*. To save disk space, the geometry information is stored in a binary format by *preprocessor*. The program *convertToASCII* is included to produce a human-readable file (ASCII). The nodes, elements, edges, unknowns and other useful information is provided in a easy to read (although disk space consuming) format. All the programs are compiled and linked by invoking the UNIX *make* utility. A *Makefile* has been provided on the distribution disk. To date, EXCALIBUR has been successfully compiled, linked and run on the following architectures/operating systems: SUN, DEC UNIX, HP 9000/7xx, IBM RS/6000, Silicon Graphics IRIS, CRAY and CONVEX. Three variable must be set within the *Makefile*:

- FF: The Fortran compiler name for the architecture.
- FOPT: The Fortran compiler options i.e. optimization, precision, etc.
- LOPT: The name of any libraries required for linking.

The user should uncomment these variables for the target architectures in *Makefile*. EXCALIBUR is constructed by simply typing *make* at the command line, while the binary-to-ASCII conversion program is constructed by entering *make convert*. EXCALIBUR is invoked by typing *excalibur* at the command line while the conversion program is run with the command *convertToASCII*. Finally, the directory may be cleaned up of all object and executable file by typing *make clean*.

4 Geometry Information

The binary geometry file created by *preprocessor* contains all the information concerning the physical structure under study except for the placement of any probe-feeds or lumped impedance posts. Therefore, it is important that the user be aware of the geometry entered into the FE-BI portion of the code. As previously mentions, the *convertToASCII* program creates a human-readable file from the machine-readable geometry file.

The first information provided in the resulting ASCII file is the header. which contains the number of nodes, number of edges, number of unknowns, etc. and an example of the header is shown in figure 2. The next field contains the node information. The information given is as follows (see figure 3):

- Column 1: Node number
- Column 2: Radial (ρ) coordinate in centimeters.
- Column 3: Angular (ϕ) coordinate in degrees.
- Column 3: Axial (z) coordinate in centimeters.
- Column 4: Layer number from top of the cylinder (aperture).
- Column 5: Row number from lowest axial coordinate.
- Column 6: Column number from smallest azimuthal coordinate.

Each node is associated with a physical location (ρ,ϕ,z) and a grid location (layer,row,column).

Grid points must be used in the discretization of a geometry since the BiCG-FFT solver requires that each node pair lie an integer number of units apart. Thus, the distance between two nodes (primed and unprimed) on the surface of the cylinder is given by

$$R(n,m;n',m') = \sqrt{(n-n')a\Delta\phi + (m-m')\Delta z} \qquad (1)$$

EXCALIBUR distinguishes between grid points and nodes. A grid point can be thought of as the intersection of two lines of a piece of graph paper which is placed on the surface of the cylinder. A node is a grid point which lies within a cavity. The row and column number associated with a node actually is the row and column number of the grid point which formed the node. The first grid point which corresponds to the lower-left corner of the grid has row

```
Binary filename:test.exc


ASCII filename:test.ascii


NODE statistics:

Total number of nodes:  50
Number of nodes on the surface:  25
Number of nodes along the metallic walls:  41
Number of nodes on surface metallic patches:  0
Number of nodes which are resistive:  0


EDGE statistics:

Total number of edges:  105
Interior edges:  9
Aperture edges:  24
         a) substrate edges:  24
         b) resistive edges:  0
Metal edges (NOT unknowns):  72

|||||||| UNKNOWNS ||||||||-->   33


ELEMENT statistics:

Total number of elements:  16
Surface Elements:  16
```

Figure 2: Geometry header.

Node	rho(cm)	phi(deg)	z(cm)	layer	row	column
1	1.00000	-5.00000	-0.50000	0	0	0
2	1.00000	-2.50000	-0.50000	0	0	1
3	1.00000	0.00000	-0.50000	0	0	2
4	1.00000	2.50000	-0.50000	0	0	3
5	1.00000	5.00000	-0.50000	0	0	4
6	1.00000	-5.00000	-0.25000	0	1	0
7	1.00000	-2.50000	-0.25000	0	1	1
8	1.00000	0.00000	-0.25000	0	1	2
9	1.00000	2.50000	-0.25000	0	1	3
10	1.00000	5.00000	-0.25000	0	1	4
11	1.00000	-5.00000	0.00000	0	2	0
12	1.00000	-2.50000	0.00000	0	2	1
13	1.00000	0.00000	0.00000	0	2	2
14	1.00000	2.50000	0.00000	0	2	3
15	1.00000	5.00000	0.00000	0	2	4
16	1.00000	-5.00000	0.25000	0	3	0
17	1.00000	-2.50000	0.25000	0	3	1
18	1.00000	0.00000	0.25000	0	3	2
19	1.00000	2.50000	0.25000	0	3	3
20	1.00000	5.00000	0.25000	0	3	4
21	1.00000	-5.00000	0.50000	0	4	0
22	1.00000	-2.50000	0.50000	0	4	1
23	1.00000	0.00000	0.50000	0	4	2
24	1.00000	2.50000	0.50000	0	4	3
25	1.00000	5.00000	0.50000	0	4	4
26	0.90000	-5.00000	-0.50000	1	0	0
27	0.90000	-2.50000	-0.50000	1	0	1
28	0.90000	0.00000	-0.50000	1	0	2
29	0.90000	2.50000	-0.50000	1	0	3
30	0.90000	5.00000	-0.50000	1	0	4

<< Remainder of nodes truncated >>

Figure 3: Node information.

= 0 and column = 0. For a wraparound grid, the first grid point is physically located at $\phi = -180^{o}$ and once again has row = 0 and column = 0.

The next set of information provided is the edges which form the cavities. The information given is as follows (see figure 4)

- Column 1: Edge number.
- Column 2: Left (lower) node forming the edge.
- Column 3: Right (upper) node forming edge.
- Column 3: Unknown number (zero indicates a fixed edge (e.g. metal)).
- Column 4: Orientation (ρ-, ϕ- or z-directed).
- Column 5: Type of edge (metal,substrate,resistive or interior).

Each edge is associated with two nodes and hence has an orientation in the cylindrical coordinate system. If an edge is metal, since EXCALIBUR uses a total field formulation, that edge's weight is fixed at zero. All other edges are unknowns which must be solved using the BiCG-FFT solver. A substrate or resistive edge is associated with the boundary integral while interior edges contribute only to the FE portion of the system. Currently, resistive cards are not implemented in EXCALIBUR.

The next set of information related the unknowns on the aperture of the cavities to their edge number. It also includes the row and column number of that edge in the discretization grid. Although this information is useful for understanding the mechanics of the BiCG-FFT solver, it is of little interest to the general user. The given information is (see figure 5)

- Column 1: Unknown number.
- Column 2: Associated edge number.
- Column 3: Row of this edge in the discretization.
- Column 3: Column of this edge in the discretization.

The edges which form each element of the mesh are given next. Each cylindrical shell element consists of eight nodes which form twelve edges. This information is useful in visualizing the mesh and could be hooked into a graphics package to generate a 3-D picture of the mesh. The prototype element is shown in figure 6 which displays the node numbering scheme. The information given by *convertToASCII* is (see figure 7)

- Row 1, Column 1: Element number.

Edge	Node 1	Node 2	Unknown	Orientation	Type
1	26	1	0	rho-directed	metal
2	27	2	0	rho-directed	metal
3	31	6	0	rho-directed	metal
4	32	7	25	rho-directed	interior
5	26	27	0	phi-directed	metal
6	1	2	0	phi-directed	metal
7	31	32	0	phi-directed	metal
8	6	7	1	phi-directed	substrate
9	26	31	0	z-directed	metal
10	1	6	0	z-directed	metal
11	27	32	0	z-directed	metal
12	2	7	13	z-directed	substrate
13	28	3	0	rho-directed	metal
14	33	8	26	rho-directed	interior
15	27	28	0	phi-directed	metal
16	2	3	0	phi-directed	metal
17	32	33	0	phi-directed	metal
18	7	8	2	phi-directed	substrate
19	28	33	0	z-directed	metal
20	3	8	14	z-directed	substrate
21	29	4	0	rho-directed	metal
22	34	9	27	rho-directed	interior
23	28	29	0	phi-directed	metal
24	3	4	0	phi-directed	metal
25	33	34	0	phi-directed	metal
26	8	9	3	phi-directed	substrate
27	29	34	0	z-directed	metal
28	4	9	15	z-directed	substrate
29	30	5	0	rho-directed	metal
30	35	10	0	rho-directed	metal

<< Remaining edges truncated >>

Figure 4: Edge information.

Unknown	Edge	Row	Column
1	8	2	1
2	18	2	3
3	26	2	5
4	34	2	7
5	40	4	1
6	47	4	3
7	52	4	5
8	57	4	7
9	63	6	1
10	70	6	3
11	75	6	5
12	80	6	7
13	12	1	2
14	20	1	4
15	28	1	6
16	44	3	2
17	49	3	4
18	54	3	6
19	67	5	2
20	72	5	4
21	77	5	6
22	90	7	2
23	95	7	4
24	100	7	6

Figure 5: Relationship between unknown number and edge number on aperture.

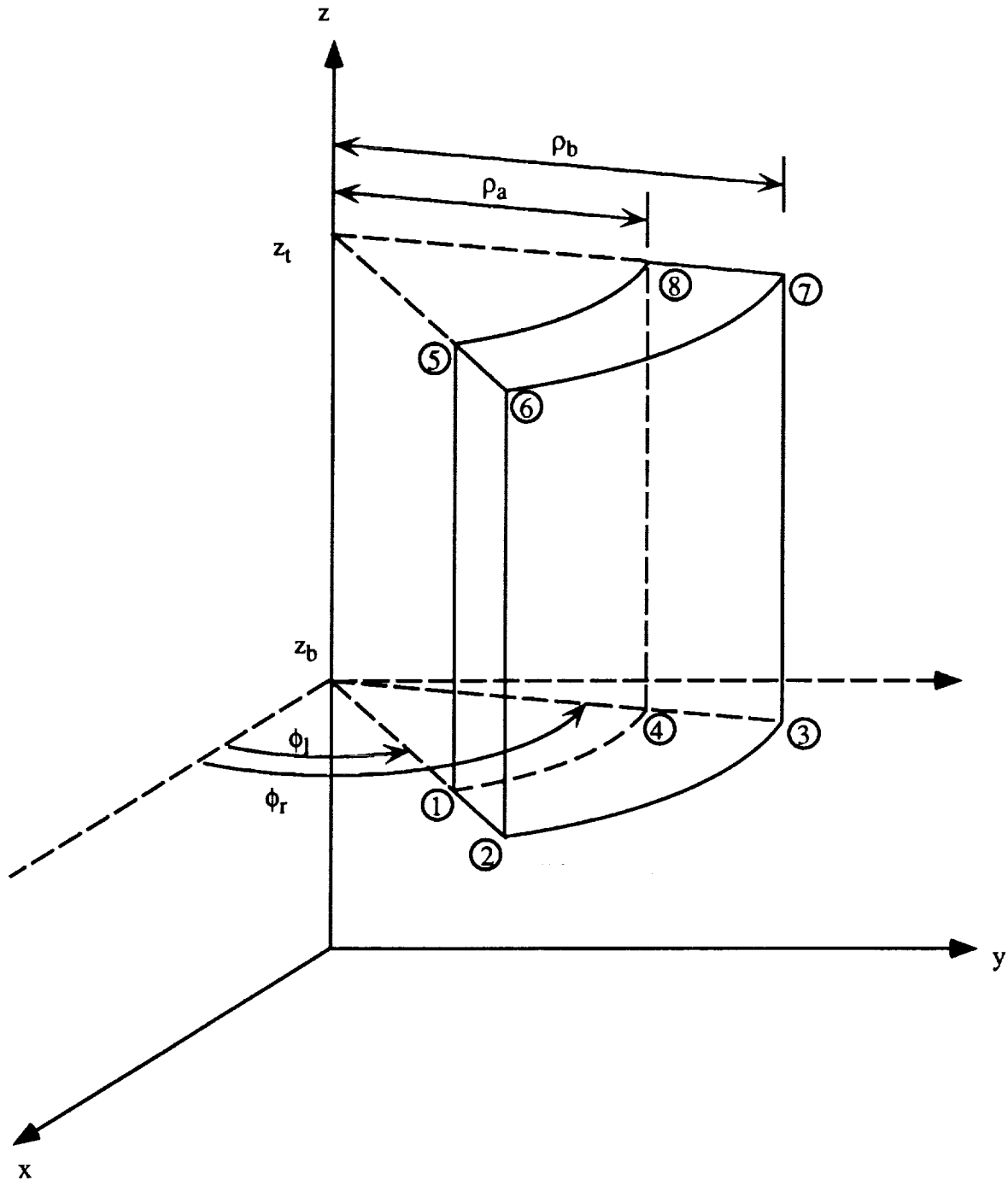

Figure 6: Cylindrical shell element.

- Row 1, Column 2-5: ρ-directed edges.
- Row 2, Column 2-5: ϕ-directed edges.
- Row 3, Column 2-5: z-directed edges.

The final set of information provided is the element parameters as shown in figure 6 which includes (see figure 8)

- Row 1: Element number.
- Row 2: ρ_a, ρ_b and t $= \rho_b - \rho_a$.
- Row 3: ϕ_l, ϕ_r and $\alpha = \phi_r - \phi_l$.
- Row 3: z_b, z_t and h $= z_t - z_b$.

5 Geometry Generation

Having reviewed the geometry information provided by *preprocessor* through *convertToASCII*, we are prepared to generate some example geometries. Specifically, we shall look at radiation and scattering by a 2 cm $\times$ 3 cm patch antenna which is placed in a 5 cm $\times$ 6 cm cavity, a four element discrete array of such cavities and the same radiating array placed in a continuous wraparound cavity. These three variations of the same geometry exhibit the main classes of structures encountered in practice. Users will find it very helpful to check the entered geometry via *convertToASCII* prior to running the solver part of EXCALIBUR. In particular, it is useful to discretize the cavity without patches present and retain the node information since it will be necessary to specify the row and column of the lower-left corner of each patch as well as the number of edges along each side.

EXCALIBUR has a *preprocessor* module which generates the required mesh. It first generates the surface nodes which are then used to create the 3-D mesh. An in-house modeling package, such as SDRC IDEAS, may be used to create such a surface grid so long as the nodes are an integer number of units apart. It would be quite easy to interface such a package with EXCALIBUR by replacing the subroutine *simpleMesh* with a universal file reader. However, we have found that the custom mesh routine provided with EXCALIBUR (*simpleMesh*) is sufficient for most modeling tasks while

Element	Edges			
1	1	2	3	4
	5	6	7	8
	9	10	11	12
2	2	13	4	14
	15	16	17	18
	11	12	19	20
3	13	21	14	22
	23	24	25	26
	19	20	27	28
4	21	29	22	30
	31	32	33	34
	27	28	35	36
5	3	4	37	38
	7	8	39	40
	41	42	43	44

<< Remaining elements truncated >>

Figure 7: Edges associated with each element.

```
Element size parameters:

  Element number:              1
     rhoA =     0.90000  rhoB =     1.00000    t =     0.10000
     phiL =    -5.00000  phiR =    -2.50000  alpha =     2.50000
      zB  =    -0.50000   zT  =    -0.25000    h   =     0.25000

  Element number:              2
     rhoA =     0.90000  rhoB =     1.00000    t =     0.10000
     phiL =    -2.50000  phiR =     0.00000  alpha =     2.50000
      zB  =    -0.50000   zT  =    -0.25000    h   =     0.25000

  Element number:              3
     rhoA =     0.90000  rhoB =     1.00000    t =     0.10000
     phiL =     0.00000  phiR =     2.50000  alpha =     2.50000
      zB  =    -0.50000   zT  =    -0.25000    h   =     0.25000

  Element number:              4
     rhoA =     0.90000  rhoB =     1.00000    t =     0.10000
     phiL =     2.50000  phiR =     5.00000  alpha =     2.50000
      zB  =    -0.50000   zT  =    -0.25000    h   =     0.25000

  Element number:              5
     rhoA =     0.90000  rhoB =     1.00000    t =     0.10000
     phiL =    -5.00000  phiR =    -2.50000  alpha =     2.50000
      zB  =    -0.25000   zT  =     0.00000    h   =     0.25000

                 << Remaining elements truncated >>
```

Figure 8: Element parameters.

being quite efficient. For this manual, we will use this package for all meshing requirements.

The first example is a 2 cm × 3 cm patch antenna recessed in a 5 cm × 6 cm cavity which is centered at ($\phi = 0°$, z = 0 cm). The required information is as follows

- Choose item 1 (Preprocessor) from main menu.
- Enter radius of the cylinder in centimeters.
- Enter angular and axial size of grid in degrees and centimeters.
- Enter center of grid in degrees and centimeters.
- Enter number of grid points in azimuthal and axial directions.
- Enter number of identical cavities in the azimuthal and axial directions.
- Enter number of nodes per cavity.
- Indicate whether all surface nodes are metallic or resistive.
- Indicate whether all surface nodes are on the substrate (0 means a patch is present).
- Enter number of patches.
- Enter row and column of lower-left hand node of the patch (see node section of the geometry file for this information).
- Enter number of edges in (ϕ,z) directions for this patch.
- Indicate any additional metallic nodes (-999 2 denotes no remaining nodes).
- Enter number of substrate layers.
- For each layer, enter its thickness in centimeters.
- Enter 1 to save this geometry.
- Enter filename for this geometry.

The transcript for this geometry is shown on the following pages. The next two examples are a discrete array of these elements and a continuous wraparound array. The main difference is that the number of grid points is not the same as the number of nodes on the cavity surface. Essentially, the same information is entered as above with the exception that these two arrays have a wraparound (360°) grid. See the attached transcripts for more details. Note for continuous wraparound cavities, if a patch crosses the branch cut ($\phi = \pm 180°$), the nodes along the lower edge of the patch must be

hand entered as shown in example 3. These nodes are obtained by running the *preprocessor* without specifying any patches and inspecting the human-readable geometry file. Note that for these three examples, the number of unknowns is dramatically different. For the single cavity of example 1, only 541 unknowns are required. The four identical discrete cavities requires 2164 unknowns which is of course 4×541. Finally, the continuous wraparound cavity has 12992 unknowns!

```
|||||||||||||||||||||||||||||||||||||||||
|                                       |
|              Example 1                |
|     Single Discrete Cavity Example    |
|                                       |
|||||||||||||||||||||||||||||||||||||||||

 Do you wish to run:
                    1) Preprocessor
                    2) FEM-BI
                    3) Impedance aperture
                    0) Exit
1

 Performing initialization, please wait....

 Enter radius of cylinder (cm):
15.27887
 Enter array size (phi,z) in (deg,cm):
18.75 6
 Enter center of array (phi,z) in (deg,cm):
0 0
 Enter number of grid points in (phi,z) direction:
11 25

 Discretization:
                deltaPhi =  1.875 deg
                deltaZ   =  .25 cm

 Enter number of cavities in phi,z directions
1 1

 Enter number of nodes per cavity (phi,z):
11 25


 275 surface nodes have been generated...
 The node numbering has the following pattern

 SINGLE CAVITY:

   ^
   |   21   22   23   24   25
   |   16   17   18   19   20
   z   11   12   13   14   15
   |    6    7    8    9   10
   |    1    2    3    4    5
   ---------- phi ---------->

 if for example 25 nodes were specified.
 where node 13 is the center point.


 Now specify which other nodes are either:
            metallic
               or
            resistive

 All surface nodes metal or resistive (1=yes):
0
 Are the nodes substrate nodes (1=yes):
0
 Enter number of metallic patches:
1
 Enter row,column of lower left corner of
 the patch on uniform grid for patch: 1
6 3
```

```
 Enter number of unknowns(edges) for each
 dimension (phi,z):
4 12

  << List of nodes constituting the patch deleted >>
  << Each of these nodes is specified by (phi,z) coord >>

 Now enter any individual nodes...
 Specify the class (metal or resistive) of all
 surface nodes which are NOT substrate nodes:
 Also indicate if 2 = metal or 3 = resistive...

 Enter node number (-999 if done):
-999 2

 0 resitive nodes entered...
 66 metal nodes entered...

 Enter number of substrate layers(INTEGER):
1

 Generating sub-surface nodes....
 Enter layer  1 thickness (cm):
0.07874

 All  550 NODES have now been created
 which form 240 elements...

 Generating edges...

 1303 edges generated....


 All element edges have been identified...

 Classifying edges....

 Number of elements: 240
 Total number of nodes:  550
 Total number of edges:  1303
 Number of interior edges:  207
 Number of metal edges:  762
 Number of aperture edges:  334
      Resistive edges:  0
      Substrate edges:  334
 Number of unknowns:  541

 Determining unknown order...

 Do you want to save this geometry (1=yes):
1
 Enter EXCALIBUR filename:
example1.exc

 Writing binary EXCALIBUR file:
 example1.exc

 Do you wish to run:
                     1) Preprocessor
                     2) FEM-BI
                     3) Impedance aperture
                     0) Exit
0
```

```
|||||||||||||||||||||||||||||||||||||||
|                                     |
|              Example 2              |
|     Four Discrete Cavities Example  |
|                                     |
|||||||||||||||||||||||||||||||||||||||

 Do you wish to run:
                    1) Preprocessor
                    2) FEM-BI
                    3) Impedance aperture
                    0) Exit
1

 Performing initialization, please wait....

 Enter radius of cylinder (cm):
15.27887
 Enter array size (phi,z) in (deg,cm):
360 6
 Wrap-around cavity entered...
 Enter center of array (z) in (cm):
0
 Enter number of grid points in (phi,z) direction:
192 25

 Discretization:
                deltaPhi =  1.875 deg
                deltaZ   =  .25 cm

 Enter 1 if ring element, 0 if rectangular array:
0
 Enter number of cavities in phi direction
4

 Enter number of nodes per cavity (phi,z):
11 25
 Enter lower left-hand (row,column): 1
0 43
 Enter lower left-hand (row,column): 2
0 91
 Enter lower left-hand (row,column): 3
0 139
 Enter lower left-hand (row,column): 4
0 187


 1100 surface nodes have been generated...
 The node numbering has the following pattern

 AZMUTHAL CAVITY ARRAY:

   ^
   |
   |  19  20  21     22  23  24
   z  13  14  15     16  17  18
   |   7   8   9     10  11  12
   |   1   2   3      4   5   6
   ---------- phi ------------>

 if for example two 3x4 cavities
 were specified


 Now specify which other nodes are either:
             metallic
                or
```

```
            resistive

 All surface nodes metal or resistive (1=yes):
0
 Are the nodes substrate nodes (1=yes):
0
 Enter number of metallic patches:
4
 Enter row,column of lower left corner of
 the patch on uniform grid for patch: 1
6 46
 Enter number of unknowns(edges) for each
 dimension (phi,z):
4 12
 << Node list deleted >>
 Enter row,column of lower left corner of
 the patch on uniform grid for patch: 2
6 94
 Enter number of unknowns(edges) for each
 dimension (phi,z):
4 12
 << Node list deleted >>
 Enter row,column of lower left corner of
 the patch on uniform grid for patch: 3
6 142
 Enter number of unknowns(edges) for each
 dimension (phi,z):
4 12
 << Node list deleted >>
 Enter row,column of lower left corner of
 the patch on uniform grid for patch: 4
6 190
 Enter number of unknowns(edges) for each
 dimension (phi,z):
4 12
 << Node list deleted >>
 Now enter any individual nodes...
 Specify the class (metal or resistive) of all
 surface nodes which are NOT substrate nodes:
 Also indicate if 2 = metal or 3 = resistive...

 Enter node number (-999 if done):
-999 2

 0 resitive nodes entered...
 261 metal nodes entered...

 Enter number of substrate layers(INTEGER):
1

 Generating sub-surface nodes....
 Enter layer  1 thickness (cm):
0.07874

 All  2200 NODES have now been created
 which form 960 elements...

 Generating edges...

 5212 edges generated....


 All element edges have been identified...
```



```
 Classifying edges....
```

```
 Number of elements: 960
 Total number of nodes:  2200
 Total number of edges:  5212
 Number of interior edges:  828
 Number of metal edges:  3048
 Number of aperture edges:  1336
      Resistive edges:  0
      Substrate edges:  1336
 Number of unknowns:  2164

 Determining unknown order...


 Do you want to save this geometry (1=yes):
1
 Enter EXCALIBUR filename:
example2.exc

 Writing binary EXCALIBUR file:
 example2.exc

 Do you wish to run:
                     1) Preprocessor
                     2) FEM-BI
                     3) Impedance aperture
                     0) Exit
0
```

```
|||||||||||||||||||||||||||||||||||||||
|                                     |
|              Example 3              |
|     Four Patches on Continuous      |
|     Wraparound Cavity Example       |
|                                     |
|||||||||||||||||||||||||||||||||||||||

 Do you wish to run:
                    1) Preprocessor
                    2) FEM-BI
                    3) Impedance aperture
                    0) Exit
1

 Performing initialization, please wait....

 Enter radius of cylinder (cm):
15.27887
 Enter array size (phi,z) in (deg,cm):
360 6
 Wrap-around cavity entered...
 Enter center of array (z) in (cm):
0
 Enter number of grid points in (phi,z) direction:
192 25

 Discretization:
                deltaPhi =  1.875 deg
                deltaZ   =  .25 cm

 Enter 1 if ring element, 0 if rectangular array:
1
 Enter number of identical rings (>=1):
1 Enter number of nodes per cavity (phi,z):
192 25
 Enter lower left-hand (row,column): 1
0 0


 4800 surface nodes have been generated...
 The node numbering has the following pattern

 SINGLE CAVITY:

   ^
   |   21   22   23   24   25
   |   16   17   18   19   20
   z   11   12   13   14   15
   |    6    7    8    9   10
   |    1    2    3    4    5
   ---------- phi ---------->

 if for example 25 nodes were specified.
 where node 13 is the center point.


 Now specify which other nodes are either:
            metallic
               or
            resistive

 All surface nodes metal or resistive (1=yes):
0
 Are the nodes substrate nodes (1=yes):
0
 Enter number of metallic patches:
```

```
4
 Enter row,column of lower left corner of
 the patch on uniform grid for patch: 1
6 46
 Enter number of unknowns(edges) for each
 dimension (phi,z):
4 12
   << Metallic node list deleted >>
 Enter row,column of lower left corner of
 the patch on uniform grid for patch: 2
6 94
 Enter number of unknowns(edges) for each
 dimension (phi,z):
4 12
   << Metallic node list deleted >>
 Enter row,column of lower left corner of
 the patch on uniform grid for patch: 3
6 142
 Enter number of unknowns(edges) for each
 dimension (phi,z):
4 12
   << Metallic node list deleted >>
 Enter row,column of lower left corner of
 the patch on uniform grid for patch: 4
6 190
 Enter number of unknowns(edges) for each
 dimension (phi,z):
4 12
 This patch includes branch...
 Enter first row nodes:
1343
 1343 176.25 -1.5
1344
 1344 178.1249 -1.5
1153
 1153 -180.0 -1.5
1154
 1154 -178.125 -1.5
1155
   << Metallic node list deleted >>
 Now enter any individual nodes...
 Specify the class (metal or resistive) of all
 surface nodes which are NOT substrate nodes:
 Also indicate if 2 = metal or 3 = resistive...

 Enter node number (-999 if done):
-999 2

 0 resitive nodes entered...
 261 metal nodes entered...

 Enter number of substrate layers(INTEGER):
1

 Generating sub-surface nodes....
 Enter layer  1 thickness (cm):
0.07874

 All  9600 NODES have now been created
 which form 4584 elements...

 Generating edges...

 23616 edges generated....

 All element edges have been identified...
```

```
 Classifying edges....

 Number of elements: 4608
 Total number of nodes:  9600
 Total number of edges:  23616
 Number of interior edges:  4416
 Number of metal edges:  10624
 Number of aperture edges:  8576
      Resistive edges:  0
      Substrate edges:  8576
 Number of unknowns:  12992

 Determining unknown order...


 Do you want to save this geometry (1=yes):
1
 Enter EXCALIBUR filename:
example3.exc

 Writing binary EXCALIBUR file:
 example3.exc

 Do you wish to run:
                    1) Preprocessor
                    2) FEM-BI
                    3) Impedance aperture
                    0) Exit
0
```

6 Operation Modes

EXCALIBUR has three main operation modes for FE-BI calculations (option 2 from the main menu). They are: input impedance vs. frequency, radiation pattern or RCS vs. frequency and single frequency radiation and RCS pattern calculations. This section will describe each mode using example 1 above.

6.1 Input Impedance – Multiple Frequencies

The first option presented is calculation of a patch antenna's input impedance at multiple frequencies. This is most useful in determining the resonant frequency of a patch antenna. The following information is required

- Choose item 2 (FE-BI) from main menu.
- Enter the stored binary geometry file.
- Enter 1 if all elements have the same material parameters.
- Enter complex permittivity.
- Enter complex permeability.
- Enter BiCG convergence tolerance, minimum and maximum number of iterations.
- Enter 1 to monitor convergence.
- Enter 1 for diagonal preconditioning and 0 for no preconditioning.
- Enter 1 for frequency sweep of the input impedance.
- Enter name of file to store the input impedance.
- Enter number of probe feeds.
- Enter location of each feed in terms of (ϕ=degrees, z=cm).
- Enter which layer in which the feed is embedded.
- Enter complex current for this feed.
- Enter number of impedance post loads.
- Enter frequency range (in GHz) for this sweep.
- Return to main menu.

The input impedance for 3.1 GHz to 3.3 GHz computed every 10 MHz is shown in figure 9. The transcript for computing the input impedance of an axially polarized 2 cm $\times$ 3 cm patch in a 5 cm $\times$ 6 cm cavity is given on the following page.

```
 Do you wish to run:
                     1) Preprocessor
                     2) FEM-BI
                     3) Impedance aperture
                     0) Exit
2

 Performing initialization, please wait....

 Enter EXCALIBUR filename:
example1.exc
 Reading excalibur file: example1.exc

 Material Parameter Specification....
 Is the material filling constant (1=yes,0=no)?
1
 Enter relative permittivity [real,imaginary]:
2.17 0
 Enter relative permeability [real,imaginary]:
1 0

 Checking dimension allocations...

 Number of Boundary Integral Unknowns: 334
 Total number of UNKNOWNS: 541

Enter tolerance, minimum and maximum iterations:
0.01 2 500
 Do you wish to monitor convergence (0=no,1-yes)?
0
 Do you want:  0 = no preconditioning, 1 = diagonal?
1
 Do you want to compute:
      0 = RCS/Pattern, 1 = Zin, 2 = Freq. Sweep?
1
 Enter Zin filename:
example1.zin

 ||||||||||||||||||||||||||||||||||||||||
 |     PROBE FEED INFORMATION            |
 ||||||||||||||||||||||||||||||||||||||||

 Enter number of feeds:
1
 Enter feed location (phi,z) in (deg,cm):
0 -0.375
 Enter layer number of feed <=: 1
1
 Enter mag,phase of probe current (amp,deg):
1 0

 ||||||||||||||||||||||||||||||||||||||||
 |     IMPEDANCE LOAD INFORMATION        |
 ||||||||||||||||||||||||||||||||||||||||

 Enter number of loads:
0

 Enter start,stop and increment freq. (GHz):
3.1 3.3 0.01
 << Data shown in attached figure >>
```

6.2 Pattern – Multiple Frequencies

The next option presented is calculation of a radiation or RCS pattern at multiple frequencies. This is useful in computing the variation of gain or RCS with respect to frequency. Usually, a single observation angle is specified although multiple angles are allowed. This mode permits radiation, bistatic and backscatter computations. In addition, the input impedance as a function of frequency is stored if a probe feed is used for excitation. In this example, we compute the backscatter at normal incidence for an E_z-polarized plane wave as a function of frequency. The required information is

- Choose item 2 (FE-BI) from main menu.
- Enter the stored binary geometry file.
- Enter 1 if all elements have the same material parameters.
- Enter complex permittivity.
- Enter complex permeability.
- Enter BiCG convergence tolerance, minimum and maximum number of iterations.
- Enter 1 to monitor convergence.
- Enter 1 for diagonal preconditioning and 0 for no preconditioning.
- Enter 2 for frequency sweep of the far-zone fields.
- Enter name of file to store the input impedance.
- Enter name of file to store the RCS or Gain.
- Enter observation type (0 = backscatter).
- Enter start, stop and increment azimuth (ϕ) angles (in degrees).
- Enter start, stop and increment elevation (θ) angles (in degrees).
- Enter polarization angle (0 = E-pol, 90 = H-pol).
- Enter RCS filename.
- Enter number of probe feeds.
- Enter number of impedance post loads.
- Enter frequency range (in GHz) for this sweep.
- Return to main menu.

The RCS for 3.1 GHz to 3.3 GHz computed every 10 MHz is shown in figure 10. The transcript for backscatter calculations for backscatter calculations is shown on the next page.

```
 Do you wish to run:
                      1) Preprocessor
                      2) FEM-BI
                      3) Impedance aperture
                      0) Exit
2
 Performing initialization, please wait....

 Enter EXCALIBUR filename:
example1.exc
 Reading excalibur file: example1.exc

 Material Parameter Specification....
 Is the material filling constant (1=yes,0=no)?
1
 Enter relative permittivity [real,imaginary]:
2.17 0
 Enter relative permeability [real,imaginary]:
1 0
 Checking dimension allocations...
 Number of Boundary Integral Unknowns: 334
 Total number of UNKNOWNS: 541
Enter tolerance, minimum and maximum iterations:
0.01 2 500
 Do you wish to monitor convergence (0=no,1-yes)?
0
 Do you want:  0 = no preconditioning, 1 = diagonal?
1
 Do you want to compute:
      0 = RCS/Pattern, 1 = Zin, 2 = Freq. Sweep?
2
 Enter Zin filename:
test.zin
 Enter Frequency sweep data filename:
example1.fsw
 Enter observation type:
                          0) Backscatter
                          1) Bistatic
                          2) Radiation
0

 Enter start,stop, and increment azmuth angles [deg]:
0 0 1
 Enter start,stop,and increment elevation angles [deg]:
90 90 1
 Enter polarization angle [0 <= alpha <= 90 deg]:
            Ephi=0:  alpha = 0
            Etheta=0:  alpha = 90
0
 Enter ouput RCS filename [<= 40 characters]:
junk

 ||||||||||||||||||||||||||||||||||||||||
 |     PROBE FEED INFORMATION            |
 ||||||||||||||||||||||||||||||||||||||||

 Enter number of feeds:
0
 ||||||||||||||||||||||||||||||||||||||||
 |     IMPEDANCE LOAD INFORMATION        |
 ||||||||||||||||||||||||||||||||||||||||

 Enter number of loads:
0
 Enter start,stop and increment freq. (GHz):
3.1 3.3 0.01
```


C-2

6.3 Pattern – Single Frequency

The final operation mode is radiation and RCS pattern calculations at a single frequency. Of course, for the case of an antenna, the input impedance is also computed. This mode is generally used for multiple incident and observation angle applications. The only difference between this mode and the previous two modes is the option to save the admittance matrix in binary format. Since this matrix is excitation independent (though still frequency dependent), it can save time for multiple runs of a large geometry if this matrix is stored and then read in for each run. The required inputs are

- Choose item 2 (FE-BI) from main menu.
- Enter the stored binary geometry file.
- Enter 1 if all elements have the same material parameters.
- Enter complex permittivity.
- Enter complex permeability.
- Enter BiCG convergence tolerance, minimum and maximum number of iterations.
- Enter 1 to monitor convergence.
- Enter 1 for diagonal preconditioning and 0 for no preconditioning.
- Enter 0 for single frequency operation.
- Enter matrix storage/read option(1 to store, 2 to read, 0 to do nothing).
- Enter six (6) character filename for matrix storage/read.
- Enter observation type (1 = bistatic).
- Enter incidence angle (ϕ,θ).
- Enter start, stop and increment azimuth (ϕ) angles (in degrees).
- Enter start, stop and increment elevation (θ) angles (in degrees).
- Enter polarization angle (0 = E-pol, 90 = H-pol).
- Enter RCS filename.
- Enter number of probe feeds.
- Enter number of impedance post loads.
- Enter frequency (in GHz).
- Return to main menu.

This option is illustrated in the next session transcript for bistatic scattering and radiation pattern calculations.

```
 Do you wish to run:
                     1) Preprocessor
                     2) FEM-BI
                     3) Impedance aperture
                     0) Exit
2
 Performing initialization, please wait....
 Enter EXCALIBUR filename:
example1.exc
 Reading excalibur file: example1.exc
 Material Parameter Specification....
 Is the material filling constant (1=yes,0=no)?
1
 Enter relative permittivity [real,imaginary]:
2.17 0
 Enter relative permeability [real,imaginary]:
1 0
 Checking dimension allocations...
 Number of Boundary Integral Unknowns: 334
 Total number of UNKNOWNS: 541
Enter tolerance, minimum and maximum iterations:
0.01 2 500
 Do you wish to monitor convergence (0=no,1-yes)?
0
 Do you want:  0 = no preconditioning, 1 = diagonal?
1
 Do you want to compute:
      0 = RCS/Pattern, 1 = Zin, 2 = Freq. Sweep?
0
 Save the BI arrays in a file (0=no,1=yes,2=read)?
1
 All BI files will have the following form:
 <filename>.guu,<filename>.guv, etc.
 Enter BI binary filename(must be six(6) char):
exampl
 Enter observation type:
                          0) Backscatter
                          1) Bistatic
                          2) Radiation
1
 Enter incident phi,theta [deg]:
0 90
 Enter start,stop, and increment azmuth angles [deg]:
-180 180 1
 Enter start,stop,and increment elevation angles [deg]:
90 90 1
 Enter polarization angle [0 <= alpha <= 90 deg]:
            Ephi=0:  alpha = 0
            Etheta=0:  alpha = 90
0
 Enter ouput RCS filename [<= 40 characters]:
exampl.bi
 Enter frequency (GHz):
3.3
 ||||||||||||||||||||||||||||||||||||||||
 |     PROBE FEED INFORMATION            |
 ||||||||||||||||||||||||||||||||||||||||

 Enter number of feeds:
1
 Enter feed location (phi,z) in (deg,cm):
0 -0.375
 Enter layer number of feed <=: 1
1
 Enter mag,phase of probe current (amp,deg):
1 0
```

```
 ||||||||||||||||||||||||||||||||||||||
 |     IMPEDANCE LOAD INFORMATION       |
 ||||||||||||||||||||||||||||||||||||||

 Enter number of loads:
0
 Writing BI binary files...
 Generate bistatic excitation vector...
 Solve it...

  << Pattern deleted. >>

 Run anouther excitation? (1=yes,0=no)
1

 Enter observation type:
                          0) Backscatter
                          1) Bistatic
                          2) Radiation
2
 Enter start,stop, and increment azmuth angles [deg]:
-180 180 1
 Enter start,stop,and increment elevation angles [deg]:
90 90 1
 Enter ouput RCS filename [<= 40 characters]:
exampl.pat
 Enter normalized pattern filename:
exampl.norm
 Solve it...
  << Pattern deleted. >>
 Run anouther excitation? (1=yes,0=no)
0

 Do you wish to run:
                     1) Preprocessor
                     2) FEM-BI
                     3) Impedance aperture
                     0) Exit
0
```

The bistatic patterns taken at 3.3 GHz for the three geometry configurations presented in this manual are shown in figure 11 The corresponding antenna pattern comparisonat 3.3 GHz is shown in figure 12

7 Concluding Remarks

This user manual presented some basic operation information for the FE-BI code, EXCALIBUR. This presentation was only meant to get an initial user started. As one becomes experienced with the code, additional features such as 2-D patch array modeling, multiple feed arrays and use of lumped impedance loads may prove useful. Indeed, an experienced user will find that custom features may readily be added to EXCALIBUR. For example, currently EXCALIBUR allows entry of material parameters either for the entire substrate, each layer of the substrate or on an element-by-element basis. This subroutine *material* in file *excalibur.f* may readily be modified by the user to input a custom inhomogeneous substrate.

The code is fairly "dummy proof". If the user enters data which is not expected by EXCALIBUR such as a character when an integer is expected or an angle greater than 360°, the code will prompt the user to re-enter the requested data. Additionally, the storage allocation parameters in *excalibur.inc* must be set by the user prior to compilation. If a particular parameter is too small for a given run, the code will halt and suggest a new value for the offensive parameter. The user must reset that parameter, recompile and run the code again. The program also estimates the amount of RAM required at the start of a run. This estimate is based on the storage required by the arrays in *excalibur.inc* plus some scratch arrays. Each complex number is assumed to require eight bytes and each integer and real number require four bytes. The user should consider this estimate to be a slightly lower than the actual consumed memory.

References

[1] L.C. Kempel and J.L. Volakis, "Scattering by cavity-backed antennas on a circular cylinder," submitted to *IEEE Trans. Antennas and Propagat.*.

[2] L.C. Kempel, J.L. Volakis and R. Sliva, "Radiation by cavity-backed antennas on a circular cylinder," to be submitted to *IEEE Trans. Antennas and Propagat.*.

[3] Sorenson *et al*, *IEEE Trans. Acoustics, Speech and Signal Processing*, pp. 152-156, Feb. 1986.

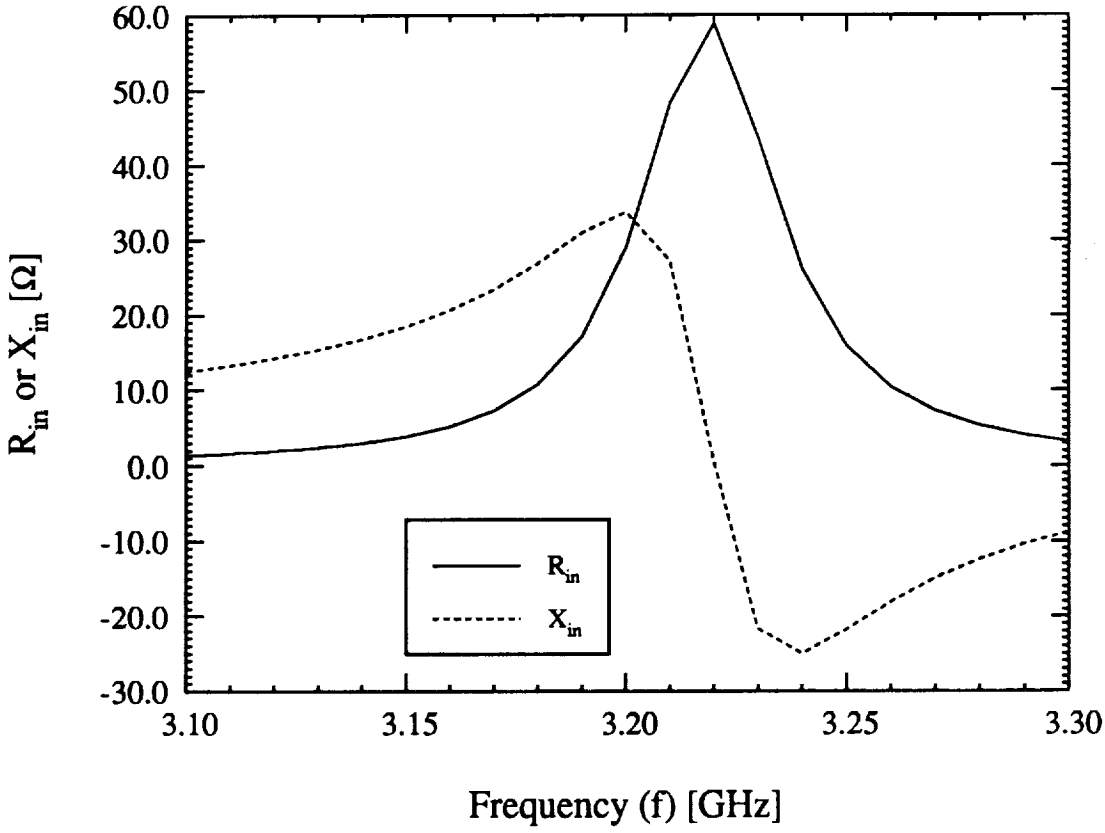

Figure 9: Input impedance vs. frequency for the axially polarized patch antenna which is 2 cm × 3 cm in a 5 cm × 6 cm cavity.

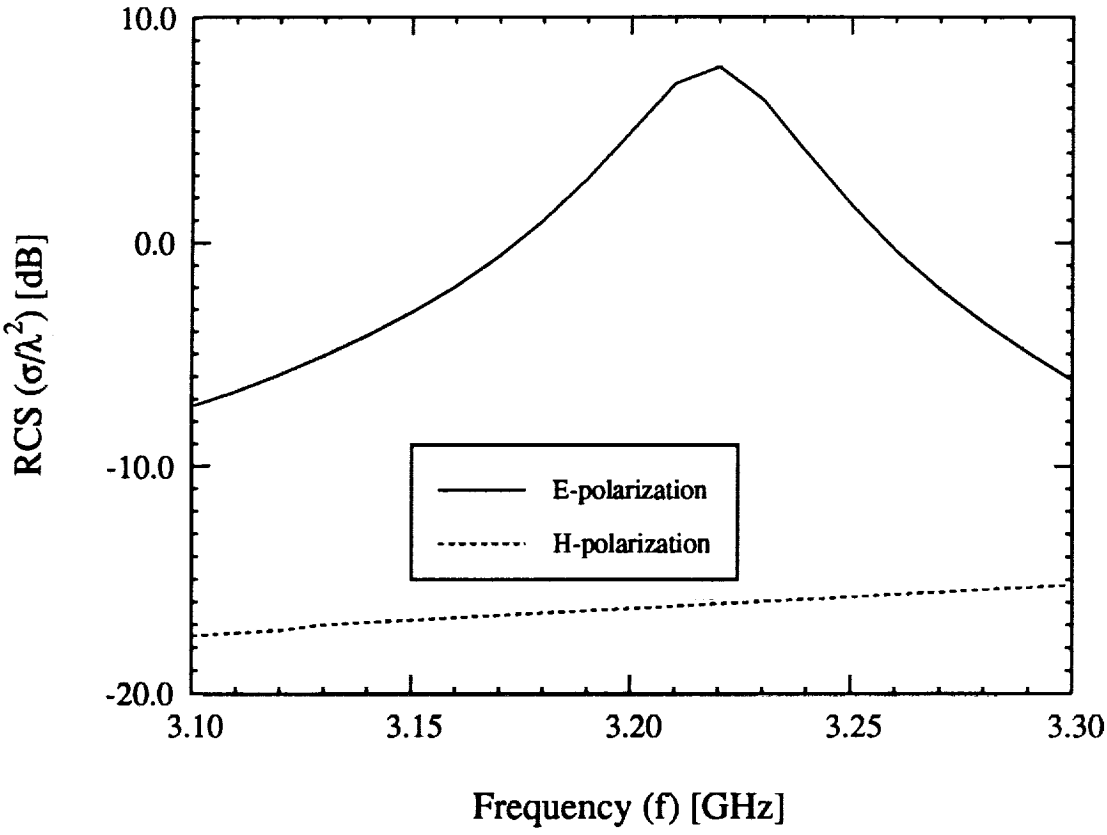

Figure 10: RCS vs. frequency for a patch antenna which is 2 cm × 3 cm in a 5 cm × 6 cm cavity.

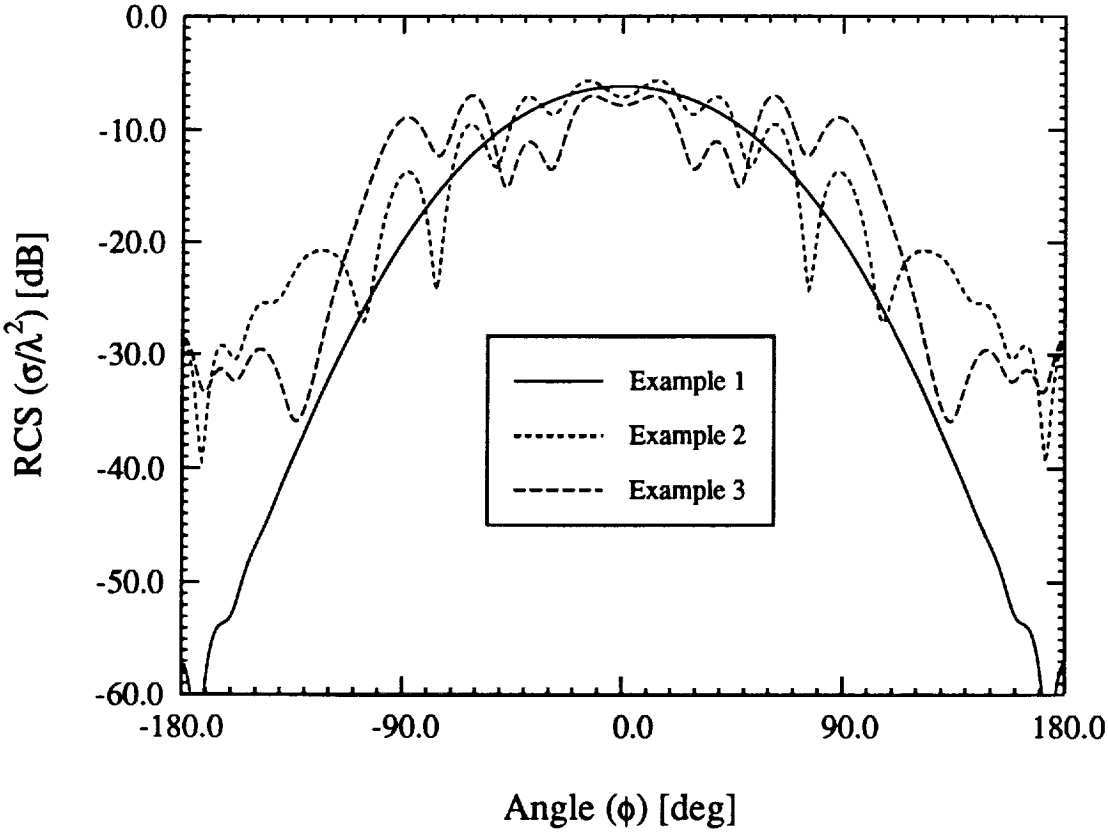

Figure 11: E-polarized bistatic patterns for a 2 cm $\times$ 3 cm embedded in the three different geometries presented in this manual. The incidence angle is $(0°, 90°)$ and observation is in the $\theta = 90°$ plane.

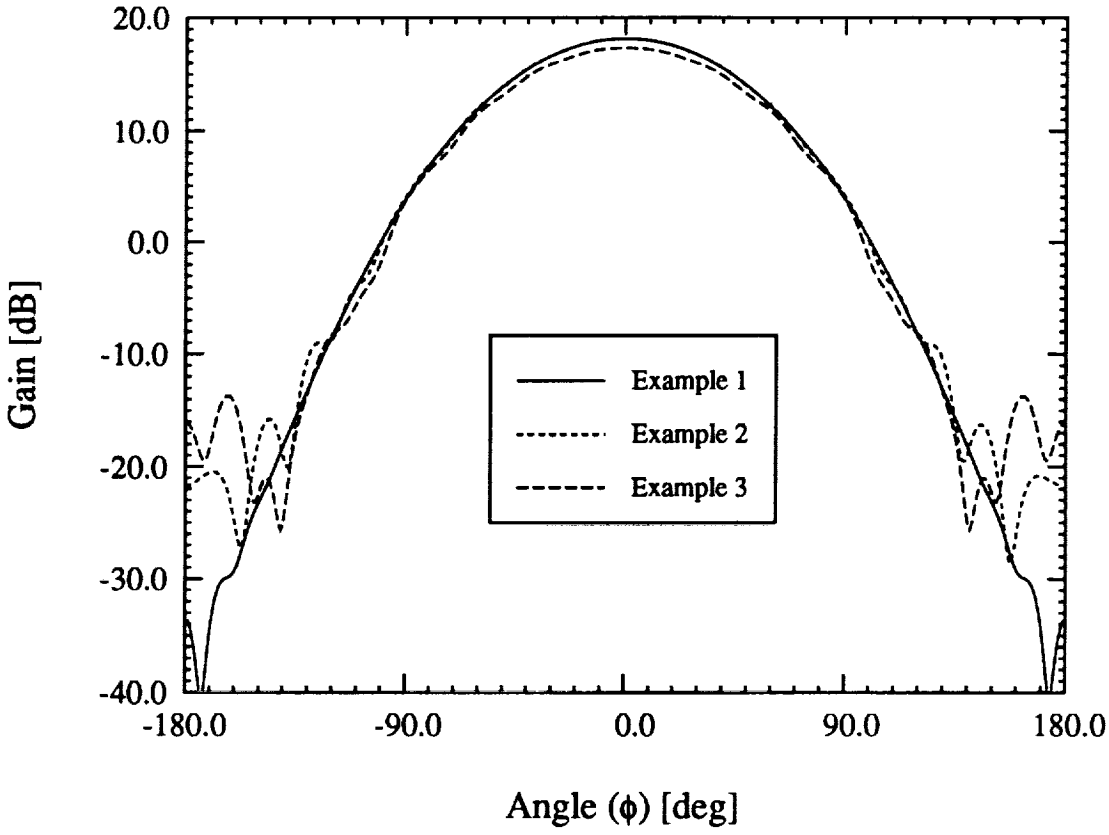

Figure 12: Axially polarized H-plane patterns for a 2 cm $\times$ 3 cm embedded in the three different geometries presented in this manual.

APPENDIX 1

A NOTE ON APPLYING NEW VECTOR ABCS TO PATCH ANTENNAS ON A CIRCULAR CYLINDER

Leo C. Kempel and John L. Volakis
Radiation Laboratory
Department of Electrical Engineering and Computer Science
University of Michigan, Ann Arbor, MI 48109-2122

Recently, we developed a Finite Element-Boundary Integral (FE-BI) method which may be used to accurately model the scattering and radiation by conformal patch antennas. The use of a boundary integral to provide an exact mesh closure condition results in a rigorous formulation. When coupled with a Biconjugate Gradient-Fast Fourier Transform (BiCG-FFT) solver, the resulting computer code possesses both low memory and low computational demand. However, boundary integral closure involves a dyadic Green's function which necessarily limits its extension to coated geometries. Although it is possible to construct a suitable Green's function for multilayered superstrates, the resulting formulation is both complex and bulky. Furthermore, this approach cannot be extended in a rigorous manner to more general doubly curved structures.

Another hybrid FE method which has been used for very large 3-D scattering calculations at the University of Michigan is the finite element-absorbing boundary condition (FE-ABC) method. ABCs provide an approximate mesh closure which maintains a highly sparse matrix for the whole system. We propose utilizing a new conformal ABC (A. Chatterjee and J.L. Volakis, *Microwave and Optical Tech. Letters*, **6**, No. 16, pp. 886-889, Dec. 20 1993) which allows the closure surface to be brought quite close to the cavity aperture. As a result, the number of unknowns required is significantly less than the number required if a traditional spherical closure surface/boundary condition is used.

We have applied the second order ABC to radiation and scattering by cavity-backed patch antennas which are embedded in a metallic cylinder. Although extensive testing has not as of yet been accomplished, the preliminary results are encouraging. We looked at a 2 cm $\times$ 3 cm patch antenna which was printed on a 5 cm $\times$ 6 cm $\times$ 0.07874 cm substrate which had a dielectric constant of $\epsilon_r = 2.17$. The second order ABC was place 0.5λ from the cavity aperture as shown in figure 1. Two comparisons with the FE-BI formulation were performed. The first involved bistatic scattering with normal incidence ($\phi_i = 0°, \theta_i = 90°$) and observation in the $\theta = 90°$ plane for an E_z-polarized plane wave which is shown in figure 2. A radiation pattern for the same antenna is shown in figure 3 where the resonant frequency is 3.3 GHz. Since this is an axially polarized element, figure 3 is an H-plane pattern.

The scattering and radiation example given herein involves a conformal antenna element without a covering superstrate. The FE-ABC formulation may be readily modified to account for such a covering which may consist of multiple inhomogeneous layers as shown in figure 1. A future report will develop the formulation for both covered and uncovered elements and it will provide suitable validation of the method.

In addition, we shall investigate whether the near-field performance of the FE-ABC method is sufficient for input and mutual impedance calculations. Having shown that the FE-ABC approach can indeed be used for conformal antennas on singly curved surfaces, we may in confidence develop a similar formulation for antennas mounted on doubly curved surfaces.

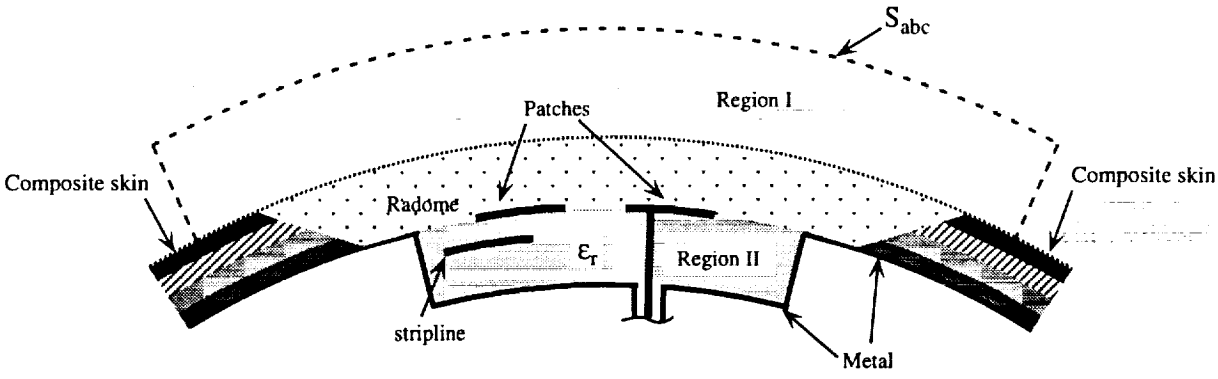

Figure 1: Coated cavity-backed patch antenna with ABC mesh termination.

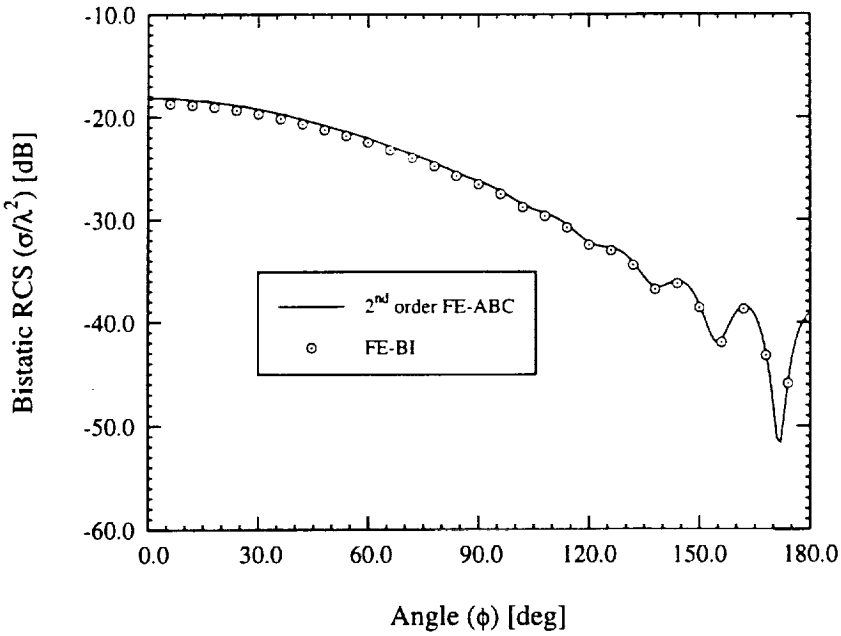

Figure 2: Comparison of 2^{nd} order conformal ABC mesh closure condition with the exact boundary integral condition for bistatic scattering. The patch was 2 cm $\times$ 3 cm printed on a 5 cm $\times$ 6 cm $\times$ 0.07874 cm dielectric substrate ($\epsilon_r = 2.17$). The ABC was placed 0.5λ from the aperture and the operating frequency was 3.0 GHz. The E_z-polarized plane wave was incident from ($\phi_i = 0^0, \theta_i = 90^o$) and observation is in the $\theta = 90^o$ plane.

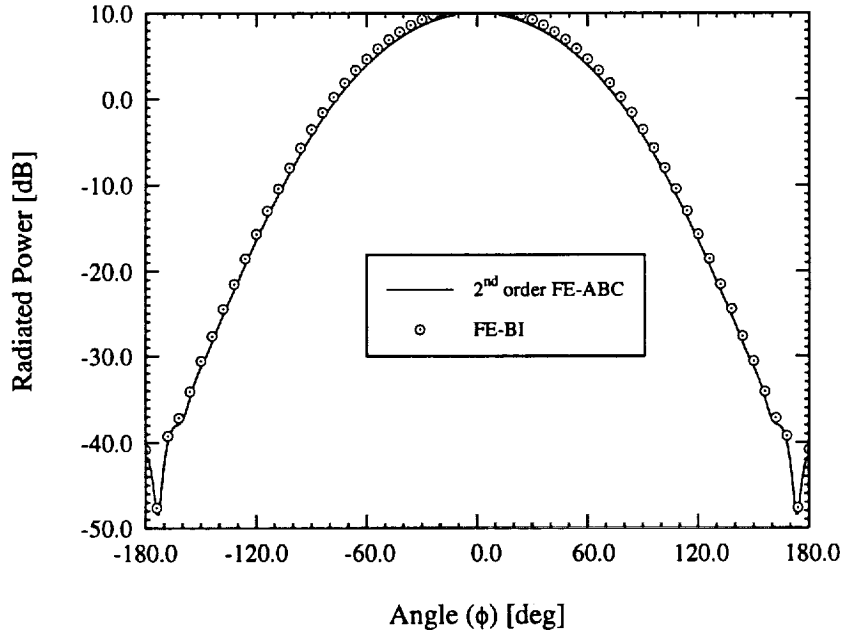

Figure 3: Comparison of 2^{nd} order conformal ABC mesh closure condition with the exact boundary integral condition for antenna pattern calculations. The geometry is identical to the one used in figure 2. The operating frequency was 3.3 GHz. The feed point was ($\phi_s = 0^o, z_s = -0.375$ cm) which results in axial polarization and observation is made in the H-plane.

APPENDIX 2

FE-BI implementation for coated planar platforms

Consider the cavity recessed in a coated ground plane as shown in Fig 1. The coating is assumed to be of thickness d and of relative permittivity ϵ_r. We will denote the free space region above the coating ($z > d$) as region 1, the region inside the coating ($0 < z < d$) as region 2 and that inside the cavity ($-c < z < 0$) as region 3. We will assume that the cavity is filled with an inhomogeneous material having a relative permittivity $\epsilon_{rc}(\mathbf{r})$ and relative permeability $\mu_{rc}(\mathbf{r})$. In accordance with the equivalence principle, the fields in regions 2 and 3 can be decoupled by closing the aperture with a perfect conductor and introduce the equivalent magnetic current

$$\mathbf{M} = \mathbf{E} \times \hat{z} \tag{1}$$

over the extent of the aperture, where $\mathbf{E}$ is the electric field at the aperture ($z = 0$). The magnetic field is then due to the radiation caused by the equivalent current $\mathbf{M}$ residing on the ground plane and is given by

$$\mathbf{H}(\mathbf{r}) = \mathbf{H}^i(\mathbf{r}) + \mathbf{H}^r(\mathbf{r}) - jkY\left[\bar{\mathbf{I}} + \frac{1}{k^2}\nabla\nabla\right] \cdot \mathbf{F} \tag{2}$$

where $\mathbf{F}$ is the magnetic vector potential and is given in terms of the dyadic Green's function of the coating as

$$\mathbf{F} = \iint_S \bar{\mathbf{G}}(\mathbf{r}, \mathbf{r}') \cdot \mathbf{M}(\mathbf{r}') dS' \tag{3}$$

and $\mathbf{H}^i$ is the incident field, $\mathbf{H}^r$ is that reflected by the coated ground plane without the aperture, S denotes the planar surface area of the aperture. If the conducting surfaces are restricted to horizontal planes, as is the situation here, we can find an equivalent scalar Green's function G_V such that [1]

$$\nabla \cdot \bar{\mathbf{G}} = \nabla' G_V(\mathbf{r}, \mathbf{r}') \tag{4}$$

where

$$G_V = \frac{\omega}{k_\rho^2 k_x} \frac{\partial G_E^{zx}}{\partial z} - \left(\frac{k}{k_\rho}\right)^2 \frac{G_H^{zx}}{jk_y\epsilon_r} \tag{5}$$

More specifically, the function $\mathbf{P}$ defined in [2] is identically zero. Now consider F_S as

$$F_S = -jkY\left[\bar{\mathbf{I}} + \frac{1}{k^2}\nabla\nabla\right]\cdot\mathbf{F} \tag{6}$$

Making use of (4) in (6) we can write F_S as

$$F_S = -jkY\iint_S \bar{\mathbf{G}}\cdot\mathbf{M}(\mathbf{r}')dS' + \frac{jY}{k}\nabla\iint_S \nabla'\cdot\mathbf{M}(\mathbf{r}')G_V(\mathbf{r},\mathbf{r}')dS' \tag{7}$$

The required components of the Green's function in (7) are given by

$$G_{xx} = \int_{-\infty}^{\infty}\int_{-\infty}^{\infty}\tilde{G_{xx}}e^{-jk_2(z-d)}e^{jk_x(x-x')}e^{jk_y(y-y')}dk_xdk_y \tag{8}$$

$$G_{yx} = \int_{-\infty}^{\infty}\int_{-\infty}^{\infty}\tilde{G_{yx}}e^{-jk_2(z-d)}e^{jk_x(x-x')}e^{jk_y(y-y')}dk_xdk_y \tag{9}$$

$$G_{yy} = \int_{-\infty}^{\infty}\int_{-\infty}^{\infty}\tilde{G_{yy}}e^{-jk_2(z-d)}e^{jk_x(x-x')}e^{jk_y(y-y')}dk_xdk_y \tag{10}$$

$$G_{xy} = \int_{-\infty}^{\infty}\int_{-\infty}^{\infty}\tilde{G_{xy}}e^{-jk_2(z-d)}e^{jk_x(x-x')}e^{jk_y(y-y')}dk_xdk_y \tag{11}$$

where

$$\tilde{G_{xx}} = \left(\epsilon_r k_0^2 k_y^2\Gamma_1 - k_1^2 k_x^2\Gamma_2\right)/\left(8\pi^2 k_0^2 k_1\beta^2\right) \tag{12}$$

$$\tilde{G_{yy}} = \left(\epsilon_r k_0^2 k_x^2\Gamma_1 - k_1^2 k_y^2\Gamma_2\right)/\left(8\pi^2 k_0^2 k_1\beta^2\right) \tag{13}$$

$$\begin{aligned}\tilde{G_{xy}} &= \tilde{G_{yx}} \\ &= -k_x k_y\left(k_1^2\Gamma_2 + \epsilon_r k_0^2\Gamma_1\right)/\left(8\pi^2 k_0^2 k_1\beta^2\right)\end{aligned} \tag{14}$$

with Γ_1 and Γ_2 given by

$$\Gamma_1 = \frac{\epsilon_r k_2\sin(k_1 d) - jk_1\cos(k_1 d)}{\epsilon_r k_2\cos(k_1 d) + jk_1\sin(k_1 d)} \tag{15}$$

$$\Gamma_2 = \frac{k_2\cos(k_1 d) + jk_1\sin(k_1 d)}{k_2\sin(k_1 d) - jk_1\cos(k_1 d)} \tag{16}$$

Also,

$$G_{zx}^E = \int_{-\infty}^{\infty}\int_{-\infty}^{\infty}\tilde{G_{zx}^E}e^{jk_x(x-x')}e^{jk_y(y-y')}dk_xdk_y \tag{17}$$

$$G_{zx}^{H} = \int_{-\infty}^{\infty}\int_{-\infty}^{\infty} \tilde{G_{zx}^{H}} e^{jk_x(x-x')} e^{jk_y(y-y')} dk_x dk_y \tag{18}$$

with

$$\tilde{G_{zx}^{E}} = \frac{1}{4\pi^2}\left[C\cos(k_1 z) + D\sin(k_1 z)\right] \tag{19}$$

where

$$C = -\frac{k_y\left[k_1\cos(k_1 d) + j\epsilon_r k_2 \sin(k_1 d)\right]}{k_1\left[\epsilon_r k_2\cos(k_1 d) + jk_1\sin(k_1 d)\right]} \tag{20}$$

$$D = \frac{jk_y}{k_1} \tag{21}$$

and

$$\tilde{G_{zx}^{H}} = \frac{1}{4\pi^2}\left[E\sin(k_1 z) + F\cos(k_1 z)\right] \tag{22}$$

where

$$E = \frac{k_x\left[k_1\sin(k_1 d) - jk_2\cos(k_1 d)\right]}{k_0 Z_0\left[k_1\cos(k_1 d) + jk_2\sin(k_1 d)\right]} \tag{23}$$

$$F = \frac{k_x}{k_0 Z_0} \tag{24}$$

with $k_1^2 = \epsilon_r k_0^2 - \beta^2$, $k_2^2 = k_0^2 - \beta^2$ and $\beta^2 = k_x^2 + k_y^2$. After weighting (7) becomes

$$\begin{aligned} F_S &= -jkY \iint_S \mathbf{M}(\mathbf{r}) \cdot \iint_S \bar{\mathbf{G}} \cdot \mathbf{M}(\mathbf{r}')dS\, dS' \\ &\quad + \frac{jY}{k} \iint_S \nabla\cdot\mathbf{M}(\mathbf{r}) \iint_S \nabla'\cdot\mathbf{M}(\mathbf{r}')G_V(\mathbf{r},\mathbf{r}')dS\, dS' \end{aligned} \tag{25}$$

The fields in region 3 (the cavity region) are formulated employing the finite element method [3].

Evaluation of the Sommerfeld integrals using the Chebyshev decomposition method

This is a new, fast and efficient method [4] of evaluating Sommerfeld integrals encountered, when we use a spectral-domain transformation to calculate fields of a dipole source in a homogeneous space or in a layered medium with planar boundaries. The integration is based on the decomposition of the integrand into Chebyshev polynomials, the oscillatory nature of which facilitates rapid

integration of the fast oscillating integrands. In (8)-(18) we encounter Fourier transform pairs given by

$$\tilde{f}(k_x, k_y) = \frac{1}{2\pi} \int^{\infty} \int_{-\infty} f(x,y) e^{-jk_x x - jk_y y}\, dxdy \tag{26}$$

$$f(x,y) = \frac{1}{2\pi} \int^{\infty} \int_{-\infty} \tilde{f}(k_x, k_y) e^{jk_x x + jk_y y}\, dk_x dk_y \tag{27}$$

Introducing the Bessel function as

$$J_0(k_\rho \rho) = \frac{1}{2\pi} \int_0^{2\pi} e^{jk_\rho \rho \cos(\alpha - \phi)} d\phi \tag{28}$$

we have

$$\tilde{f}(k_\rho) = \int_0^{\infty} J_0(k_\rho \rho) f(\rho) \rho d\rho \tag{29}$$

$$f\rho = \int_0^{\infty} J_0(k_\rho \rho) \tilde{f}(k_\rho) k_\rho dk_\rho \tag{30}$$

(29) and (30) is the Fourier-Bessel or Hankel integral transform pair. Inverse Hankel tranforms such as (30) are the generic form of Sommerfeld integrals which we consider for the demonstration of this method. Transverse derivatives of $f(\rho)$ can be expressed as :

$$\frac{\partial f}{\partial x} = -\cos\phi \int_0^{\infty} J_1(k_\rho \rho) \tilde{f}(k_\rho) k_\rho^2 dk_\rho \tag{31}$$

Hence the most general Sommerfeld integral is written as

$$SI = \int_0^{\infty} J_m(k_\rho \rho) h(k_\rho)\, dk_\rho \tag{32}$$

where J_m is the Bessel function of the first kind of order m. Assuming that $h(k_\rho)$ has a pole at $k_\rho = k_P$ $(0 < k_P < \sqrt{\epsilon_r} k_0)$

$$\begin{aligned} SI \;=\; & \int_0^{\sqrt{\epsilon_r} k_0} (J_m(k_\rho \rho) h(k_\rho) - F(k_\rho))\, dk_\rho \\ & + \int_0^{\sqrt{\epsilon_r} k_0} F(k_\rho)\, dk_\rho \\ & + \int_{\sqrt{\epsilon_r} k_0}^{\infty} J_m(k_\rho \rho) h(k_\rho)\, dk_\rho \end{aligned} \tag{33}$$

with

$$F(k_\rho) = \frac{A}{k_\rho - k_P} \tag{34}$$

where A is the residue of $J_m(k_\rho\rho)h(k_\rho)$ at $k_\rho = k_P$. The second integral in (33) is solved analytically. Next we make the behaviour of the integrands in (33) smoother by applying a change of variables, for the first and third integrands respectively

$$k_\rho = \sqrt{\epsilon_r}k_0 \sin\xi \tag{35}$$

and

$$k_\rho = \sqrt{\epsilon_r}k_0 \cosh\xi \tag{36}$$

Transforming the domain of integration to the domain of definition of the Chebyshev polynomials the first integral of (33) becomes

$$\frac{\pi}{4}\int_{-1}^{1}\frac{f_1(z_1)}{\sqrt{1-z_1^2}}dz_1 + j\frac{\pi}{4}\int_{-1}^{1}\frac{f_2(z_1)}{\sqrt{1-z_1^2}}dz_1 \tag{37}$$

with

$$f_{1,2}(z) = Re, Im\left((J_m(k_\rho\rho)h(k_\rho) - F(k_\rho))\sqrt{1-k_\rho^2}\sqrt{1-z^2}\right) \tag{38}$$

$$k_\rho = \sqrt{\epsilon_r}k_0 \sin\left(\frac{\pi}{4}(z+1)\right) \tag{39}$$

Similarly transforming the domain of integration for the third integral in (33) and truncating the upper limit at a and b for the real and imaginary parts respectively we have

$$\frac{a}{2}\int_{-1}^{1}\frac{f_3(z_2)f_5(z_2)}{\sqrt{1-z_2^2}}dz_2 + j\frac{b}{2}\int_{-1}^{1}\frac{f_4(z_3)f_6(z_3)}{\sqrt{1-z_3^2}}dz_3 \tag{40}$$

with

$$\begin{aligned} f_{3,4}(z) &= J_m\left(\sqrt{\epsilon_r}k_0\cosh\left(\frac{a,b}{2}(z+1)\right)\rho\right) \\ &\quad \left(\sqrt{\epsilon_r}k_0\sinh\left(\frac{a,b}{2}(z+1)\right)\right)\sqrt{1-z^2} \end{aligned} \tag{41}$$

$$f_{5,6}(z) = Re, Im\left(h\left(\sqrt{\epsilon_r}k_0\cosh\left(\frac{a,b}{2}(z+1)\right)\right)\right) \tag{42}$$

Now $f_1(z)$ to $f_6(z)$ are fiited with Chebyshev polynomials so that

$$f(z) \approx \left[\sum_{k=1}^{N} c_k T_{k-1}(z)\right] - \frac{1}{2}c_1 \tag{43}$$

with

$$c_j = \frac{2}{N}\sum_{k=1}^{N} f(z_k)T_{j-1}(z_k) \tag{44}$$

The orthogonal property of these polynomials is defined as

$$\int_{-1}^{1} \frac{T_i(z)T_j(z)}{\sqrt{1-z^2}}dz = \begin{cases} 0 & (i \neq j) \\ \frac{\pi}{2} & (i = j \neq 0) \\ \pi & (i = j = 0) \end{cases} \tag{45}$$

Applying the orthogonal property we evaluate the SI as

$$\begin{aligned} SI \approx & \frac{\pi}{2}\frac{\pi}{4}(c_{1,1} + jc_{2,1}) + \frac{\pi}{2}\left(\frac{a}{2}f(c_3, c_5) + j\frac{b}{2}f(c_4, c_6)\right) \\ & + A\ln\left(\frac{\sqrt{\epsilon_r}k_0 - k_P}{k_P}\right) - j\pi A \end{aligned} \tag{46}$$

with

$$f(c_i, c_j) = \sum_{k=0}^{min(N_i,N_j)-1} \left(\frac{2-\delta(k)}{2}\right) c_{i,k+1}c_{j,k+1} \tag{47}$$

Using the Chebyshev decomposition method, a typical Sommerfeld integral encountered while analysing a horizontal electric dipole in the x direction above a ground with relative pemittivity ϵ_r and conductivity σ, is evaluated. The integral is expressed as

$$A_x = 2\int_0^{\infty} J_0(k_\rho \rho)\left(\frac{e^{-u_0|z+h|}}{u_0 + u}\right) k_\rho dk_\rho \tag{48}$$

where

$$\rho = \sqrt{x^2 + y^2} \quad u_0 = \sqrt{k_\rho^2 - k^2} \tag{49}$$

$$u = \sqrt{k_\rho^2 - N^2k^2} \quad N^2 = \epsilon_r - j\frac{\sigma}{\omega\epsilon_0} \tag{50}$$

and k is the free space propagation constant. For this evaluation z (the observer height) to be equal to the dipole height h ($\lambda/50$). The results of this evaluation is shown in Fig 2.

References

[1] T. Itoh, ed., Numerical Techniques for Microwave and Millimeter- wave Passive Structures, Wiley-Interscience, 1989.

[2] K. A. Michlaski, "Electromagnetic Scattering and Radiation by Surfaces of Arbitary Shape in Layered Media, Part 1: Theory," *IEEE Trans. Antennas Propagat.*, vol.38, no. 3, pp.335-344, March 1990.

[3] J. M. Jin and J. L. Volakis, "A Finite Element-Boundary Integral Formulation for Scattering by Three-Dimensional Cavity-Backed Apertures, "*IEEE Trans. Antennas Propagat.*, vol.39, no.1, pp.97-104, Jan 1991.

[4] G. Annaert, "Evaluation of Sommerfeld Integrals using Chebyshev Decomposition," *IEEE Trans. Antennas Propagat.*, vol.41, no. 2, pp.159-164, Feb. 1993.

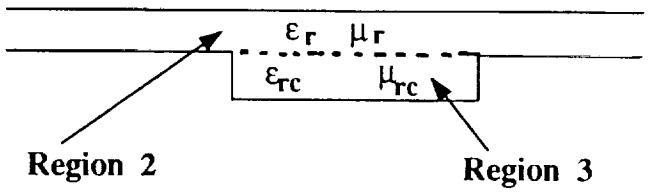

Figure 1: Geometry of a groove in a coated plane

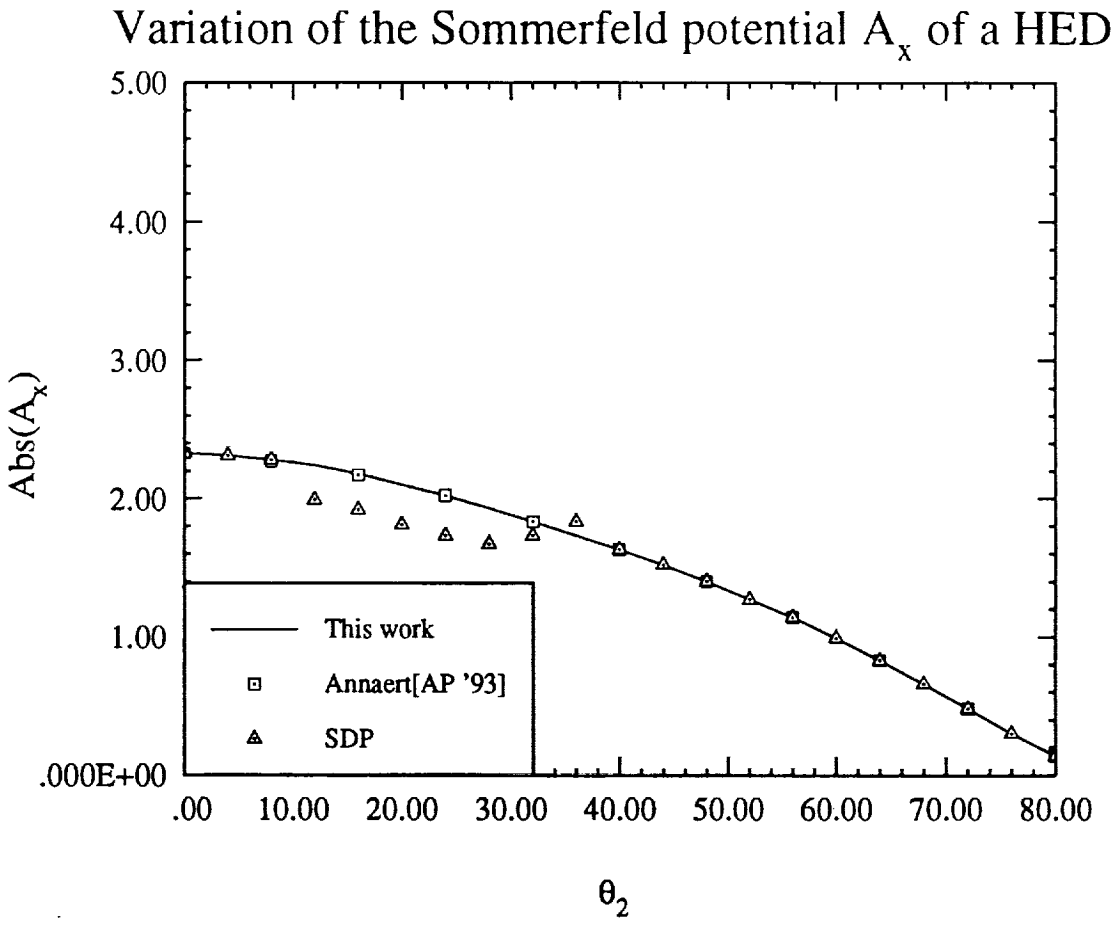

Figure 2: A typical Sommerfeld integral evaluation